UNIVERSIDADE FEDERAL DE MINAS GERAIS

Escola de Engenharia

Programa de Pós-Graduação em Engenharia Elétrica

Rodrigo Cassio de Barros

OPTIMIZATION OF BATTERY BANK SIZING FOR ENERGY STORAGE SYSTEM AND IMPACTS DURING ACTIVE FILTER OPERATION MODE

Belo Horizonte

2022

Rodrigo Cassio de Barros

Optimization of Battery Bank Sizing for Energy Storage System and Impacts During Active Filter Operation Mode

Tese de doutorado submetida à banca examinadora designada pelo Colegiado do Programa de Pós-Graduação em Engenharia Elétrica da Universidade Federal de Minas Gerais, como parte dos requisitos necessários à obtenção do grau de Doutor em Engenharia Elétrica.

Orientador: Prof. Dr. Wallace do Couto Boaventura
Coorientador: Prof. Dr. Heverton Augusto Pereira
Coorientador: Prof. Dr. Allan Fagner Cupertino

Belo Horizonte, MG

2022

Barros, Rodrigo Cassio de.
B277o Optimization of battery bank sizing for energy storage system and impacts during active filter operation mode [recurso eletrônico] / Rodrigo Cassio de Barros. - 2022.
1 recurso online (111 f. : il., color.) : pdf.

Orientador: Wallace do Couto Boaventura.
Coorientadores: Heverton Augusto Pereira, Allan Fagner Cupertino.

Tese (doutorado) - Universidade Federal de Minas Gerais, Escola de Engenharia.

Bibliografia: f.105-111.

Exigências do sistema: Adobe Acrobat Reader.

1. Engenharia elétrica - Teses. 2. Energia - Armazenamento - Teses. 3. Baterias elétricas - Teses. 4. Harmônicos (Ondas elétricas) - Teses. I. Boaventura, Wallace do Couto. II. Pereira, Heverton Augusto. III. Cupertino, Allan Fagner. IV. Universidade Federal de Minas Gerais. Escola de Engenharia. V. Título.

CDU: 621.3(043)

Ficha catalográfica elaborada pela Bibliotecária Roseli Alves de Oliveira CRB/6 2121
Biblioteca Prof. Mário Werneck, Escola de Engenharia da UFMG

UNIVERSIDADE FEDERAL DE MINAS GERAIS
ESCOLA DE ENGENHARIA
PROGRAMA DE PÓS-GRADUAÇÃO EM ENGENHARIA ELÉTRICA

FOLHA DE APROVAÇÃO

"OPTIMIZATION OF BATTERY BANK SIZING FOR STORAGE SYSTEM AND IMPACTS DURING ACTIVE FILTERS OPERATION MODE"

RODRIGO CASSIO DE BARROS

Tese de Doutorado submetida à Banca Examinadora designada pelo Colegiado do Programa de Pós-Graduação em Engenharia Elétrica da Escola de Engenharia da Universidade Federal de Minas Gerais, como requisito para obtenção do grau de Doutor em Engenharia Elétrica. Aprovada em 04 de novembro de 2022. Por:

Prof. Dr. Wallace do Couto Boaventura - DEE (UFMG) - Orientador

Prof. Dr. Heverton Augusto Pereira - DEL (UFV) - Coorientador

Prof. Dr. Allan Fagner Cupertino - DEE (CEFET-MG) - Coorientador

Prof. Dr. Pedro André Carvalho Rosas - DEE (UFPE)

Prof. Dr. Helio Marcos Andre Antunes - DEE (UFES)

Prof. Dr. Victor Flores Mendes - DEE (UFMG)

Prof. Dr. Gabriel Azevedo Fogli - DELT (UFMG)

Documento assinado eletronicamente por **Victor Flores Mendes**, **Professor do Magistério Superior**, em 04/11/2022, às 13:56, conforme horário oficial de Brasília, com fundamento no art. 5º do Decreto nº 10.543, de 13 de novembro de 2020.

Documento assinado eletronicamente por **Wallace do Couto Boaventura**, **Professor do Magistério Superior**, em 04/11/2022, às 14:07, conforme horário oficial de Brasília, com fundamento no art. 5º do Decreto nº 10.543, de 13 de novembro de 2020.

Documento assinado eletronicamente por **Gabriel Azevedo Fogli**, **Professor do Magistério Superior**, em 04/11/2022, às 15:05, conforme horário oficial de Brasília, com fundamento no art. 5º do

À minha mãe,
À minha família,
Aos meus mentores e amigos.

Agradecimentos

Primeiramente, obrigado a Deus e aos meus pais, José Maria e Gurdiana, pelo suporte incondicional. Obrigado por ensinarem que humildade e dedicação são as maiores armas que posso ter. Ao meu orientador, Prof. Wallace, pela paciência e boa vontade de ensinar. Ao meu coorientador Heverton, pelo suporte e conhecimento compartilhado. Ao grupo de pesquisa GESEP por todo o suporte durante essa caminhada. Aos meus amigos de trabalho pelo companheirismo, amizade e cumplicidade. Agradeço em especial a Dayane, pelo suporte neste trabalho. Também agradeço em especial o Prof. Allan e ao André, pelo grande suporte dado nos experimentos práticos. A todos os amigos e familiares que de forma indireta ajudaram nesta caminhada.

Resumo

Devido ao comportamento intermitente durante a geração de energia por fontes renováveis (como Fotovoltaica (FV) e eólica), o sistema de armazenamento por bateria (do inglês, *Battery Energy Storage System* - BESS) tem se apresentado como uma aplicação interessante no sistema elétrico de potência. O BESS pode ser usado para várias operações, como suporte no horário de pico, regulação de frequência e suavização de potência. Além disso, o BESS pode fornecer serviços auxiliares, como Compensação de Corrente Harmônica (do inglês, *Harmonic Current Compensation* - HCC) e suporte de energia reativa. A escolha da bateria utilizada no BESS não é uma tarefa simples, pois existem vários critérios que devem ser levados em consideração. Assim, este trabalho propõe uma metodologia de apoio ao processo de seleção de baterias. Seis critérios são considerados: a tensão do barramento cc do sistema, a vida útil da bateria, o volume do banco de baterias, as perdas de energia do banco de baterias, o preço do banco de baterias e o índice de capacidade de armazenamento. A tomada de decisão baseada em multiplos critérios (do ingês, *Multiple Criteria Decision Making* - MCDM) é usado para escolher a melhor bateria com base na importância relativa entre os conceitos de Despesa Operacional (do inglês, *operational expenditure*- OPEX) e Despesa de Capital (do inglês, *capital expenditure* - CAPEX). A metodologia proposta neste trabalho é aplicada a 27 baterias de chumbo-ácido e de íon-lítio, com o objetivo de selecionar a melhor solução para um sistema fotovoltaico, baseado no modo de operação de deslocamento de pico de geração, com foco no armazenamento de energia fora do horário de ponta e injeção no horário de ponta. Além disso, foi iniciado o estudo do BESS operando como deslocamento do pico de geração e HCC. Assim, a avaliação da vida útil do estágio dc/ac do sistema BESS é analisada com base no perfil de operação do sistema. Nesse contexto, é realizada a avaliação do tempo de vida útil dos dispositivos semicondutores e dos capacitores do barramento cc. A vida útil do estágio dc/ac do BESS trabalhando apenas com deslocamento de pico de geração é considerada como sendo o caso base e é comparada ao consumo de vida util do BESS quando este compensa correntes harmônicas 5^o e 7^o ordens. Como resultados, observa-se um aumento no consumo de vida nos componentes analisados devido ao processo de HCC. Além disso, resultados experimentais do sistema proposto (BESS com operação HCC) são apresentados neste trabalho. A bancada com os principais componentes são descritos e os resultados de condicionamento, controle e térmicos são apresentados.

Palavras-chaves: Sistema de Armazenamento de Energia por Bateria, Seleção de baterias, MCDM, Compensação Harmônica, Vida Útil do BESS.

Abstract

Due to the intermittent behavior during the energy generation by renewable energy (such as Photovoltaic (PV) and wind power generation), the Battery Energy Storage System (BESS) has been presented as an interesting application in the electrical power system. The BESS can be used for several operation, such as peak shaving, frequency regulation and power smoothing. In addition, the BESS can provide ancillary services, such as Harmonic Current Compensation (HCC) and reactive power injection. The choice of the battery employed in the BESS is not a straightforward task, since there are several criteria which should be taken into account. Thus, this work proposes a methodology to support the battery selection process. Six criteria are considered: system dc-link voltage, battery lifetime, battery bank volume, battery bank power losses, battery bank price and storage capacity index. The Multiple Criteria Decision Making (MCDM) is used to choose the best battery based on the relative importance between the Operational Expenditure (OPEX) and Capital Expenditure (CAPEX) concepts. The methodology proposed in this work is applied to 27 batteries composed by lead-acid and Li-ion (Lithium - ion) batteries aiming to select the best solution for a photovoltaic system based on the peak shaving operation mode. In this work, the BESS working with peak shaving and HCC operation are explored. Thus, the lifetime evaluation of the dc/ac stage of the BESS is analyzed based on a mission profile operation. In this context, the lifetime evaluation of the semiconductor devices and the dc-link capacitors are performed. The BESS dc/ac stage lifetime working only with peak shaving operation is considered the base case and it is compared to the lifetime consumption when the BESS compensates 5^{th} and 7^{th} harmonic current components. As results, it is observed an increasing in the lifetime consumption in the analyzed components due to HCC process. In addition, experiment results of the proposed system (BESS with HCC operation) is presented in this work. The bench test with the main components are described and results of conditioning, control and thermal are presented.

Keywords: Battery Energy Storage System, Battery Selection, MCDM, Harmonic Current Compensation, BESS Lifetime Evaluation.

List of Figures

Figure 1 – Applications of ESS, *adapted from* (Xu et al., 2016). 25
Figure 2 – Energy storage systems technologies. Adapted from (Díaz-González; Sumper; Gomis-Bellmunt, 2016). 25
Figure 3 – Benchmarking of energy storage technologies: (a) The Ragone chart; (c) Capital costs. Adapted from (Rufer, 2017). 26
Figure 4 – A typical PV system with BESS connected into the grid: (a) isolated inverted and (b) hybrid inverter. 28
Figure 5 – Comparative board between lead-acid and Lithium-ion (Li-ion) battery technologies. 34
Figure 6 – Grid connected inverter with common dc-link and two dc/dc stages. . . 35
Figure 7 – Grid connected inverter with common dc-link and two dc/dc stages with supercapacitor. 36
Figure 8 – Grid-connected inverter with three-port bidirectional full bridge converter. 36
Figure 9 – Variation of a dual inverter topology. 37
Figure 10 – Control block diagram of the Battery Energy Storage System (BESS) dc/ac stage. 38
Figure 11 – Flowchart for the lifetime evaluation of Lead battery proposed by Schiffer et al. (2007). 41
Figure 12 – Flowchart for Li-ion battery lifetime proposed by (Stroel Ioan, 2014). . 44
Figure 13 – Thermal cycles representation: (a) long cycle thermal and (b) short cycles. 46
Figure 14 – Flowchart for the lifetime evaluation of the semiconductor devices. . . . 46
Figure 15 – Power losses look-up table generation process. 46
Figure 16 – Inverter injecting fundamental current to the grid: (a) average power losses and (b) junction temperature. 47
Figure 17 – Flowchart for the lifetime evaluation for the dc-link capacitor. 49
Figure 18 – Voltage representation of the BESS dc/ac stage dc-link voltage and voltage limits of the battery bank. 52
Figure 19 – TOPSIS method used to select the best battery based on the selected criteria. 56
Figure 20 – Criteria separation into OPEX and CAPEX group. 59
Figure 21 – Optimum matrix of the battery solution. 59
Figure 22 – Proposed methodology assisted by choice matrix approach. 60
Figure 23 – Load mission profile over one year with sample time equal to 5 min. . . 61

Figure 24 – One year mission profile of the battery bank power (a) solar irradiance, (b) ambient temperature and (c) battery bank power mission profile. . 62
Figure 25 – Representation of the BESS peak shaving operation over one week. . . 62
Figure 26 – Battery design estimations: (a) number of batteries in series and in parallel and (b) total number of batteries. 64
Figure 27 – Optimum matrix solution for the lead-acid battery models (form M1 to M13). 64
Figure 28 – Optimum matrix solution for the Li-ion battery models (form 14 to 27). 66
Figure 29 – Optimum matrix solution for lead-acid and Li-ion batteries(form 1 to 27). 66
Figure 30 – Structure of a BESS used to perform the common applications and also ancillary services. 68
Figure 31 – BESS injecting 200 kW of active power: Output current (phase a) comparison of traditional operation with HCC. In this case, the BESS dc/ac stage is compensating 5^{th} (a) and 7^{th} (b) harmonic current components with phases angle of 0^o and 180^o, respectively. 71
Figure 32 – BESS injecting 200 kW of active power: Power losses (a) and junction temperature of the IGBT (Phase a). In this case, the BESS dc/ac stage is compensating 5^{th} with phases angle equal to 0^o in (a) and 7^{th} harmonic current components with phase angle equal to 180^o in (b). . . 72
Figure 33 – Flowchart of the long cycle lifetime evaluation considering the HCC operation mode. 72
Figure 34 – Power losses look-up table generation process. 73
Figure 35 – Variation of the semiconductor power losses due the harmonic phase angle variation: (a) IGBT and (b) diode. 74
Figure 36 – Variation of the semiconductor power losses due the harmonic amplitude variation: (a) IGBT and (b) diode. 74
Figure 37 – Power losses of the semiconductor devices when the active power was equal to 500 kW and the ambient temperature equal to 25 ^{o}C. For the IGBT, the 5^{th} and 7^{th} harmonic components were compensated considering: (a) $I_5 = 0.6\ I_f$ and $I_7 = 0.3\ I_f$, (b) $I_5 = 0.3\ I_f$ and $I_7 = 0.6\ I_f$ and (c) $I_5 = 0.6\ I_f$and I_7= $0.6\ I_f$. For the diodes, the same study were provided: (d) $I_5 = 0.6\ I_f$ and $I_7 = 0.3\ I_f$, (e) $I_5 = 0.3\ I_f$ and $I_7 = 0.6\ I_f$ and (f) $I_5 = 0.6\ I_f$ and $I_7 = 0.6\ I_f$. 75
Figure 38 – Flowchat of the proposed short-cycles methodology: the LC look-up table generation. 76
Figure 39 – Exemplification of the total number of short cycles based on the mission profile resolution. 78
Figure 40 – Flowchart of the LC calculation for the short cycles thermal load. . . . 78

Figure 41 – The effect on the semiconductor LC due to harmonic phase angle variation. The active power is considered 500 kW, the ambient temperature 25^{o}C and the harmonic current amplitude is equal to 0.6 I_f. 79
Figure 42 – LC of the semiconductor devices when the active power was equal to 500 kW and the ambient temperature equal to 25 ^{o}C. For the IGBT, the 5^{th} and 7^{th} harmonic components were compensated considering: (a) $I_5 = 0.6\ I_f$ and $I_7 = 0.3\ I_f$, (b) $I_5 = 0.3\ I_f$ and $I_7 = 0.6\ I_f$ and (c) $I_5 = 0.6\ I_f$and I_7= 0.6 I_f . For the diodes, the same study were provided: (d) $I_5 = 0.6\ I_f$ and $I_7 = 0.3\ I_f$, (e) $I_5 = 0.3\ I_f$ and $I_7 = 0.6\ I_f$ and (f) $I_5 = 0.6\ I_f$ and $I_7 = 0.6\ I_f$. 80
Figure 43 – Mission profiles of: (a) solar irradiance, (b) ambient temperature, (c) power consumed by the load and (d) battery bank power. 81
Figure 44 – Mission profile of: (a) 5^{th} harmonic amplitude, (b) 7^{th} harmonic amplitude, (c) 5^{th} harmonic phase angle and (d) 7^{th} harmonic phase angle. 82
Figure 45 – Mission profile histogram of: (a) 5^{th} harmonic amplitude, (b) 7^{th} harmonic amplitude, (c) 5^{th} harmonic phase angle and (d) 7^{th} harmonic phase angle. 82
Figure 46 – Mean junction temperature for one year operation considering the long cycles analyzes for (a) IGBT and (b) diode. 83
Figure 47 – Hot-spot temperature of one year operation for the dc-link capacitor. . 84
Figure 48 – Unreliability function considering the system level composed only of: (a) IGBT, (b) diode and (c) dc-link capacitor. 85
Figure 49 – Unreliability function considering the system level composed of all the components (IGBT, diode and dc-link capacitor) 86
Figure 50 – Schematic of the laboratory test bench used in this work. 87
Figure 51 – Three-dimensional model of the power model used in the test bench (SEMIKRON, 2006). 88
Figure 52 – Images of the laboratory test bench used in this work. 89
Figure 53 – Control block diagram for INV1 and INV2. 89
Figure 54 – SOGI-PLL performance: synchronization of the line voltage and $w(t)$ waveforms. 90
Figure 55 – Output current of a three-phase PV inverter injecting: (a) 6 A of I_f and: (b) 2 A of I_5 with $\theta_h = 180^o$, (c) 2 A of I_7 with $\theta_h = 180^o$ and (d) 2 A of I_5 and I_7 with $\theta_h = 180^o$. 91
Figure 56 – Spectrum current of a three-phase PV inverter injecting: (a) 6 A of I_f and: (b) 2 A of I_5 with $\theta_h = 180^o$, (c) 2 A of I_7 with $\theta_h = 180^o$ and (d) 2 A of I_5 and I_7 with $\theta_h = 180^o$. 91

Figure 57 – Waveforms of the inverter and battery bank currents with I_f equal to 3.5 A: (a) without harmonic current compensation and (b) With harmonic current compensation (I_5 equal to 1 A). 92
Figure 58 – Charging and discharging performance of the battery bank (a) fundamental current reference of the inverter and (b) battery bank voltage. 93
Figure 59 – Capacitor bank of INV1 with the specification of C_1 to C_6. 94
Figure 60 – Thermal images of current capacitor bank for: (a) Case 1, (b) Case 2, (c) Case 3 and (d) Case 4. 95
Figure 61 – Representation of a NI9213 manufactured by National Instruments. . . 96
Figure 62 – Measurements of the batteries and ambient Temperatures in (a) and temperature variation of the batteries comparing to the ambient temperature (b). 96
Figure 63 – Temperature variation of the batteries compared to the ambient temperature. 97
Figure 64 – Inverter and battery bank current considering: (a) Case 1, (b) Case 2 and (c) Case 3. 97
Figure 65 – Spectrum of the battery bank current considering: (a) Case 1, (b) Case 2 and (c) Case 3. 98

List of Tables

Table 1 – Scale of relative importance of the selected criteria. 58
Table 2 – The pair-wise comparison matrix. 58
Table 3 – Batteries and its main parameters. 63
Table 4 – Battery Models and the main parameters. 65
Table 5 – Main parameter of the BESS 69
Table 6 – IGBT thermal resistences. 73
Table 7 – LC for the IGBT and diode considering the short and long cycles. LC for Case 1 considering: short IGBT = 0.0032; LC long IGBT = 0.012; LC short diode = 0.0010 and LC long diode = 0.010. 84
Table 8 – LC for the dc-link capacitor considering one year mission profile. The LC base case is 0.0182. 85
Table 9 – Main parameter and specification of the power module. 88
Table 10 – Electrical specification of the battery used in this work. 89
Table 11 – Temperatures (in degree) values of the dc-link capacitors. 94

List of abbreviations and acronyms

AGM Absorbed Glass Mat

ANEEL Brazilian Regulatory Agency

AHP Analytic Hierarchy Method

BESS Battery Energy Storage System

CAPEX Capital Expenditure

CDF Cumulative Density Function

DSP Digital Signal Processing

DOD Depth of Discharge

ESS Energy Storage System

GESEP *Gerência de Especialista em Sistemas Elétricos de Potência*

GW Gigawatts

HCC Harmonic Current Compensation

HF High Frequency

LF Low Frequency

Li-ion Lithium-ion

IGBT Insulated Gate Bipolar Transistor

MCDM Multiple Criteria Decision Making

MPPT Maximum Power Point Tracker

OPEX Operational Expenditure

PCC Point of Common Coupling

PDF Probability Density Function

PLL Synchronous Phase Locked Loop

PoF Physics of Failure

PMR Proportional Multi-resonant Controller

PV Photovoltaic

PHS Pumped Hydro Storage

RE Renewable Energy

RMS Root Mean Square

SOC Stage of Charge

SOGI Second Order Generalized Integrator

TOPSIS Technique for Ordering Preferences Similar to an Ideal Solution

List of symbols

a_i	criteria used in the AHP method.
A^+	ideal solution
A^-	anti-ideal solution
c_b	cost of the battery bank
c_{bat}	cost of a single battery
c_t	battery temperature coefficient
c_u	battery voltage coefficient
C_{cal}	capacity fade due to calendar
$C_{cal,actual}$	actual month calendar capacity fade
$C_{cal,previous}$	previous month calendar capacity fade
$C_{cal,tot}$	total capacity fade due to the cycling calendar process
C_{corr}	battery corrosion mechanism
$C_{corr,lim}$	battery limit of corrosion process
C_{cycle}	capacity fade due to cycling
$C_{cycle,tot}$	total capacity fade due to the cycling aging process
C_d	dc-link capacitance
C_{deg}	battery degradation mechanism
$C_{deg,lim}$	battery limit of the degradation process
C_f	capacitance of the LCL filter capacitor
$C_{fade,tot}$	total battery capacity fade
C_i	ranking score of the batteries
C_n	Nominal battery capacity
C_r	battery C-rate

$d_{i,j}$	attribute given to each criteria in the TOPSIS method
$d_N i, j$	normalized attribute given to each criteria
D	attribute matrix
D_N	normalized decision matrix
D'_N	normalized weighted matrix construction
E_n	energy requirement
E_{bat}	energy of a singe battery
$En_{Generated}$	energy produced by the system over one year
En_{Stored}	energy stored by the battery bank over one year
ESR	capacitor equivalent series resistance
f_{acid}	weighted factor of the acid stratification effect
f_n	grid frequency
f_{SOC}	weighted factor of the SOC effect
f_x	Weibull probability density function
Fb_1	full bridge converter number 1
Fb_2	full bridge converter number 2
Fb_3	full bridge converter number 3
F_x	cumulative density function
g	electrolyte proportionality constant
G	irradiance
h	harmonic order
i_G	grid Voltage
i_h	harmonic current
$i_h{}^*$	harmonic current reference
i_s	BESS output current
i_s^*	reference of the BESS output current

$i_{sa}(t)$	BESS output current for phase a
I_{bat}	BESS current
I_{Bat}	fundamental BESS current
I^*_{Bat}	fundamental BESS current reference
$I_{gas,0}$	normalized gassing current
I_h	harmonic current component amplitude
$I_{i(RMS)}$	rout mean square of the capacitor current
In_{Cap}	battery bank stored capacity index
$INV1$	Inverter 1 of the bench
$INV2$	Inverter 2 of the bench
k	number of samples of the mission profile
k_b	Boltzmann constant
k_s	battery corrosion speed
L	time to failure of the capacitor
LC	lifetime consumption of the semiconductor device
L_f	inductor from the converter side
L_F	battery lifetime
L_g	inductor from the grid side
L_0	time to failure of the capacitor under testing
L_1	inductor of the inverter 1 in the bench
L_2	inductor of the inverter 2 in the bench
M_c, M_d	charge-transfer overvoltage
M_i	battery numbered from i = 1 to i = 27
n	number of battery criteria
n_c	number of dc-link capacitors
n_i	number of IGBTs

N	number of time which a specific battery energy is stored in a year
N_{En}	number of batteries based on the energy requirement
N_f	number of cycle of the semiconductor device
N_{min}	minimum number of batteries
N_{Pn}	number of batteries based on the power requirement
P_{avg}	average power losses of BESS semiconductor devices
$P_{c,loss}$	power losses of BESS dc/ac capacitors
P_{loss}	power losses of BESS dc/ac semiconductor devices
P_n	power required
P_{Bat}	battery power losses
P_{IGBT}	IGBT power losses
PL_b	power losses dissipated in the battery bank
r_{bat}	internal resistance of a single battery
R	capacitor thermal resistence
$R_{th(c-a)}$	case to ambient thermal resistence
$R_{th(j-c)}$	junction to case - Diode thermal resistence
$R_{th(j-c)}$	junction to case - IGBT thermal resistence
SOC_{max}	maximum SOC value
SOC_{mim}	minimum SOC value
SS	steady-state
S^+	euclidean distance from the ideal solution
S^-	euclidean distance from the anti ideal solution
t	time which the battery stay in idling mode
t_{on}	semiconductor device heating time
t_{sim}	time to achieve the steady-stage of the BESS simulation
T_{amb}	ambient temperature

$T_{gas,0}$	battery nominal battery temperature
T_{jm}	mean junction temperature
T_h	hot-spot temperature of the capacitor
T_s	sampling time of the mission profile
T_{Bat}	battery temperature
T_{IGBT}	junction temperature of the IGBT
$U_{gas,0}$	capacity at nominal voltage
v_{PCC}	voltage at point of common coupling
v_1	dc-link voltage of converter 1
v_2	dc-link voltage of converter 2
v_3	dc-link voltage of converter 3
V_{bmax}	battery bank maximum voltage
V_{bmin}	battery bank minimum voltage
V_{batmax}	battery maximum voltage
V_{batmin}	battery minimum voltage
V_{Bat}	voltage of a single battery cell
V_c	operation voltage of the capacitor
V_{dc}	dc-link voltage
$V_{dc}{}^*$	dc-link voltage reference
V_{dcmin}	minimum voltage of the dc-link
Vl_b	battery bank volume
Vl_{bat}	single battery volume
$\hat{V}_g$	peak of the line-to-line neutral voltage
U_0	open-circuit equilibrium cell voltage
x_{pu}	unit equivalent output impedance of the inverter
z_w	weight battery number of cycle

Δt	duration of one time step of the battery mission profile
ΔT_j	fluctuation junction temperature
ΔV_g	maximum ac grid voltage variation
$\Delta W(t)$	corrosion layer thickness
δ	margin of the dc/dc battery bank stage
θ_h	harmonic current phase angle
$\rho_{corr,lim}$	battery limit of internal resistance
ρ_c, ρ_d	aggregated internal resistances
ω_f	angular grid frequency

Contents

1 INTRODUCTION 24
1.1 Energy Storage System Technologies 24
1.2 Battery Selection 27
1.3 Energy Stored System Reliability 29
1.4 Purpose and Contributions 29
1.5 Organization of this PhD Thesis 30
1.6 List of Publications 30
1.6.1 Published Journal Paper 30
1.6.2 Submitted Journal Paper - Under Review 31
1.6.3 Published Conference Paper 31
1.7 Acknowledgement 31

2 LITERATURE REVIEW 32
2.1 Battery Technology Overview 32
2.1.1 Lead-acid Battery 32
2.1.2 Li-ion Battery 33
2.2 Power Processing Structures for PV Inverters with BESS 34
2.2.1 Common dc-link and Two dc-dc Stages 34
2.2.2 Three-port Bidirectional Full Bridge Converter 36
2.2.3 Common ac Connection: Dual Inverter Topology 37
2.3 Multiple Criteria Decision Making 38
2.4 Lifetime Evaluation Methods 39
2.4.1 Lead-acid Battery Lifetime 40
2.4.2 Li-ion Battery Lifetime 43
2.4.3 Semiconductor Devices Lifetime 45
2.4.4 dc-link Capacitor Lifetime 48
2.4.5 Monte-Carlo Simulation 50
2.5 Chapter Conclusions 50

3 METHODOLOGY FOR BESS DESIGN ASSISTED BY CHOICE MATRIX APPROACH 51
3.1 Storage System Design 51
3.1.1 Step 1: Minimum Number of Battery 51
3.1.2 Step 2: Voltage Limits of the Battery Bank 52
3.1.3 Step 3: Battery Bank Design 53
3.2 Battery Selection Criteria 53

3.2.1 dc-link Voltage of the BESS dc/ac Stage . . . 54
3.2.2 Battery Bank Volume . . . 54
3.2.3 Total Battery Bank Power Losses . . . 54
3.2.4 Stored Capacity Index . . . 54
3.2.5 Total Battery Bank Cost . . . 55
3.2.6 Battery Lifetime . . . 55
3.3 Multiple Criteria Decision Making . . . 55
3.4 Application of the Proposed Methodology . . . 60
3.5 Chapter Conclusions . . . 66

4 LIFETIME EVALUATION OF THE BESS DC-AC STAGE DURING HCC OPERATION . . . 68
4.1 BESS Parameters . . . 68
4.2 Case Study 1: Constant Harmonic Current Compensation . . . 70
4.2.1 Lifetime Estimation Considering Long cycle Thermal Loading . . . 71
4.2.2 Lifetime Estimation Considering Short cycle Thermal Loading . . . 76
4.3 Case Study 2: HCC Based on Mission Profile Operation . . . 79
4.3.1 Lifetime Evaluation of Semiconductor Devices . . . 83
4.3.2 Lifetime Evaluation of Dc-link Capacitor . . . 84
4.3.3 Monte Carlo Simulation Analyzes . . . 85
4.4 Chapter Conclusions . . . 86

5 EXPERIMENTAL RESULTS . . . 87
5.1 Electrical Schematic of the Test Bench . . . 87
5.2 Validation of the Control Adopted Strategy . . . 90
5.3 HCC Effect on the dc-link capacitors . . . 93
5.4 HCC Effect on the Battery Bank . . . 95
5.5 Chapter Conclusions . . . 98

6 CLOSURE . . . 99
6.1 Conclusions . . . 99
6.1.1 Battery Choice Based on OPEX and CAPEX Analysis . . . 99
6.1.2 Lifetime Evaluation of Semiconductor Devices During HCC Operation Mode . . . 100
6.1.3 Experimental Results in the Test Bench . . . 100
6.2 Next steps - Propose . . . 100

REFERENCES . . . 102

1 Introduction

1.1 Energy Storage System Technologies

According to (REN, 2022), Renewable Energy (RE) represented 84 % of newly installed power capacity in the world. In this context, the added power installed was greater than 314 Gigawatts (GW) in 2021, achieving another record breaking year (REN, 2022). In this context, solar Photovoltaic (PV) maintained its record-breaking streak, adding 175 GW of new capacity in 2021 to reach a cumulative total of around 942 GW.

With the increasing of the RE installation, concerns related to the intermittent nature of the power generation have been discussed (Ahmed et al., 2020; Nguyen; Shim, 2020). Power oscillations due to intermittency may also cause rapid voltage fluctuations, which are avoided in the power system (Kamali et al., 2013). Grid stresses related to the recurrent voltage and frequency oscillations caused by the irregular PV or winds plants power generation could be indeed a limiting factor on the future expansion of RE applications.

In this context, Energy Storage System (ESS) have become a possible solution to support the potential increasing of RE installation. ESS can contribute to improving system reliability and maintaining sensible operational costs in the aforementioned case. These ESS installations provide various electric grid services including frequency regulation, voltage support, renewable energy time-shift, renewable energy smoothing and leveling, demand reduction, and support for power reliability, power quality, and islanding operations. In addition, for transmission and distribution systems, the ESS has also been applied for reliability improvement as an alternative to more costly line upgrade projects Xu et al. (2016). The benefits and usage of ESS can be classified in five categories, as presented in Fig. 1.

There are some ESS technologies, such as electrochemical, eletromagnetic, eletromechanical and thermal storage. A representation of the ESS technologies are presented in Fig. 2. The electrochemical technology is considered an indirect storage process, since the energy needs to be converter to a chemical energy to be stored. The batteries are an example of the electrochemical energy storage. On the other hand, the eletromagnetic components store the energy directly as an electrical or magnetic filed. The supercapacitor is an example of this storage technology (Xu et al., 2016).

The eletromechanical storage technology is related to the conversion of the mechanical to electrical energy, such as pumped hydro, flywheel and compressed air. Pumped Hydro Storage (PHS) is a mature and widely implemented form of energy storage

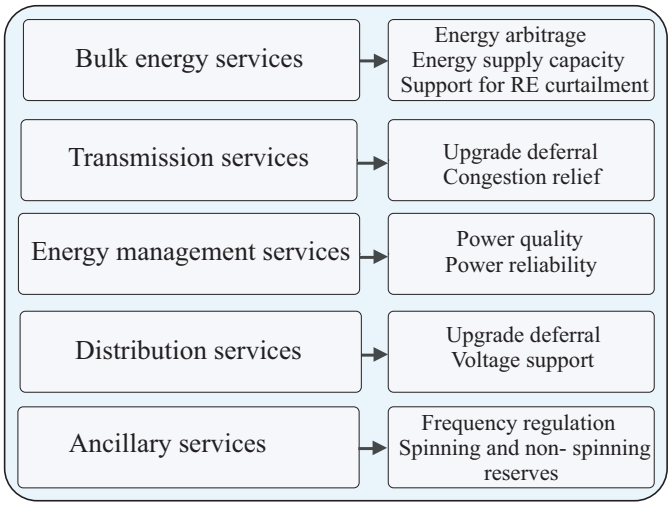

Figure 1 – Applications of ESS, *adapted from* (Xu et al., 2016).

Source: Own authorship.

for power/grid applications. Many water reservoirs have come to be utilized for PHS projects with the aim of saving energy in times of energy availability by pumping water to higher altitudes and then generating energy from it in the reverse process (Rufer, 2017). In addition, as the name suggests, the compressed air energy storage is the ESS which stores energy in the form of compressed air in natural underground caverns or constructed air chambers (WeiQing; Seamus, 2019). Finally, flywheels are rotating masses, which store energy in the form of kinetic energy. The rotational energy is stored in an accelerated rotor, which is constructed as a massive rotating cylinder (PereiraL; Martínez, 2022).

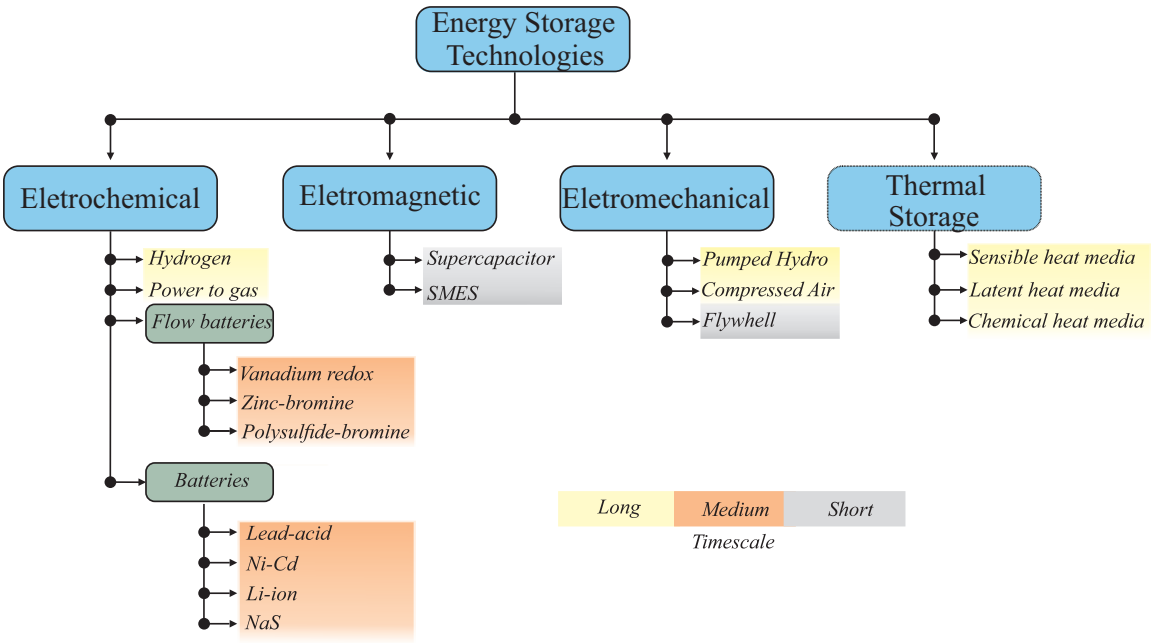

Figure 2 – Energy storage systems technologies. Adapted from (Díaz-González; Sumper; Gomis-Bellmunt, 2016).

The choice of the energy storage technology depends on some criteria, such

as the power and energy rating, response time, operating cycles, weight, volume and temperature (Díaz-González; Sumper; Gomis-Bellmunt, 2016). In this context, Fig. 3(a) exhibits Ragone Diagram of energy storage technologies. In this graph, power density (W/kg) is compared with energy density (Wh/kg). The higher the energy density, the greater the amount of energy available per unit of mass or volume. Besides that, the lower the power density, the lower the speed of energy transfer per unit of mass or volume. Fig. 3(b) presents the costs related to different energy storage technologies. It is important to remark that the selection of a particular technology must be assessed against technical performance and application requirements.

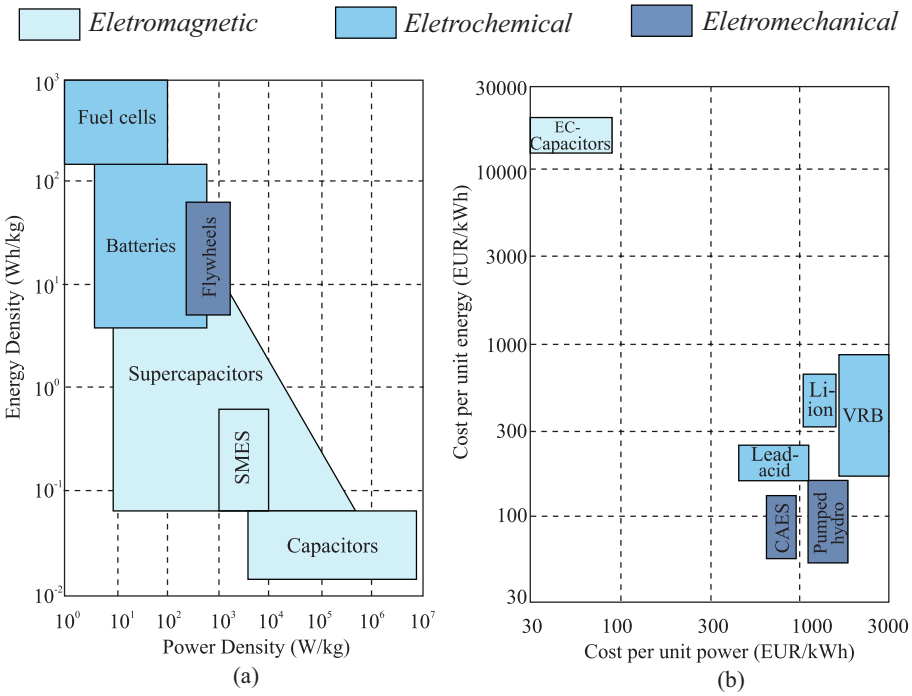

Figure 3 – Benchmarking of energy storage technologies: (a) The Ragone chart; (c) Capital costs. Adapted from (Rufer, 2017).

The focus of the thesis is on the ESS which uses batteries as an energy storage source is called Battery Energy Storage System (BESS). This ESS is categorized as electrochemical devices which delivers electric energy by conversion of chemical reactions. The use of BESS technology can be deployed on the power grid at a substation, distributed along a feeder or as a residential community. Furthermore, the use of BESS in those applications can be explained based on the flexibility in location for installation, shorter construction time of the facilities and quick response time to system events. With regarding to the RE application, the BESS can be used for the following applications (Jiang et al., 2018):

- Grid frequency regulation;
- Economic dispatch (arbitrage);

- Shifting the time of peak generation (peak shaving);
- Renewable energy output smoothing;
- Renewable energy output leveling.

In addition, auxiliary services based on BESS can be performed, such as, reactive power support and Harmonic Current Compensation (HCC). Wang et al. (2017), Jiang et al. (2018), Zimann et al. (2019) propose the use of BESS with the reactive power support to the grid to perform voltage regulation. In reference Abba et al. (2020) the feasibility of BESS acting as coordinated active harmonic filters is performed. In the same context, harmonic mitigation based on the battery system is provided in (Xu et al., 2015).

The focus of this thesis is on the the peak shaving operation, which is an application that has been used in the recent decades and it operates in parallel with PV system. When the peak of the energy consumed by a load is not around noon, which roughly corresponds to the peak generation PV power production, the BESS can act as a buffer, storing energy during the peak generation period and injecting this energy during the peak loading period (Farihan et al., 2018; Xu et al., 2016). This application can reduce the cost spend to the energy from the electrical grid and it commonly used in European countries.

1.2 Battery Selection

Despite their benefits, the BESS implementation in grid connected power systems deals with considerable challenges in terms of converter design, grid integration and dc/dc stage inclusion (Manz; Piwko; Miller, 2012). Especially, the battery bank sizing is a crucial step in the project, since the battery is one of the most expensive component of BESS (Wang et al., 2016; Manz; Piwko; Miller, 2012). The battery market offers several technologies, and lead-acid and Li-ion technologies are consolidated in the rechargeable battery market with more maturity and better cost/benefit (Linden; Reddy, 2001). Currently, there are hundreds of manufacturers which have different catalogs with the most different types of batteries (Chen; Sen, 2016). Thus, the challenge of a designer for a battery bank is related to a multiple criteria decision related to the choice of the manufacturer, battery technology and electrical characteristics (Fathima; Palanisamy, 2015; Byrne et al., 2018).

One of the first steps to build the BESS is the selection of the converter topology to be applied in the integration of the battery bank with the power system (Wang et al., 2016; Xavier et al., 2019). Classical topologies of two-level converters are widely discussed in the literature due to its simplicity of operation and implementation, which employ a smaller number of passive components in the dc-link, decreasing the converter cost. The two-level converters can be employed with an integration of a dc/dc stage to integrate

the grid voltage level with the minimum BESS voltage (Vazquez et al., 2010; Wang et al., 2016; Xavier et al., 2019). In addition, for connection to the grid, passive low-pass filters are applied to reduce the harmonics produced by the converter semiconductor devices (Vazquez et al., 2010).

Fig. 4 presents a typical structure of PV system with BESS connected to the grid. As observed in Fig. 4 (a), the BESS can be connected separated of the PV inverter. This topology is generally used for high power processing. For low power processing, for example residential system, the BESS is generally composed of a hybrid inverter, as presented in Fig. 4 (b). For both structure, a BESS converter is used, which has bidirectional function to promote the battery bank charging and discharging process. The BESS connected to a PV system is also interesting when the PV inverter achieves its nominal power, since the extra energy can be used to charge the battery bank.

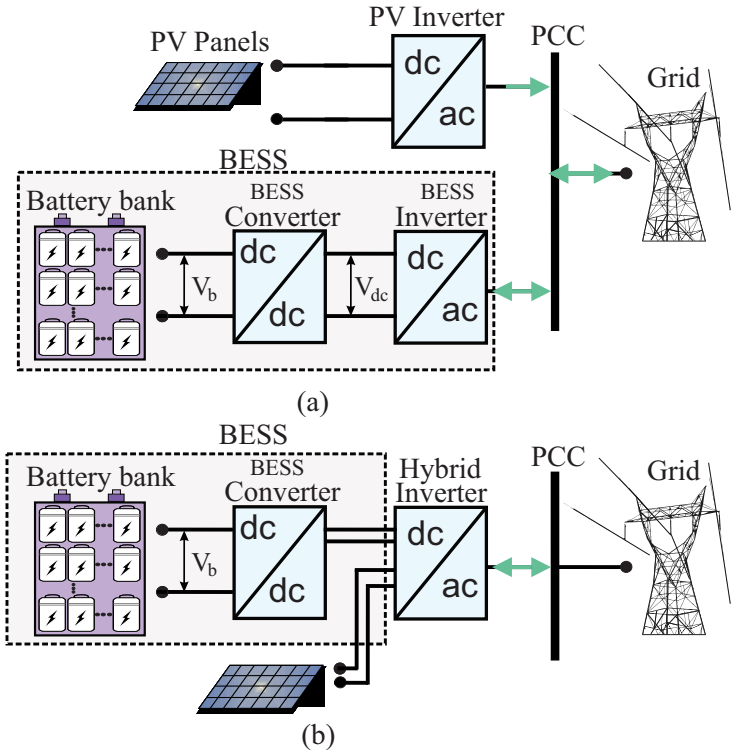

Figure 4 – A typical PV system with BESS connected into the grid: (a) isolated inverted and (b) hybrid inverter.

Source: Own authorship.

In this sense, once the BESS structure is chosen, the next step is to design the battery bank. Based on the BESS characteristics such as: output voltage, storage system autonomy, converter energy and power, the array arrangements of batteries in series and the strings in parallel can defined (Fathima; Palanisamy, 2015). On the other hand, the choice of the battery to be used in the storage system is not a straightforward task, since there are many important criteria during the battery selection, such as: battery bank

volume/weight, power losses of the storage system, battery lifetime, total battery bank price and capacity of storage (Fathima; Palanisamy, 2015; Byrne et al., 2018).

In this context, this work proposes a methodology to choose the battery to be used in the BESS. The main idea is grouping the battery bank criteria based on the Capital Expenditure (CAPEX) and Operational Expenditure (OPEX) concepts and relative importance. Thus, Multiple Criteria Decision Making (MCDM) methods are used to choose the best battery model based on the selected criteria. The MCDM methods are applied to different areas of knowledge such as industries, material selection, investment decision and economics (Fathima; Palanisamy, 2015; Panday; Bansal, 2016). In specific for this thesis, the Technique for Ordering Preferences Similar to an Ideal Solution (TOPSIS) method is used to classify and order the best battery for the BESS application (Yoon, 1980; Fathima; Palanisamy, 2015). In addition, the Analytic Hierarchy Method (AHP) method is used to estimate the weights for the battery selection criteria (Ashby; Cebon, 1993).

1.3 Energy Stored System Reliability

As discussed in the previous sections, the BESS can be used in many applications. Therefore, the reliability of the systems using have been concerning researchers in the area. Since the cost of the BESS is still expensive, it is strongly recommended to address the reliability of the system (Sandelic ; Sangwongwanich; Blaabjerg, 2019; Sandelic; Sangwongwanich; Blaabjerg, 2019). In addition, the BESS performance can affect the power electronic converters reliability. Thus, the lifetime evaluation considering all the components of the system is an interesting assignment.

Regarding the PV system with BESS application, some works have performed reliability study about this topic. In reference Sangwongwanich et al. (2018a), a single-phase dc-coupled PV battery system was considered and the impact of different self consumption control strategies on the PV inverter reliability were analyzed. Even thought the reliability of the PV inverter was addressed, it was not studied the battery lifetime.

References Sandelic , Sangwongwanich and Blaabjerg (2019), Sandelic, Sangwongwanich and Blaabjerg (2019) analyze the reliability of the remaining power converters (i.e., PV boost converter and battery converter), in which the system level reliability was investigated when considering both dc-coupled and ac-coupled BESS configurations. Reference (Jinkui; Yang; Vinnikov, 2020) contributes for the reliability analysis considering PV system in high power application. In addition, reference Jinkui, Yang and Vinnikov (2020) investigates the BESS solutions of dc and ac-coupled configurations for 1500 V PV systems with a comparative reliability analysis. Even though

there are some works related to the BESS reliability, there is a lack in the literature regarding the BESS with ancillary services, such as HCC and reactive power injection. Thus, in this qualification work, the lifetime evaluation considering dc/ac stage of the BESS with HCC operation mode is performed.

1.4 Purpose and Contributions

Based on the previous sections, the main objectives of this PhD thesis can be addressed. In this context, the main objectives and contributions of this work are:

- Propose a methodology to select the best battery for the BESS based on the OPEX and CAPEX concepts and their relative importance;
- Perform the lifetime evaluation of the BESS dc/ac stage with HCC operation. The lifetime analysis of semiconductor devices and dc-link capacitors are performed;
- Perform laboratory tests in the test bench to validate the BESS operating as peak shaving and HCC operation.

1.5 Organization of this PhD Thesis

This work is organized in six chapters. In Chapter 1, an introduction contextualizing the BESS is presented. The objectives and contributions of this work are shown. In Chapter 2 a literature review is presented and the main methods used to achieve the objectives of the work are analyzed and explained. Thus, the methods used in the battery selection process and lifetime models for each component of the system are presented. In Chapter 3, a methodology to select the battery for the system based on the CAPEX and OPEX relative importance is proposed. In addition, in Chapter 4, the BESS operating as peak shaving operation and HCC as auxiliary service is presented. In this context, the effect of the HCC operation mode in the lifetime of the semiconductor devices and dc-link capacitors of the BESS dc/ac stage are addressed. Also, results of the test bench are presented in Chapter 5. Finally, in Chapter 6, the finals considerations are stated.

1.6 List of Publications

In this section the published and submitted papers related to this work are presented.

1.6.1 Published Journal Paper

R. C. de Barros, W. C. Boaventura, A. F. Cupertino and H. A. Pereira. Lifetime Evaluation of a Three-phase Photovoltaic Inverter During Harmonic Current Compensation. Eletrônica de Potência, 2022.

R. C. de Barros, E.M.S. Brito, W. C. Boaventura, A. F. Cupertino and H. A. Pereira. Methodology for Bondwire Lifetime Evaluation of Multifunctional PV Inverter During Harmonic Current Compensation. International Journal of Electrical Power Energy Systems, v. 128, p. 106711, 2021. ISSN 0142-0615, 2021.

R. P. Silva, D. B. Silveira, R. C. de Barros , J.M. Callegari, W. C. Boaventura, A. F. Cupertino and H. A. Pereira. Third-Harmonic Current Injection for Wear-out Reduction in Single-Phase PV Inverters. IEEE Transactions on Energy Conversion, 2021.

R. P. Silva, R. C. de Barros, W. C. Boaventura, A. F. Cupertino and H. A. Pereira.Correction Strategy for Wear-out Prediction of PV Inverters Considering the Mission Profile Resolution Effects. Microelectronics Reliability, 2021.

R. P. Silva, R. C. de Barros, E.M.S. Brito, W. C. Boaventura, A. F. Cupertino and H. A. Pereira. Pursuing computationally efficient wear-out prediction of PV inverters: The role of the mission profile resolution. Microelectronics Reliability, v. 110, p. 113679, 2020.

1.6.2 Submitted Journal Paper - Under Review

R. C. de Barros, W.C.S. Amorim, W. C. Boaventura, A. F. Cupertino, V. F. Mendes and H. A. Pereira.Methodology for Optimization of Battery Model Choice Applied in BESS System. Journal of Power Sources.

1.6.3 Published Conference Paper

R. C. de Barros, R. P. Silva, D. B. da Silveira, W. C. Boaventura, A. F. Cupertino and H. A. Pereira, Third Harmonic Injection Method for Reliability Improvement of Single-Phase PV Inverters, 2019 IEEE 15th Brazilian Power Electronics Conference and 5th IEEE Southern Power Electronics Conference (COBEP/SPEC), Santos, Brazil, 2019, pp. 1-6.

1.7 Acknowledgement

This work received financial support from CEMIG-D through Brazilian Regulatory Agency (ANEEL) P&D program. The RD related project, entitled D0722 - *Análise de arranjo técnico e comercial baseado em uma planta piloto de sistema distribuído de*

armazenamento de energia em alimentador crítico da rede de distribuição de 13,8 kV, is an opportunity to deal with the interaction of battery energy storage systems and distribution feeders. The objectives are the development, construction, installation along with technical, regulatory and economic evaluation of a pilot plant for energy storage connected directly to the medium voltage grid (13.8 kV), promoting support for various ancillary services. The pilot plant for this P&D project is composed by two BESS, to be connected to the feeder servicing the UFMG, one of lithium-ion technology, 750 kVA/1000 kWh, and the other of advanced lead-carbon (PbC) , 400 kVA/ 750kWh.

2 Literature Review

In this chapter, a literature review about the main topics discussed in this work are presented. First of all, it is introduced the main characteristics of lead-acid and Li-ion batteries technologies. In addition, an overview of power processing structures of PV inverters with BESS is discussed. Some of the main topologies addressed in the literature and their relevant information are shown. Finally, the overview of lifetime evaluation methods for the main components in a BESS structure are described.

2.1 Battery Technology Overview

The BESS is composed by a group of batteries (battery bank) which can be connected in series and/or parallel to achieve the desired power and energy required by the project (Kazmierkowski, 2018). In addition, the battery is composed by a set of cell which is able to store electrical energy form of chemistry energy. This conversion process can achieve an efficiency around 80 % to 90 % (Kazmierkowski, 2018).

According to the battery internal material, the battery can be classified as reliable (secondary cells) and non-reliable (primary cells) (Moseley; Rand; Peters, 2015). The secondary cells can be recharged with the support of an electrical external source and this type of cell can be reused. For this reason, the secondary cell is used in many applications, such as renewable energy project, cell phone, electrical vehicles, notebooks, and others. On the other hand, the primary cells can be used only once.

There are different secondary cells technology available on the market. The batteries present different characteristic and some of them must be taking into account during the battery selection process, such as: energy density, efficiency, capacity, lifetime and costs. In this work, the lead-acid and Li-ion batteries are considered. The lead-acid battery was selected since it is a consolidated product on the marked and the Li-ion battery was selected due to its great performance and the increasing usage of this technology in renewable energy projects.

2.1.1 Lead-acid Battery

Lead-acid batteries are the most mature electrochemical energy storage technology available on the market. Even though there are a large variety of lead-acid battery based on the design perspective, the operation principle for them is the same (Moseley; Rand; Peters, 2015). Basically, the operating principle of lead-acid batteries is based on the redox reaction in electrochemical cells. The positive electrode is based on lead dioxide,

the negative electrode is based on metallic lead, while the electrolyte is a sulfuric acid solution.

The lead-acid battery can be divided in open (vented) or sealed (valve-regulated). In open batteries, overcharge results in the conversion of water into hydrogen and oxygen gases, which are lost to the atmosphere. Therefore, the water needs to be added to this group of battery in a regular time. This fact increases the project maintenance. On the other hand, sealed rechargeable batteries hold only enough liquid to allow the electrolytes to flow (Moseley; Rand; Peters, 2015). These types of batteries are also known as maintenance-free batteries. There are two types of sealed rechargeable batteries: gel and Absorbed Glass Mat (AGM). Gel batteries contain a putty-like substance, while AGM batteries contain special acid-saturated fiberglass mats. AGM batteries are generally more powerful and cost-effective, but gel batteries offer more longevity (Moseley; Rand; Peters, 2015).

Due to the commercial maturity of the lead-acid battery, they present low cost and efficiency rate between 70 % and 85 %. In addition, the technology presents short response time (in the range of milliseconds), low-self-discharge rate (3 % to 20 % per month) (Ibrahim; Ilinca; Perron, 2008). On the other hand, the main drawbacks of this technology is its low energy density and capacity, poor performance at low temperatures and reduced cycling lifetime, which is very sensitive to the cycle depth. In addition, the lead acid battery presents a lower lifetime when compared to other batteries technology, such as the Li-ion batteries (Moseley; Rand; Peters, 2015).

In order to overcome some of their traditional drawbacks, advanced lead-acid batteries are under development or under early applications stage. For example, the applications of carbon in lead-acid batteries has presented great performance, since carbon materials are widely used as an additive to the negative active mass, as they improve the cycle life and charge acceptance of batteries, especially in high-rate state of charge (Moseley; Rand; Peters, 2015).

2.1.2 Li-ion Battery

This battery technology is widely used in portable electronic devices, such as cell phones, notebooks, watches and others. Li-ion batteries are lighter, smaller and more powerful than other batteries, which become more attractive for consumer electronics applications (Horiba, 2014). In addition, Li-ion batteries are more common in the market since they have been used in electrical power system application and electric vehicle (Divya; Ostergaard, 2009).

The main reasons behind the fast growth of this technology is the high energy density and cycling (Lopez et al., 2021). Li-ion cells are typically rated for much higher

charge and discharge powers than lead-acid cells, allowing them to absorb high pulses of generated power or meet sudden power demands. Basically, Li-ion batteries can use a number of different materials as electrodes. The most common combination is that of lithium cobalt oxide (cathode) and graphite (anode), which is most commonly found in portable electronic devices such as cell phones and laptops. Other cathode materials include lithium manganese oxide (used in hybrid electric and electric automobiles) and lithium iron phosphate (Horiba, 2014).

Furthermore, the Li-ion battery lifetime is superior than the lead-acid technology. According Molina (2017), the lifetime of the Li-ion battery is around 10-15 years and for the lead-acid this value is around 3-8 years. In addition, the low self-discharge rate and maintenance are also considered an advantages of this battery technology.

Even though the Li-ion battery presents better performance compared to lead-acid batteries, the costs for Li-ion batteries are still a limiting factor. In addition, Li-ion batteries have a tendency to overheat, and can be damaged at high voltages. In some cases this can lead to thermal runaway and combustion. Thus, based on these information, a comparative board between the lead-acid and Li-ion batteries are presented in Fig. 5.

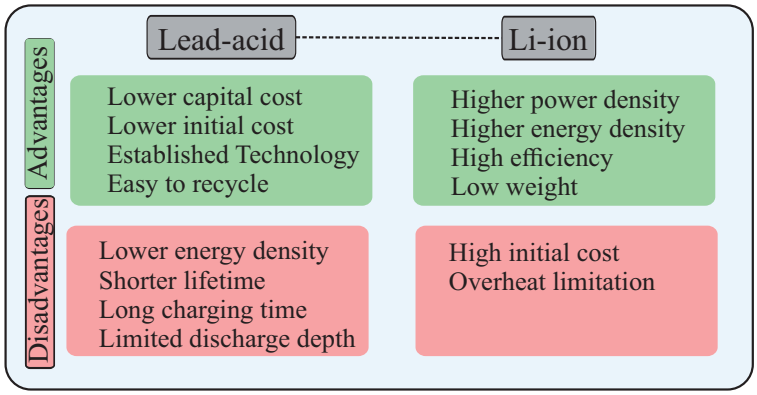

Figure 5 – Comparative board between lead-acid and Li-ion battery technologies.

Source: Own authorship.

2.2 Power Processing Structures for PV Inverters with BESS

Some of the most common structures of PV power converters connected BESS are presented in this sections. Thus, a state-of-art for the power conversion system (combined with BESS) applied to medium-high-power is presented.

2.2.1 Common dc-link and Two dc-dc Stages

The first topology presented is a common dc-link and two dc-dc stages, as presented in Fig. 6. As observed, the PV array and the battery bank are connected to a common dc-link. There is a dc-dc converter interfacing the PV array and the dc-link (converter 1). In generally, this dc-dc converter is a boost unidirectional chopper, which is responsible to perform the Maximum Power Point Tracker (MPPT) in the PV modules. In addition, there is a dc-dc converter (converter 2) interfacing the battery bank and the dc-link. This is a bidirectional converter which can act as a boost or buck converter, used to charge and discharge the batteries. Finally, there is a dc-ac stage (inverter) which is responsible to inject active or reactive power into the grid (Citro et al., 2011).

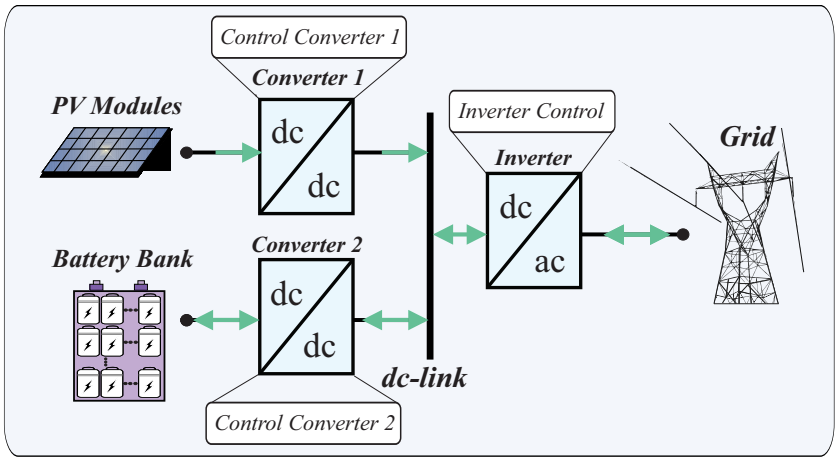

Figure 6 – Grid connected inverter with common dc-link and two dc/dc stages.

Source: Own authorship.

In this topology, three independent controls are considered: one for the dc/dc stage of converter 1, one for the dc/dc stage of converter 2 and one for the dc/ac stage of the inverter. Thus, this topology presents an easier control design (due to the independent control) and more optimized use of the battery bank (Sangwongwanich et al., 2018a). In addition, the batteries can be charged from the power generated by the PV models and also from the electrical grid. Specially for the control strategy of the converter 2, it is possible to add strategies to increase the reliability of the battery bank, since the charge and discharge process can be controlled (Sangwongwanich et al., 2018a).

Regarding the increase of the battery reliability, this topology can be improved by adding a supercapacitor in parallel to the battery bank, as presented in Fig. 7. The idea is to take the advantage of the combined use of the high-power device (supercapacitor) with the slow response (battery) (Xu et al., 2016). It is important to observe that the battery response time is in order of tens of milliseconds, which is satisfactory for several applications. Nevertheless, the use of the supercapacitor can avoid severe variation in the battery discharge current and increase the battery reliability.

Even though the supercapacitor combined with the battery bank presents those positive points, some drawbacks are also presented. The first one is the increases of the total power losses in the system, since three dc-dc stages are presented. Besides, the increasing of component in the system compared to the previous topology can affect the reliability of the entire system (Citro et al., 2011).

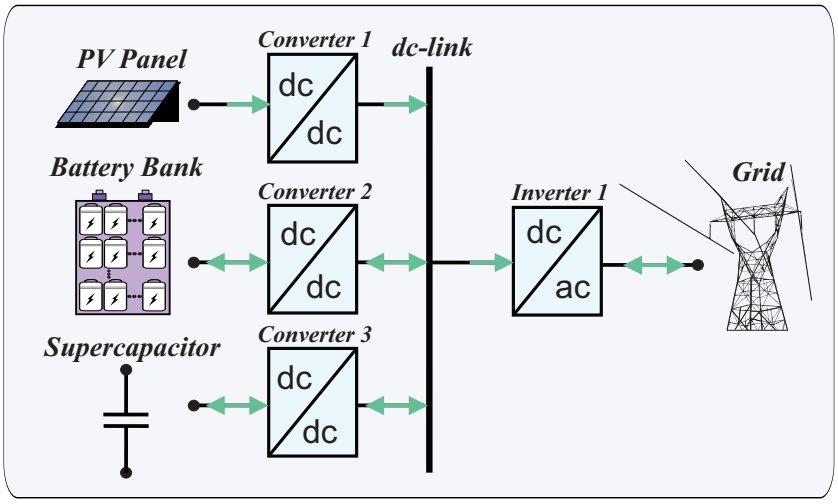

Figure 7 – Grid connected inverter with common dc-link and two dc/dc stages with supercapacitor.

Source: Own authorship.

2.2.2 Three-port Bidirectional Full Bridge Converter

The three-port bidirectional full bridge converter is presented in Fig. 8. As observed, three active full bridge converters, represented by Fb_1, Fb_2 and Fb_3 are implemented in this topology. In addition, the three converters are interconnected by a High Frequency (HF) transformer. The dc side of the Fb_1 is connected to PV modules, Fb_2 is connected to the BESS and Fb_3 is connected to the dc side of a grid-connected single-phase inverter.

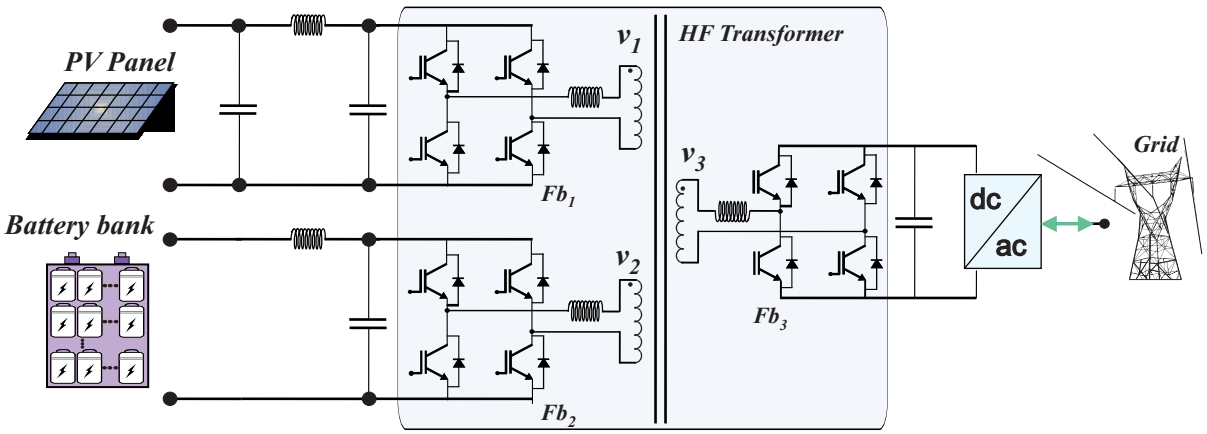

Figure 8 – Grid-connected inverter with three-port bidirectional full bridge converter.

Source: Own authorship.

The power flowing between the three ports depends on the phase shift between the square voltage v_1, v_2, and v_3. Considering v_1 as the voltage reference, the phase difference between v_1 and v_2 and between v_1 and v_3 can be used to regulate the power flow. In addition, Citro et al. (2011) proposed the regulation of the dc-link voltage v_3 to allow the inverter control system to manage the current injected into the grid regardless the dc-link voltage variations. The idea is to mitigate the oscillations in the power injected to the grid.

According to Falcones and Ayyanar (2010), this topology presents a considerable small size, low weight and a high reliability level. Moreover, different port voltage levels can be achieved in this topology. However, the main drawbacks is relate to the difficult design of the HF transformer, reduced soft switching operating range and high stress on the batteries. In addition, according to Citro et al. (2011), more test with high power flow should be performed and discussed.

2.2.3 Common ac Connection: Dual Inverter Topology

A dual inverter topology is presented in Fig. 9. As observed, this topology presents two separated inverter: one connected to the PV system and other connected to the battery bank. The PV inverter is responsible to inject the active power produced by the PV model to the grid. Generally, for three-phase inverters, it is not necessary a dc/dc stage (boost converter) interfacing the PV model and the inverter (Falcones; Ayyanar, 2010). Thus, the MPPT and the dc-link voltage control is performed by the inverter.

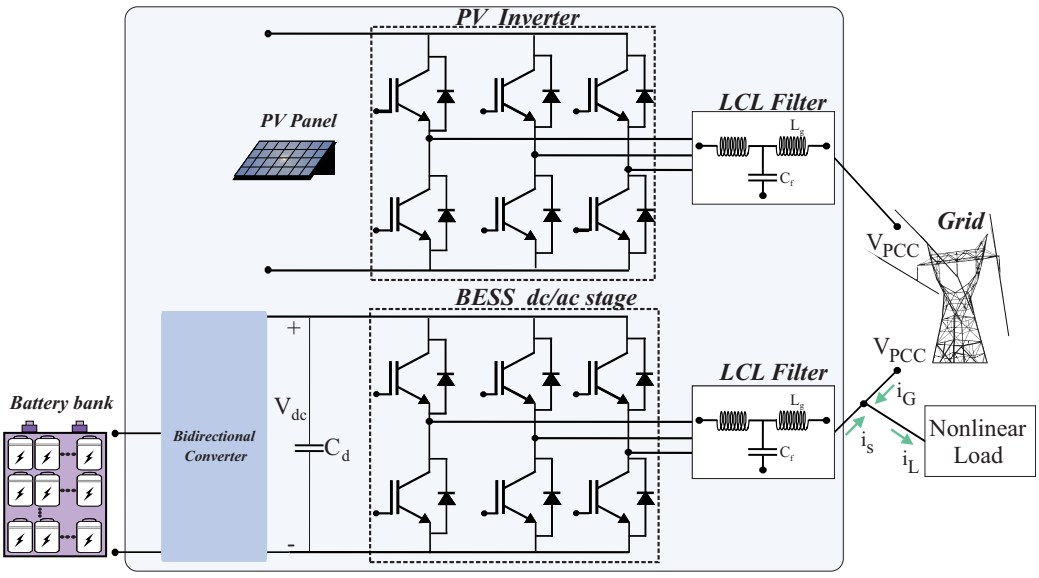

Figure 9 – Variation of a dual inverter topology.

Source: Own authorship.

The BESS dc/ac stage is connected to the battery bank. This inverter is responsible

to inject active power from the battery bank to the grid. In addition, BESS dc/ac stage can work as a rectifier operation to charge the battery bank with the grid power. A bidirectional converter interfacing the battery bank and the inverter is presented. This converter is important to support the control of the battery current during the charge and discharge process. The control strategy can be performed using the methodology proposed by (Manoranjan; Siva, 2014). In this topology, the dc-link voltage control can be controlled by the inverter or the bidirectional converter.

The structure presented in Fig. 9 is commonly used for peak shaving operation. Thus, the power produced from the PV system is used to charge the battery bank and inject it to the grid during the peak time. It is an interesting solution since avoid the use the energy from the grid when the energy price is higher. In addition, the BESS inverter can be used as auxiliary services, such as harmonic current compensation for nonlinear loads or reactive power injection. Therefore, this topology is used in this work as a case study.

The block diagram of the BESS dc-ac stage is presented in Fig. 10. The dc-link voltage is controlled by the outer loop. The amplitude of the fundamental current ($I_{bat}{}^{*}$) to be injected or drained from the grid is computed. The synchronization with the voltage at Point of Common Coupling (PCC) (V_{PCC}) is performed using a Second Order Generalized Integrator (SOGI) structure connected in cascade to a Synchronous Phase Locked Loop (PLL) (Rodríguez et al., 2011). Moreover, the load harmonic current ($i_L^*(t)$) is added to the fundamental current reference to generate the BESS reference current ($i_s^*(t)$). Finally, $i_s(t)$ is controlled by a Proportional Multi-resonant Controller (PMR).

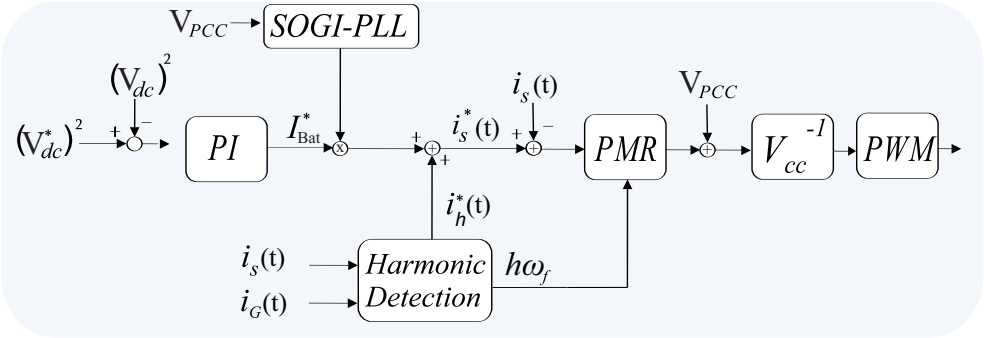

Figure 10 – Control block diagram of the BESS dc/ac stage.

Source: Own authorship.

2.3 Multiple Criteria Decision Making

The methods used in this work to select the battery for the BESS is described in this section. In this context, the MCDM is adopted. This tool involves both quantitative and qualitative factors. The main proposal of this tool is to select a best fit alternative

according to the goal (Farahani; SteadieSeifi; Asgari, 2010). In recent years, several MCDM techniques and approaches have been suggested to chose the optimal probable options, such as industries, food quality decision making, economics, material selection, investment decision, project evaluation and staff appraisal (Jha et al., 2014; Vucijak et al., 2013).

In the MCDM technique, some methods, such as TOPSIS, are commonly used in the selection process. This method was proposed by Hshiung, Dieckerhoff and Huang (1981) and it is able to select and order the input parameters based on the weights chosen by the user. The main conception of the method is based on the idea that the best alternative should have the shortest distance from an ideal solution. TOPSIS method assumes that if each attribute takes a monotonically increasing or decreasing variation, then it is easy to define an ideal solution. Thus, a solution is composed of all the best attribute values achievable, while the worst solution is composed of all the worst attribute values achievable. Therefore, TOPSIS finds a solution which has the shortest distance from the ideal solution in the Euclidean space.

This method was previous used for applications such as material selections (Thakker et al., 2008). In addition, TOPSIS method was also used by the Panday and Bansal (2016) for the battery selection in hybrid electric vehicle applications. Therefore, the TOPSIS method is used in this work to select the best battery for the projects in PV systems. Thus, different batteries with different characteristics, such as, power losses, lifetime, cost and volume are used as comparative parameters. In this context, the TOPSIS model is used to decide which battery presents the better performance based on the selected criteria.

In the TOPSIS method, it is necessary to define the weights of the criteria. Thus, in this work, the AHP is used to find the weights for the TOPSIS method. This method is a powerful multicriteria decision-making tool which has been used in numerous applications in various fields of economics, politics and engineering (Chai; Liu; Ngai, 2013). With the AHP method, the user can give his opinion in the criterion importance level. The application of these methods are discussed in the next chapters of this thesis.

2.4 Lifetime Evaluation Methods

In this section, the lifetime evaluation for some components which are more common to fail in a BESS are presented. Regarding to the dc/ac stage, the lifetime evaluation of the semiconductor devices and the dc-link capacitor are performed. Those components are considered the most failure rates inside the inverter (Ma; Wang; F. Blaabjerg, 2016; Falck et al., 2018). According to Falck et al. (2018), a survey was applied to a group of power electronic manufactures asking about the components which presents

the most failure in PV inverters. As results, it was observed that semiconductor devices and dc-link capacitor are the most fragile components, achieving almost 50 % of the total number of adressement failure.

Regarding the BESS, the batteries lifetime is expected to be shorter than the lifetime of others converters components, such as capacitors, inductors and semiconductors devices (Stroe et al., 2014). In addition, the lifetime evaluation method for lead-acid and Li-ion batteries present different characteristics. The lifetime evaluation methods adopted in this work are described in the following subsections.

2.4.1 Lead-acid Battery Lifetime

The lifetime evaluation of the battery model is an important topic to be considered when a BESS is present in the project. Regarding the lead-acid battery, there are some methods available in the literature. A very used method is the equivalent full cycle to failure (Bernal-Agustín; Dufo, 2009). Basically, this method defines the end of the battery lifetime when a specified number of full charge and discharge cycles are reached. Thus, based on the information provided by the datasheet, it is possible to quantify the effect on the battery lifetime. Another used method is the rainflow cycles counting (Downing; Socie, 1982). This method uses the rainflow algorithm to count the number of cycles achieved by the battery during a mission profile operation.

The methods equivalent full cycle and rainflow cycles counting are easy to be implemented and present a low processing time. However, those methods do not consider important factor regarding the battery operation. In a lead-acid battery, many stress factors related to temperature and operation condition must be taking into account during the lifetime evaluation. Thus, the Schiffer method, proposed by Schiffer et al. (2007), is a common methodology that considers the most important stress factors in the lead-acid battery. This a very accepted model in the literature for lead-acid batteries, since it considers that operating conditions are typically more severe than those used in standard tests of cycling and float lifetime. Therefore, phenomenons such as corrosion, acid stratification, gassing, sulfation and sulfate crystal growth are taking into account (Schiffer et al., 2007). In fact, these phenomenons are modeled and used as weighted factor in the Schiffer model.

The lifetime model is developed for a single cell of the battery and it is adaptable for different lead-acid batteries. The input parameters can be easily found in the manufacture datasheet. In addition, the Schiffer model takes into account the battery power (P_{bat}) and battery temperature (T_{bat}) mission profile, which guarantee the evaluation of the battery operation effects in the aging process. Other important point about this model is the update of the output parameters in each step time of the mission profile. Therefore, it is possible to observe the degradation process with the time in parameters (for example

the internal resistance) used in the lifetime evaluation. Even though Schiffer method presents a more complex implementation and processing time, the estimated lifetime is more accurate and accepted in the literature. The flowchart for the lead-acid battery is presented in Fig. 11.

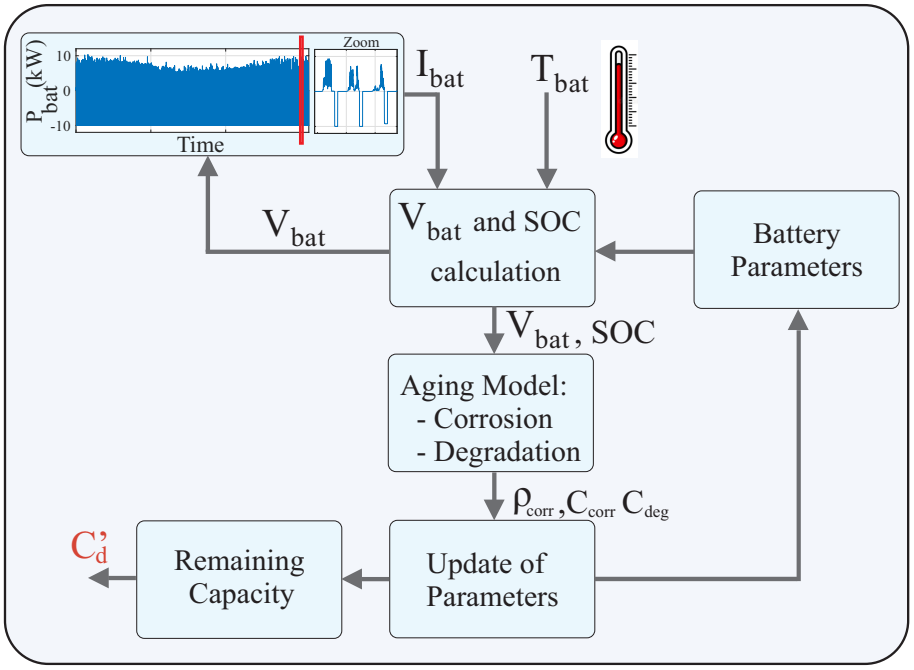

Figure 11 – Flowchart for the lifetime evaluation of Lead battery proposed by Schiffer et al. (2007).

Source: Own authorship.

As observed, the battery temperature and the battery power mission profile are considered input of the model. The Stage of Charge (SOC) estimation is the first step of this method. V_{bat} is the voltage of a single cell and it is estimated based on the Shepherd equation (Manoranjan; Siva, 2014), as shown:

$$V_{bat}(t) = U_0 - gDOD(t) + \rho_c(t)\frac{I_{bat}(t)}{C_N} + \rho_c(t)M_c\frac{I_{bat}(t)}{C_N}\frac{SOC(t)}{C_c - SOC(t)}, \forall I_{bat}(t) > 0 \quad (2.1)$$

$$V_{bat}(t) = U_0 - gDOD(t) + \rho_d(t)\frac{I_{bat}(t)}{C_N} + \rho_d(t)M_d\frac{I_{bat}(t)}{C_N}\frac{DOD(t)}{C_d - DOD(t)}, \forall I_{bat}(t) < 0 \quad (2.2)$$

where $U_0[V]$ is the open-circuit equilibrium cell voltage at the fully-charged state; $g[V]$ is an electrolyte proportionality constant; the Depth of Discharge (DOD) is defined as $(1 - \text{SOC})$; ρ_c and ρ_d [Ω Ah] are the aggregated internal resistance; C_N is the nominal capacity; M_c and M_d are is the charge-transfer overvoltage coefficient and C_c/C_d is the normalized capacity. With V_{bat} and P_{bat} is possible to estimate the battery current (I_{bat}).

Therefore, the SOC can be calculated by the following equation:

$$SOC(t) = SOC(0) + \int_0^t (I_{bat}(t) - I_{gas}(t))dt, \tag{2.3}$$

where $I_{gas}(t)$ is the gassing current. As observed, depending on the battery voltage not all the charge is stored as chemical bound charge in the battery, since there is a lost due to gassing. The higher voltage of the battery, more gas is developed and less of current is actually converted to change of SOC (Schiffer et al., 2007). The gas current can be calculated as:

$$I_{gas}(t) = \frac{C_N}{100} I_{gas,0} \exp\left(c_u(V_{bat}(t) - U_{gas,0}) + c_T(T_{bat}(t) - T_{gas,0})\right), \tag{2.4}$$

where $I_{gas,0}$ is the normalized gassing current for 100 Ah nominal battery capacity at nominal voltage ($U_{gas,0}$) and nominal temperature ($T_{gas,0}$). c_u and c_T are the voltage and temperature coefficients, respectively.

Since the battery voltage and SOC are estimated, the aging model is performed in the Schiffer model. Basically, the aging model can be divided in corrosion (C_{corr}) and degradation (C_{deg}) mechanisms. The C_{corr} is based on the corrosion process, which is an aging mechanism typically for lead-acid battery. This phenomenon is related to the internal resistance increasing. Schiffer model adopts the concept of a corrosion layer with lower conductivity, which grows during the lifetime of the battery. Thus, for each simulation time step, the corrosion layer thickness ($\Delta W(t)$) is calculated (Schiffer et al., 2007). This calculation is related to the voltage corrosion, as presented:

$$(U_{corr} < 1.74), \Delta W(t) = k_s \left[\frac{\Delta W(t - \Delta t)^{\frac{1}{0.6}}}{k_s} \right]^{0.6}, \tag{2.5}$$

$$(U_{corr} \geq 1.74), \Delta W(t - \Delta t) + k_s \Delta t, \tag{2.6}$$

where Δt is the duration of one time step of the I_{Bat} mission profile and k_s is the corrosion speed parameters, which implies the increase in the corrosion layer with the time. In addition, k_s is calculated based on Arrhenius' law:

$$k_s(U_{corr}, T_{bat}) = k(U_{corr}) \exp\left(k_{s,T_{bat}}(T_{bat} - T_{corr,0})\right), \tag{2.7}$$

where $k(U_{corr})$ is a corrosion speed/voltage based on the Lander curve, proposed by Lander (1956). Also, the temperature factor $k_{s,T_{bat}} = \ln(2)/15$ K reflects the fact that the corrosion speed doubles for a temperature increase of 15 K or it slows down at low temperatures. In addition, the $T_{corr,0}$ equal to 298 K is used (Schiffer et al., 2007).

Therefore, with the battery time operation, $\Delta W(t)$ increases affecting the battery internal resistance(ρ_{corr}) and the capacity loss due to the corrosion process (C_{corr}), as presented in Eq.(2.8) and Eq.(2.9), respectively.

$$\rho_{corr} = \rho_{corr,lim}\frac{\Delta W(t)}{\Delta W_{lim}}, \tag{2.8}$$

$$C_{corr} = C_{corr,lim}\frac{\Delta W(t)}{\Delta W_{lim}}, \tag{2.9}$$

where $C_{corr,lim}$ and $\rho_{corr,lim}$ are the limit of capacity loss and resistance by corrosion process, respectively. In addition, ΔW_{lim} is the corrosion layer thickness when the battery has reached the end of its float lifetime (given in the battery datasheet).

The degradation aging process takes into account the cycling behavior of the battery. Therefore, depending of the battery power and temperature mission profile, the lifetime can be shorter than it is expected. Some references evaluate this aging process analyzing only the number of IEC standard cycles (Z_{IEC}), which is the number of IEC cycles (ZIEC) given in the battery datasheet. Thus, depending of the battery DOD, the number of cycles are computed. On the other hand, Schiffer model takes into account those phenomenons by using the following equation to estimate the number of cycles (Z_W):

$$Z_W(t+\Delta t) = Z_W(t) + \frac{|I_d(t)| f_{SOC}(t) f_{acid}(t)\Delta t}{C_N}, \tag{2.10}$$

where the number of cycle is weighted with the impact of the SOC variation ($f_{SOC}(t)$), the discharge current $I_d(t)$ and the acid stratification factor (f_{acid}). The modeling of $I_d(t)$, $f_{SOC}(t)$ and f_{acid} are explained in detail by reference Schiffer et al. (2007). In addition, the Z_W is updated in each simulation step time (Δt).

The capacity loss due to the degradation process (C_{deg}) is presented in:

$$C_{deg} = C_{deg,lim} e^{-c_z\left(1-\frac{Zw(t)}{1.6Z_{IEC}}\right)}, \tag{2.11}$$

where $C_{deg,lim}$ is the capacity at the end of the battery life (i.e. 80% of nominal capacity) and c_Z is a constant equal to 5.

Finally, the remained capacity ($C'_d(t)$) is calculated considering initial battery capacity $C'_d(t=0)$ subtracted by the capacity losses due to the corrosion and degradation process, as presented in Eq.(2.12). Thus, when $C'_d(t)$ represents 80% of the nominal capacity, the battery achieves the end of life.

$$C'_d(t) = C'_d(t=0) - C_{corr} - C_{deg}. \tag{2.12}$$

2.4.2 Li-ion Battery Lifetime

The lifetime model used for Li-ion batteries was proposed by Stroel Ioan (2014). This model considers aging process due to two important factors, which are the cycling

and calendar mechanims. The cycling are related to the battery power cycling and the calendar is related to the idle operation mode. The flowchart for the lifetime evaluation is presented in Fig. 12.

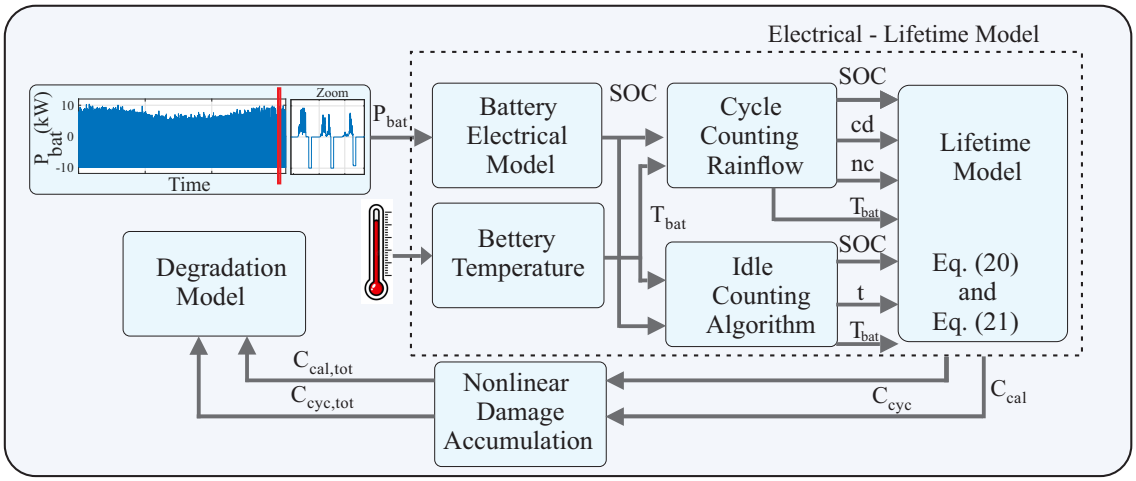

Figure 12 – Flowchart for Li-ion battery lifetime proposed by (Stroel Ioan, 2014).

Source: Own authorship.

Active power mission profile is used to obtain the SOC mission profile, from the battery electrical equivalent model presented by (Stroel Ioan, 2014) . Based on the operation conditions, the parameters such as internal resistance and battery capacity are monthly updated based on the calendar and cycling aging process. Based on the battery power mission profiles, the SOC estimation is performed. Thus, the SOC mission profile is used in the cycle counting rainflow and idle counting algorithm to extract the main parameters of each charge/discharge cycle and idle operation cycle. Thus, it is possible to estimate the capacity fade due to cycling (C_{cyc}) and calendar degradation (C_{cal}) processes. The equation modeled for the cycling capacity fade is presented in Eq.(2.13) (Stroel Ioan, 2014):

$$C_{cyc} = 2.6418^{-0.01943SOC} 0.004 e^{0.01705 T_{bat}} 0.0123 cd^{0.7162} nc^{0.5}, \tag{2.13}$$

where nc is the number of cycle, SOC is the average state-of-charge in each cycle, dc is the battery DOD in percentage. The total capacity fade is computed by the non-linear accumulation process. Thus, it is necessary to use a strategy to accumulate these values and find the total capacity fade due to the cycling aging process $C_{cyc,tot}$. Therefore, a nonlinear accumulation strategy is used in this work, as presented in Eq.(2.14):

$$C_{cyc,tot} = \sqrt{C_{cycle,actual}{}^2 + C_{cycle,previous}{}^2}, \tag{2.14}$$

where $C_{cycle,actual}$ is the the accumulation of the actual month cycling capacity fade and $C_{cycle,previous}$ is the previous month cycling capacity fade.

Regarding the calendar capacity fade estimated in each month, the Eq.(2.15) is proposed by Stroel Ioan (2014):

$$C_{cal} = 1.9775.10^{-11} e^{0.07511 T_{bat}} 1.639 e^{0.007388 SOC} t^{0.8}, \tag{2.15}$$

where t is the time that the battery stay in idling mode, in months, SOC is the state of charge stationary in each idle period, in percentage, and T_{bat} is giving in Kelvin. In addition, the strategy to accumulate the capacity fade ($C_{cal,tot}$) due to the calendar operation mode is presented:

$$C_{cal,tot} = \left[{C_{cal,actual}}^{\frac{8}{10}} + {C_{cal,previous}}^{\frac{10}{8}} \right]^{\frac{10}{8}}, \tag{2.16}$$

where $C_{cal,actual}$ is the actual month calendar capacity fade and $C_{cal,enprevious}$ is the previous month calendar capacity fade.

Finally, the total capacity fade ($C_{fade,tot}$) due to the cycling and calendar capacity fade is shown in Eq.(2.17). Therefore, considering the battery capacity achieve a loss of 20 % in relation to the nominal capacity, the battery have reached its end-of-life.

$$C_{fade,tot} = C_{cal,tot} + C_{cyc,tot}. \tag{2.17}$$

2.4.3 Semiconductor Devices Lifetime

According to Reigosa et al. (2016a), the semiconductors devices of inverter has been reported as the failure-prone component in PV plants. In this context, the Physics of Failure (PoF) becomes a consolidated approach to understand the root causes of failure in power devices (Ma; Wang; F. Blaabjerg, 2016). PoF takes into account the load profiles, considering the stress in the real field operation. Irradiance (G) and ambient temperature mission profiles are commonly employed in PV systems (Ma et al., 2015).

Previous works have concluded that the mean junction temperature (T_{jm}), the junction temperature fluctuation (ΔT_j) and the heating time (t_{on}) affect the semiconductor lifetime consumption (Ma et al., 2015). Moreover, the semiconductor device thermal loading for the inverter is estimated considering two thermal cycling stresses: long cycles and short cycles (Reigosa et al., 2016a; Ma et al., 2015). The former considers the damage caused by the mission profile variation, which is related to environmental conditions, such as solar irradiance and ambient temperature (Reigosa et al., 2016a). Therefore, the long cycle depends on the sampling time (T_s) of the mission profile. The latter considers the damage caused by power cycling due to line frequency (f_n) (50/60 Hz) (Ma et al., 2015). The short and long cycles are presented in the Fig. 13.

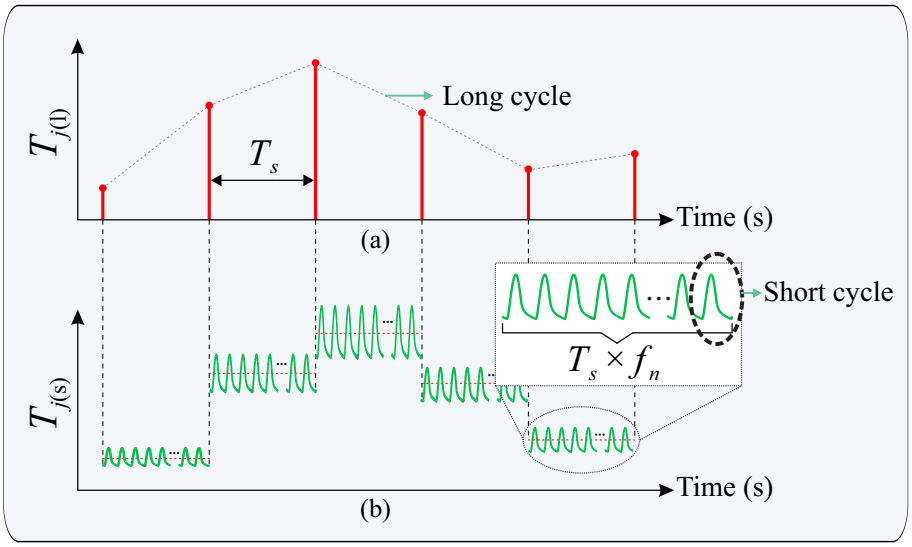

Figure 13 – Thermal cycles representation: (a) long cycle thermal and (b) short cycles.

Source: Own authorship.

The flowchart for the lifetime evaluation of the semiconductor devices is presented in Fig. 14. As observed, the lifetime consumption is based on look-up tables. Considering the BESS inverter operation, the power losses (P_{loss}) of the semiconductor device depend on the active power provided or received by the battery bank and the T_{jm}. Therefore, in a PLECS simulation environment, the parameters of the active power and T_{jm} are varied to generate the power losses look-up table. The conduction and switching losses of the power devices are stored in the look-up tables. More detail about the simulation environment is given in Chapter 4.

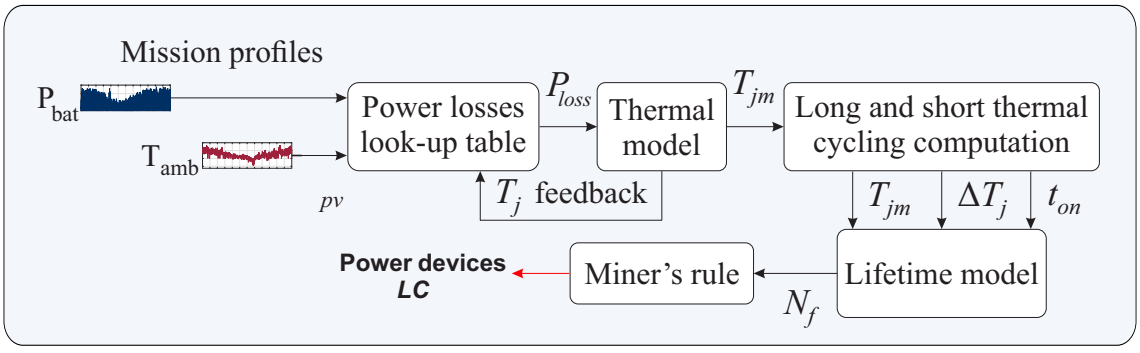

Figure 14 – Flowchart for the lifetime evaluation of the semiconductor devices.

Source: Own authorship.

The power losses are estimated based on information provided by the manufacturer's datasheets. For the conduction losses, the on-state characteristics of the semiconductors devices are considered. For the switching losses, the energy loss during the turn-on and turn-off switching is used. Temperature dependence of the losses are included in the model as well. The creation of power losses look-up table is presented in Fig. 15.

The power losses are applied to an electro-thermal model, which extracts the T_{jm}

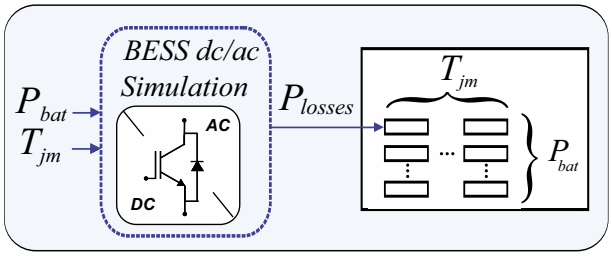

Figure 15 – Power losses look-up table generation process.

Source: Own authorship.

using the thermal circuit, proposed by Ma et al. (2015). This approach is composed of the combination of Foster and Cauer thermal impedance model. Thus, this technique takes the advantages of the two models, and achieves a more accurate junction temperature estimation. In addition, all the information necessary in the thermal model is obtained from the datasheet.

Since the junction temperature is estimated, it is used a rainflow counting algorithm to convert the randomly thermal profile into regulated thermal cycle, which is needed to compute the lifetime consumption (Ma et al., 2015). Rainflow counting has become the most widely accepted method for the processing of random signals for fatigue analysis, and tests have demonstrated good agreement with measured fatigue lives when compared to other counting algorithms. Thus, the parameters of T_{jm} , ΔT_j and t_{on} are estimated. Those parameters are used in the long cycle lifetime evaluation, since they are varied due to the mission profile operation of the BESS.

Power cycling due to line frequency strongly affects the semiconductor lifetime consumption (Yang et al., 2015; Shen et al., 2016). Thus, the short cycle lifetime evaluation analyzes the damage caused to the semiconductor device in a period equal to $1/f_n$. As observed, the sampling time of the mission profile needed in this study is difficult to obtain, since the data must be acquired with a high sampling rate.

Therefore, there are some methods in the literature to estimate the parameter of T_{jm}, ΔT_j and t_{on} during the short cycle. One of the most used lifetime estimation methods applied to short cycles is proposed by Ma and F. Blaabjerg (2012). This technique approximates the almost sinusoidal power losses waveform to two step square wave pulses, keeping the area constant, as observed in Fig. 16 (a)-(b).

By doing so, the junction temperature fluctuation can be obtained from analytical equations for a given set of heating times, in which the square pulses occur. In addition, when the BESS is injecting only fundamental current to the grid, the inverter current is almost perfectly sinusoidal. In this case, the ΔT_j can be obtained using an analytical equation, depending on the square waveform previously defined, as observed (Ma; F. Blaabjerg, 2012):

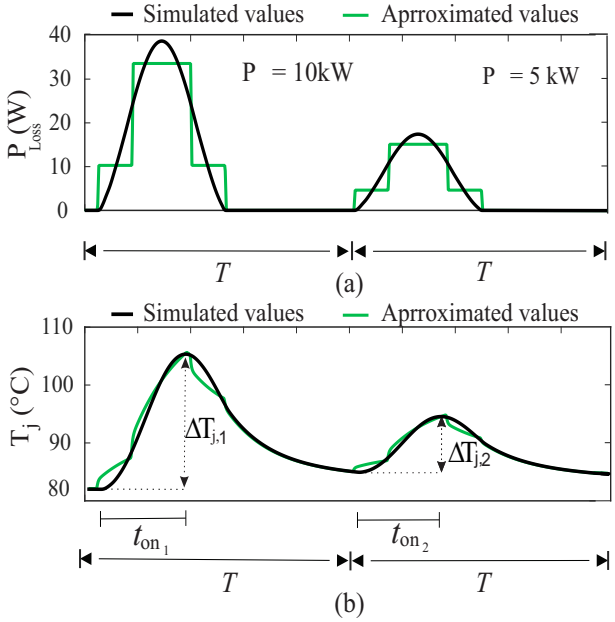

Figure 16 – Inverter injecting fundamental current to the grid: (a) average power losses and (b) junction temperature.

Source: Own authorship.

$$\Delta T_j = P_{avg} Z_{th}(t_1) + (3P_{avg} - P_{avg}) Z_{th}(t_2 - t_1), \tag{2.18}$$

where P_{avg} represents the average power losses in one cycle period, Z_{th} is the thermal impedance of the semiconductor device, $t_1 = 1/(8f_n)$ and $t_2 = 3/(8f_n)$. The heating time coincides with the time when the junction temperature is determined. Even though t_{on} is not exactly the same for each range of active power, it is considered constant to be applied in the lifetime model. Therefore, the value of t_{on} is fixed in $1/(2f_n)$ (Reigosa et al., 2016a).

Finally, for both thermal cycling, the number of cycles until failure (N_f) of the power semiconductor devices is estimated by the following lifetime model, proposed by Scheuermann, Schmidt and Newman (2014):

$$N_f = A(\Delta T_j)^{\alpha} (ar)^{\beta_1 \Delta T_j + \beta_0} \left[\frac{C + (t_{on})^{\gamma}}{C + 1} \right] \exp\left(\frac{E_a}{k_b T_{jm}} \right) f_d, \tag{2.19}$$

where the meaning and values of the parameters A, α, β_1, β_0, C, γ, E_a and f_d are defined in Scheuermann, Schmidt and Newman (2014). k_b is the Boltzmann constant and ar equal to 0.35 is used in this work. Besides, the parameter f_d is equal to 1 to calculate the N_f of Insulated Gate Bipolar Transistor (IGBT)s, as proposed by Scheuermann, Schmidt and Newman (2014).

The power devices lifetime consumption (LC) can be computed by using the Miner's rule, represented as follows (Huang; Mawby, 2013):

$$LC = \sum_{k} \left(\frac{1}{N_{f,l(k)}} + \frac{T_s \times f_n}{N_{f,s(k)}} \right), \tag{2.20}$$

where indexes l and s correspond to the long and short thermal cycling, respectively. As observed, the power devices LC is given by a cumulative sum of the damages caused by the long and short cycles.

2.4.4 dc-link Capacitor Lifetime

The dc-link capacitor is classified as electrolytic capacitors (al-caps). The lifetime evaluation of this component is also similar to the semiconductor devices, since the mission profile of solar irradiance and ambient temperature are taking into account. Furthermore, the power losses of the component are also translated to temperature profiles, which are used in the lifetime evaluation process.

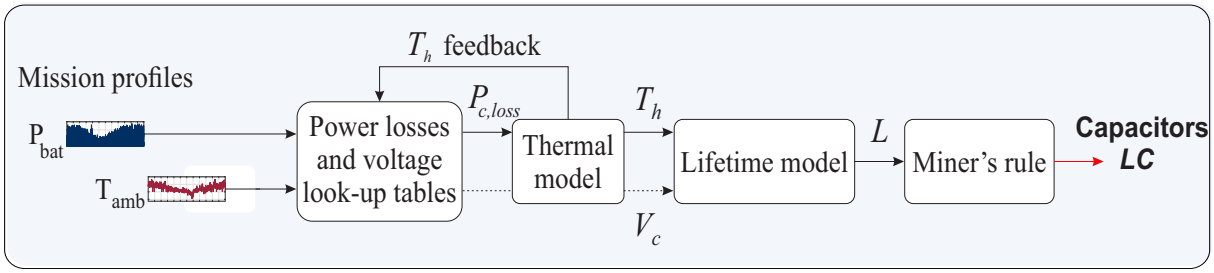

Figure 17 – Flowchart for the lifetime evaluation for the dc-link capacitor.

Source: Own authorship.

Fig. 17 summarizes the steps for lifetime evaluation of dc-link capacitors. The main stress factors are the hot-spot temperature (T_h) and operating voltage (V_c) (Falck et al., 2018; Wang; Blaabjerg, 2014). The T_h is estimated based on the capacitor power losses, which are calculated as:

$$P_{c,losses} = \sum_{i} ESR(T_h, i\omega_n) I^2_{i(RMS)}, \tag{2.21}$$

where $I_{i(RMS)}$ is the RMS value of each i-th harmonic component of the capacitor current and ESR is the capacitor equivalent series resistance. ESR is a function of the capacitor current frequency and the hot-spot temperature, parameters usually provided by the capacitor manufactures (Lenz; Pinheiro, 2018). Thus, for the capacitor ESR estimation, a look-up table based on the al-cap datasheet data is used. Other approaches to extracting the ESR can be found in (Sundararajan et al., 2020). Since the capacitor power losses are computed, T_h can be estimated by (Lenz; Pinheiro, 2018):

$$T_h = T_{amb} + R_c P_{c,losses}, \tag{2.22}$$

where R_c correspond to capacitor equivalent thermal resistance. Them, the time to failure (L) of the capacitor is obtained by (Wang; Blaabjerg, 2014):

$$L = L_0 \left(\frac{v_{dc}}{v_0} \right)^{-n} \times 2^{\frac{T_0 - T_h}{10}}, \tag{2.23}$$

where L_0 is the lifetime under testing conditions. In addition, v_{dc} is the capacitor voltage, v_0 is the rated voltage at test condition and T_0 is the temperature under test condition. As the lifetime of al-caps quite depends on the voltage stress level, the value of the voltage stress exponent n equal to 3 is used in this work, as suggested in Wang and Blaabjerg (2014). Finally, the capacitor lifetime consumption can be determined by the Miners rule:

$$LC = \sum_k \left(\frac{T_s}{L_k} \right), \tag{2.24}$$

where k is the number of samples of the mission profile.

2.4.5 Monte-Carlo Simulation

The previous lifetime evaluation methodologies return in fixed accumulated damage. However, this approach is far from reality, since deviations from model parameters are not considered. Thus, a statistical approach based on Monte-Carlo simulation is conducted, according to (Reigosa et al., 2016b). The Monte-Carlo analysis is simulated for n = 10,000 samples with 5 % of variation over the static values, and the result is fitted using the Probability Density Function (PDF) $f(x)$. The component unreliability is evaluated by the Cumulative Density Function (CDF) $F(x)$, calculated from $f(x)$. The parameters used in the Monte Carlo simulation method are based on the reference (Reigosa et al., 2016b).

The system wear-out failure probability F_s is obtained with the series-connected reliability model, given by:

$$F_s = 1 - \prod_{j=1}^{n_I} (1 - F_I(x)) \prod_{j=1}^{n_D} (1 - F_D(x)) \prod_{j=1}^{n_C} (1 - F_C(x)), \tag{2.25}$$

where $F_I(x)$, $F_D(x)$ and $F_C(x)$ are the unreliability functions of the IGBTs, diodes and dc-link capacitor, respectively. n_I, n_D and n_C are the number of IGBTs, diodes and dc-link capacitor in the analyzed system.

2.5 Chapter Conclusions

In this chapter was presented a literature review about the main methods and topics which are discussed in this work. Firstly, a brief presentation about the batteries

technologies are shown. Thus, the lead-acid and Li-ion batteries are shown. In addition, some of the main power processing structures of PV inverters connected to the BESS are presented. Regarding to the battery selection process, the MCDM methods (TOPSIS and AHP) are shown. Finally, some of the proposed lifetime methods in the literature for the BESS elements are presented (the batteries, semiconductors and dc-link capacitor lifetime methods). In the next chapter, the proposed methodology to select the battery for a BESS are presented.

3 Methodology for BESS Design Assisted by Choice Matrix Approach

The battery choice employed in BESS projects is not a straightforward task, since there are several criteria which should be take into account in the battery selection process. Therefore, this chapter proposes a methodology to select the battery which will be used in general project. Thus, six criteria are considered in this work: dc-link voltage of the BESS inverter, battery lifetime, battery bank volume, battery bank power losses, battery bank cost and battery bank storage capacity index. The MCDM is used to select the optimum battery based on the relative importance between the OPEX and CAPEX concepts. The methodology proposed in this work is applied to 27 batteries composed by lead-acid and Li-ion batteries. The idea is to select the optimum battery solution for a BESS based on the peak shaving operation mode.

3.1 Storage System Design

As explained, this chapter proposes a methodology to select the optimum battery to be used in a BESS application. Firstly, the battery bank is sized. The battery bank sizing consist of three steps: the minimum number of battery, the voltage limits of the battery bank and the battery bank design. Each step is described in the next subsections.

3.1.1 Step 1: Minimum Number of Battery

The first step determines the minimum number of batteries (N_{min}) required for the BESS application. The N_{min} value is obtained based on the criterion of the energy and power requirements. The minimum number of batteries based only on the energy requirement (N_{En}) is calculated by:

$$N_{En} = \text{ceil}\left(\frac{100E_n}{E_{bat}(SOC_{max} - SOC_{min})}\right), \tag{3.1}$$

where E_n is the energy requirement for the BESS application and E_{bat} is the energy stored by a single battery. Also, the function "ceil" is responsible to compute the smallest integer find. In addition, the operation limits of the SOC is also taken into account. Thus, the interval between the maximum and minimum SOC values (SOC_{max} - SOC_{min}) is used.

Similarly, the minimum number of battery based on the power requirement (N_{P_n}) is calculated by:

$$N_{P_n} = \text{ceil}\left(\frac{P_n}{V_{batmin} C_n C_r}\right), \tag{3.2}$$

where P_n is the power required by the BESS application and V_{batmin} is the minimum voltage of a single battery considering the SOC_{min}. In addition, the C-rate (C_r) and the nominal battery capacity (C_n) are also taken into account.The C_r is the unit battery experts used to measure the speed at which a battery is fully charged or discharged. Depending on the BESS application, different strategies can be performed to find the parameters of E_n and P_n.

Thus, based on the results obtained from the Eq.(3.1) and Eq.(3.2), the minimum number of batteries based on the energy and power requirements is selected by the maximum value between N_{En} and N_{P_n}, as presented in the following equation:

$$N_{min} = \max\left(N_{E_n}, N_{P_n}\right). \tag{3.3}$$

3.1.2 Step 2: Voltage Limits of the Battery Bank

Since N_{min} is calculated, the maximum (V_{bmax}) and minimum voltages (V_{bmin}) of the battery bank are estimated. In this context, the voltage range of the battery bank and the dc-link voltage of the BESS dc/ac stage (V_{dc}) are presented in Fig. 18 for the sake of clarity.

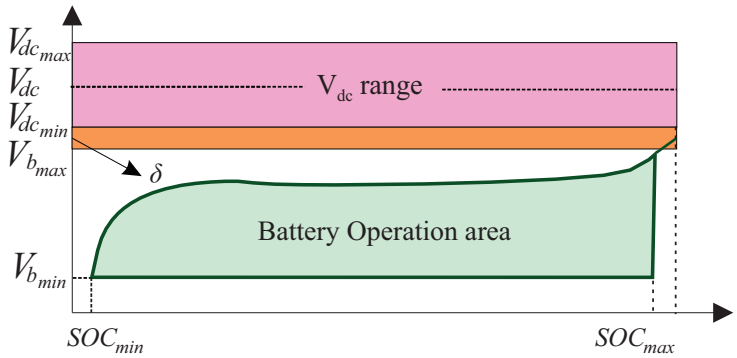

Figure 18 – Voltage representation of the BESS dc/ac stage dc-link voltage and voltage limits of the battery bank.

Source: Own authorship.

As observed, the battery bank has a range voltage between the minimum and maximum voltage (V_{bmin} - V_{bmax}), which is defined by the voltage at the maximum and minimum SOC specification. In addition, the dc-link voltage of the BESS dc/ac stage also presents a range of operation, which is defined by the maximum and minimum dc-link voltage (V_{dcmax} - V_{dcmin}). The V_{dcmax} is chosen based on the safe voltage supported by the semiconductor device. Generally, in terms of project, the maximum value used is around

75% of the blocking voltage provided by the semiconductor device manufacture (Infineon, 2014). On the other hand, the V_{dcmin} voltage is chosen based on the methodology proposed by (Cupertino et al., 2020), in which the minimum voltage necessary to inject reactive power into the grid (work in the linear conditions of modulation) parameters is calculated based on the grid parameters, as follows:

$$V_{dcmin} = 1.05\hat{V}_g(1 + \Delta V_g + x_{pu}), \tag{3.4}$$

where $\hat{V}_g$ is the peak of the line-to-line neutral voltage, ΔV_g is the maximum ac grid voltage variation (in pu) and x_{pu} is the per unit equivalent output impedance of the inverter. More information about this parameters can be find in reference (Cupertino et al., 2020).

3.1.3 Step 3: Battery Bank Design

In this step, the association of number batteries in series (N_s) and parallel (N_p) are estimated. In this sense, an important point to be analyzed is the voltage margin (δ) between the maximum battery bank voltage and minimum dc-link voltage of the BESS dc/ac stage. Since the inclusion of a dc-dc stage is considered in the battery bank design, the margin guarantees a better performance of the dc-dc stage during the battery charging and discharging processes. In this work, δ equal to 1 was used. However, this margin may be adopted (δ higher than one) to guarantee an acceptable dynamic performance of the dc/dc converter control. Thus, the number of batteries in series and parallel can be estimated, for a given V_{dc}, by the following equations, respectively:

$$N_s = \text{floor}\left(\frac{V_{dc}}{V_{batmin}\delta}\right). \tag{3.5}$$

$$N_p = \text{ceil}\left(\frac{N_{min}}{N_s}\right). \tag{3.6}$$

The total number of batteries (N_T) is calculated as $N_s.N_p$. As observed, depending on the V_{dc} value, different configurations of N_s and N_p can be obtained. The V_{dc} value ranged from V_{dcmin} to V_{dcmax} was applied to Eq.(3.5) and Eq.(3.6). Then, the configuration which presents the lowest N_T is selected. If the N_T repeats for more than one V_{dc} value, then the combination with the lowest V_{dc} is considered.

3.2 Battery Selection Criteria

Once the optimal number of batteries was selected, some important characteristics of the battery bank are analyzed to select the best battery for the application. In this work, six criteria are considered: dc-link voltage of the BESS inverter, battery bank volume,

battery bank power losses, battery bank cost, battery lifetime and storage capacity index. Each of these criterion is described in the following subsections.

3.2.1 dc-link Voltage of the BESS dc/ac Stage

The dc-link voltage of the BESS is important for the battery selection process, since it directly affects the reliability of the power electronic components. Thus, when the voltage of the battery bank increases, the switching power losses of the semiconductor devices (of the dc-dc stage) also increase (Feix et al., 2009). Consequently, the junction temperature of the semiconductor devices increases, which leads to thermal stress and reduces reliability of the the semiconductor devices, as presented by (Sangwongwanich et al., 2018b; Reigosa et al., 2016b). Therefore, the V_{dc} is an interesting variable to be analyzed since it directly impacts the power losses of the BESS dc/ac stage.

3.2.2 Battery Bank Volume

The battery bank volume (Vl_b) is an important parameter for battery decision. For large battery bank volume, issues related to the physical construction and transportation can be limiting factors. For each battery, the Vl_b can be calculated by multiplying the N_T by the volume of a single battery (Vl_{bat}):

$$Vl_b = Vl_{bat} N_T. \tag{3.7}$$

3.2.3 Total Battery Bank Power Losses

The power losses dissipated in the battery bank (PL_b) due to the internal battery resistance affect the efficiency of the storage system. The total power losses of the storage system calculated in this work is presented by:

$$PL_b = \left(\frac{r_{bat} N_s}{N_p}\right) (C_n C_r)^2, \tag{3.8}$$

where r_{bat} is the internal resistance of a single battery. This equation is based on the equivalent resistance of the battery bank. Thus, the number of batteries connected in series and parallel are taken into account.

3.2.4 Stored Capacity Index

Depending on the N_T selected, different energy capacities can be observed for each battery association. In addition, the capacity of storage energy directly affects the autonomy time of the system. Therefore, this criterion needs to be taken into account during battery selection. The energy capacity index is defined by the ratio between the

energy stored by the battery bank (En_{Stored}) and the total energy produced by the system ($En_{Generated}$). In this work, it was considered the stored capacity index (In_{Cap}) presented by:

$$In_{Cap} = \frac{En_{Stored}}{En_{Generated}}. \tag{3.9}$$

3.2.5 Total Battery Bank Cost

The cost of the battery bank (c_b) may make the project unfeasible. In this work, the total cost is calculated by the multiplication of N_T by the price of a single battery (c_{bat}) (obtained through the manufacturer's catalog):

$$c_b = N_T.c_{bat}. \tag{3.10}$$

3.2.6 Battery Lifetime

In general applications, the battery lifetime (LF) is shorter than that of other components, such as capacitor and semiconductor power devices (Stroe et al., 2014). The replacement of the battery bank affects the cost and payback of the entire system. Therefore, strategies to evaluate the lifetime of each battery technology is necessary. Two important issues related to the battery lifetime are presented:

- The association of batteries in series and parallel affects the lifetime of the battery due to the voltage and current levels to which the battery is submitted (Stroel Ioan, 2014);
- The lifetime methodology depends on the battery technology. Thus, in this work the methodologies for lead-acid and Li-ion batteries proposed by Schiffer et al. (2007) and Stroel Ioan (2014) respectively, are used. The lifetime methodology for lead-acid and Li-ion are presented in Chapter 2.

3.3 Multiple Criteria Decision Making

Based on the criteria considered in the last section, it necessary to choose a method to select the best battery for the BESS application. Thus, the MCDM is adopted (Farahani; SteadieSeifi; Asgari, 2010). Some methods, such as TOPSIS, is common used in the selection process in the MCDM techniques. This method is able to select and order the input parameters based on the weights chosen by the user. In this work, the TOPSIS method, proposed by (Hshiung; Dieckerhoff; Huang, 1981) is used, as shown in Fig. 19.

This method assumes that if each attribute takes a monotonically increasing or decreasing variation, then it is easy to define an ideal solution. Thus, a solution is composed

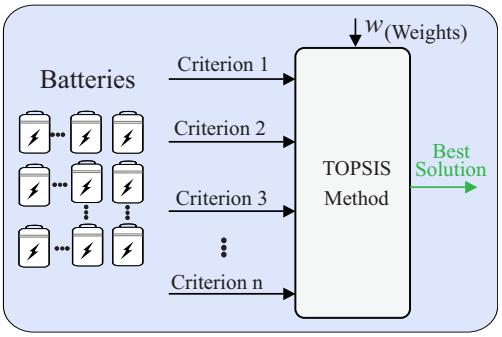

Figure 19 – TOPSIS method used to select the best battery based on the selected criteria.

Source: Own authorship.

of all the best attribute values achievable, while the worst solution is composed of all the worst attribute values achievable. Therefore, TOPSIS finds a solution which has the shortest distance from the ideal solution in the Euclidean space. Basically, the TOPSIS algorithm is systematically described by the following steps:

1) The decision matrix construction (D): D is the attribute matrix given to each criterion for all the battery models. Thus, the decision matrix presents the dimension m x n, where m is the number of battery in the study and n is the number of criterion adopted. The nomenclature used for the elements of D, which is the attribute given for each criterion of each battery model, is d_{ij} (where i = 1,2...m and j = 1,2...n). The decision matrix is represented as:

$$D = \begin{bmatrix} d_{11} & d_{12} & ... & d_{1n} \\ d_{21} & d_{22} & ... & d_{2n} \\ ... & ... & ... & ... \\ d_{m1} & d_{m2} & ... & d_{mn} \end{bmatrix} \tag{3.11}$$

2) The normalized decision matrix construction (D_N): Based on the the D matrix, the normalized matrix decision is performed considering the Euclidean normalization:

$$D_N = \begin{bmatrix} d_{N11} & d_{N12} & ... & d_{N1n} \\ d_{N21} & d_{N22} & ... & d_{N2n} \\ ... & ... & ... & ... \\ d_{Nm1} & d_{Nm2} & ... & d_{Nmn} \end{bmatrix} \tag{3.12}$$

Each element of the normalized decision matrix is represented as d_Nij:

$$d_{Nij} = \frac{d_{ij}}{\sqrt{\sum_{i=1}^{m} d_{ij}^2}}, \tag{3.13}$$

where parameter i = 1,2,...m and j = 1,2,...n.

3) The normalized weighted matrix construction (D'_N): In this step, the weight (w_j) giving for each parameter is taking into account. The D'_N is calculated as:

$$D'_{Nij} = w_j.d_{Nij}, \tag{3.14}$$

where parameter i = 1,2,...m and j = 1,2,...n. In addition, it is important to note that $\sum_{j=1}^{n} w_j = 1$.

4) Ideal and anti-ideal solution determination: In this step is necessary to calculate the ideal solution (A^+), which is represented as $[V_1{}^+, V_2{}^+ ... V_n{}^+]$. The elements for the ideal solution (V_j^+) can be calculated as:

$$V_j{}^+ = \max(D'_{Nij}), \tag{3.15}$$

where i = 1,2,...m.

On the hand, the anti-ideal solution (A^-) is represented by $[V_1{}^-, V_2{}^- ... V_n{}^-]$. The elements for the ideal solution (V_j^-) can be calculated as:

$$V_j{}^- = \min(D'_{Nij}), \tag{3.16}$$

where i = 1,2,...m. In this step is important to note that Eq.(3.15) and Eq.(3.16) are valid when the increasing of battery criterion value is desirable (for example the battery lifetime). On the other hand, when the criterion is undesired (for example price and volume), the terms max and min from Eq.(3.15) and Eq.(3.16) must be inverted.

5) Ideal and anti-ideal solution separation: In this step is necessary to calculate the Euclidean distance from the ideal ($S_i{}^+$) ans anti ideal ($S_i{}^-$) solution, as presented in Eq.(3.17) and Eq.(3.18):

$$S_i{}^+ = \sqrt{\left(\sum_{j=1}^{n} (V_j{}^+ - D'_{Nij})^2\right)}, \tag{3.17}$$

where i = 1,2,...m.

$$S_i{}^- = \sqrt{\left(\sum_{i=1}^{n} (V_j{}^- - D'_{Nij})^2\right)}, \tag{3.18}$$

where j = 1,2,...n.

6) The battery model ranking: In this step the batteries model are allocated in order according to the scores (C_i) given by the equation Eq.(3.19). The ranking is performed based on the decreasing order of C_i.

$$C_i = \sqrt{\frac{S_i^-}{S_i^- + S_i^+}}, \tag{3.19}$$

where i = 1,2,...,m.

As observed in Fig. 19, it is necessary to define the weights of the battery criteria in the TOPSIS method. Thus, in this work, the AHP is used. This method is a powerful multicriteria decision-making tool that has been used in numerous applications in various fields of economics, politics and engineering (Chai; Liu; Ngai, 2013). With the AHP method, the user can give his opinion in the criterion importance level. Thus, the battery can be chosen based on the characteristic desired by the user. The steps of the AHP are presented are following presented.

1) The relative importance of different criteria with respect to the goal: In this step, a pair-wise comparison matrix is created. Basically, this matrix confronts all the criteria based on the a scale of relative importance (x_{ij}), which is presented in Table 1. As observed, the importance level of a criterion in relation to the others is varied from 1 (equal important) to 9 (absolute more important).

Table 1 – Scale of relative importance of the selected criteria.

Numeric Scale x_{ij}	**Conceptual Scale**
1	Equal
3	Moderate
5	Strong
7	Very Strong
9	Absolute
2,4,6,8	Intermediate values

In Table 2 is presented the pair-wise comparison matrix. As observed, each criterion a_i ($i = 1, 2..m$) is confronted to each other criterion and the relative scale x_{ij} is used. The line criterion of the matrix is always compared to the row criterion. In addition, when the same criterion is compared, the value 1 is used, since they are equal important to the selection process.

Table 2 – The pair-wise comparison matrix.

	a_1	a_2	...	a_n
a_1	1	x_{12}	...	x_{1n}
a_2	$1/x_{12}$	1	...	x_{2n}
...	...	...	...	...
a_m	$1/x_{m1}$	$1/x_{m2}$	...	1

2) The pair-wise matrix normalization: In this step the pair-wise matrix is normalized. Each element is normalized using the sum of the elements of the respective row.

3) The weights calculation: Finally, in this step the weights for the criteria are estimated. Thus, the weight for each criteria is calculated based on the average of the line elements.

Thus, the TOPSIS and AHP methods are the techniques from the MCDM which are used to select the battery. Before apply the AHP and TOPSIS methods, the criteria are separated into two groups based on the CAPEX and OPEX concepts. The idea is separate the criteria related to the operation of the BESS (V_{dc}, PL_b, Ind_{Cap} and LF) and the initial capital spend to the project (Vl_b and p_b). Thus, only the parameters of battery cost and volume are considered CAPEX while the other parameters are considered OPEX, as presented in Fig. 20. In addition, it is important to note the color separation in Fig. 20. The increasing of the red criteria refers to a negative parameter in the battery selection model. On the other hand, the increasing of the green criteria are a positive parameter for the battery selection model. As example, the battery with higher power losses is not a good criterion for the battery selection. However, the battery with a higher lifetime is interesting for the selection process.

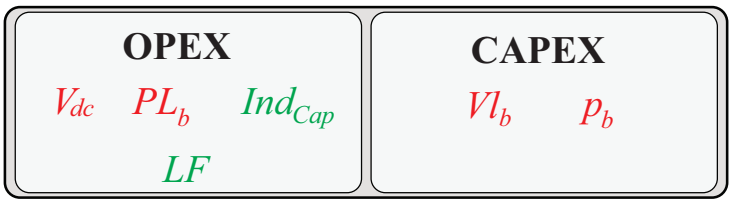

Figure 20 – Criteria separation into OPEX and CAPEX group.

Source: Own authorship.

The division of these groups is performed to estimate the criteria weights. Thus, the user can give relative importance to the CAPEX or OPEX group. In order to have a more generic results, the AHP methods was performed varying all the possible combination to the relative importance. Thus, the x_{ij} can have two values: $x_{ij_{CAPEX}}$ and $x_{ij_{OPEX}}$. Each of them are varied from 1 to 9 and all the combinations are considered in the generic solution. Therefore, the best solution matrix based on the relative weights of OPEX and CAPEX are represented in Fig. 21. Thus, the user can choose the best battery solution based on the relative importance of OPEX and CAPEX group.

Since the weights are estimated, the TOPSIS is used to order the best battery to the application. In order to have a better understand of the proposed battery selection methodology, Fig. 22 is presented. As observed, the first step is to perform the battery bank sizing. Thus, the parameters from the project (energy and power requirements) and information from the battery manufacturer datasheet are taken into account. Thus, the six criteria are estimated according to the methodology presented in this chapter. Finally, the criteria are applied to the TOPSIS method. The AHP method is also used to vary the

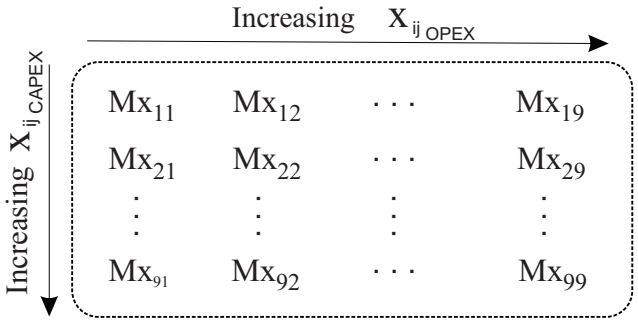

Figure 21 – Optimum matrix of the battery solution.

Source: Own authorship.

OPEX and CAPEX relative importance. Thus, the optimum matrix is generated.

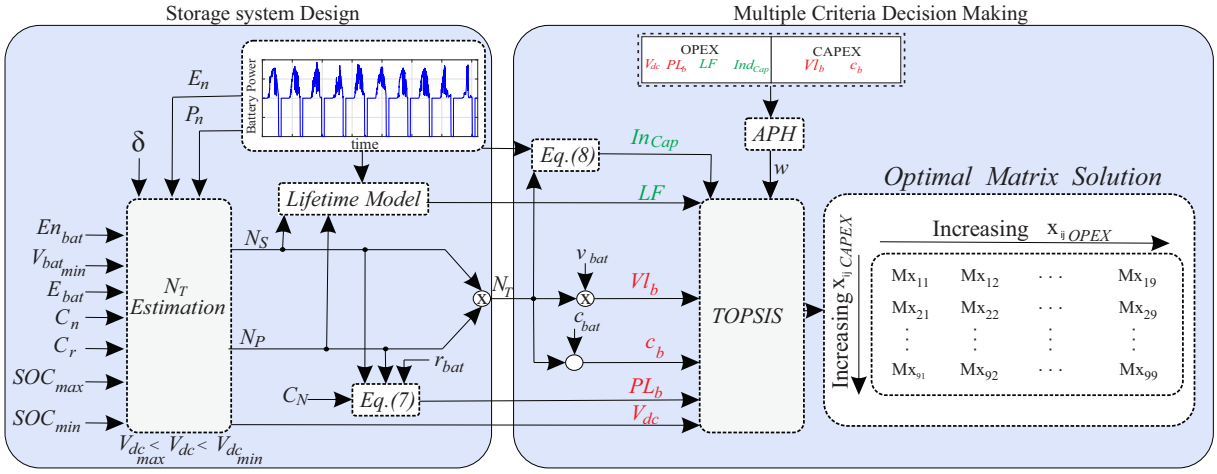

Figure 22 – Proposed methodology assisted by choice matrix approach.

Source: Own authorship.

It is important to make sure that the proposed methodology is adaptable for different application of the BESS. It is only necessary to select the input parameters of the storage system design (E_n and P_n). In addition, more (or less) criteria can be added to the methodology. In addition, different weights can be chosen for the methodology. It is possible to give different weights for each criteria inside the CAPEX and OPEX groups.

3.4 Application of the Proposed Methodology

The proposed methodology is applied to choose the battery bank for a BESS in a PV system application based on the peak shaving operation. This system is composed by a three-phase inverter, which is responsible to inject the active power from the PV modules to the grid, and by a bidirectional dc/dc converter, responsible to suport the charge and discharge process of the battery bank.

The Federal University of Viçosa was considered the installation where the proposed methodology is applied. The University is connected to the medium voltage (13.8 KV) and it is classified as Group A, according to ANEEL (ANEEL, 2022). The demand of electrical power consumed by the University over one year (P_L) was measured and it is presented in Fig. 23. As observed, during the peak time, from 17:00 to 20:00 PM, the power consumed is important, which increases the cost spent to the electrical energy consumption. To reduce the cost with the electrical energy, a solution is the installation of a photovoltaic system connected to a BESS. Thus, the energy produced by the PV modules during the day is stored and used to supply the loads during the peak time.

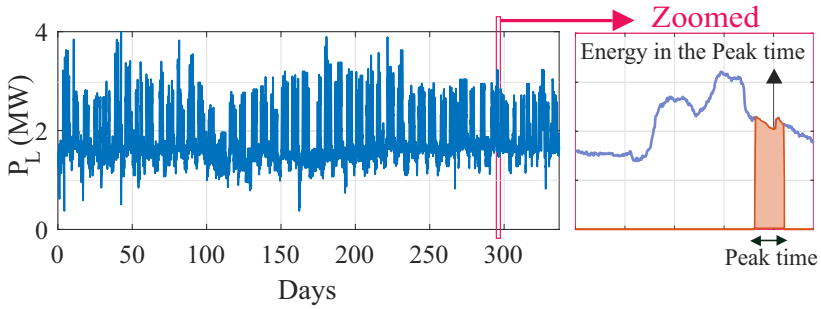

Figure 23 – Load mission profile over one year with sample time equal to 5 min.

Source: Own authorship.

The energy consumed by the load during the peak hours for all the days over one year is calculated and the highest value is used to size the PV system. The value of 7.5 MWh was obtained as the maximum energy consumed by the load. Considering the peak time of three hours, the nominal active power for the PV inverter should be equal to 2.5 MW. Thus, a commercial solution is used in this work. Five PV inverters of 500 kW, manufactured by WEG, are adopted (WEG, 2021). Thus, based on that information and the mission profile of solar irradiance (G) and ambient temperature (T_a) of Goiânia, in Goiás (Brasil), it is possible size the PV system used. These data from other state of Brazil was used since it was the data based available with a reduced sample time. The mission profile of G and T_a are presented in Fig. 24 (a) and (b). The maximum power generated by the PV system was set at 500 kW (which is the nominal power of the PV inverter). Thus, the mission profile of the BESS reference power can be performed based on the PV generation and the energy consumed by the load during the peak hour. The mission profiles of solar irradiance, ambient temperature and the BESS reference power are presented in Fig. 24 (c). It is important to say that this mission profile is the possible reference of the battery bank. The SOC of the battery is analyzed in order to grantee the safety of the battery bank.

The reference mission profile for a typical week is presented in Fig. 25. As observed, the BESS is charged with the energy generated by the PV system and supplies the load

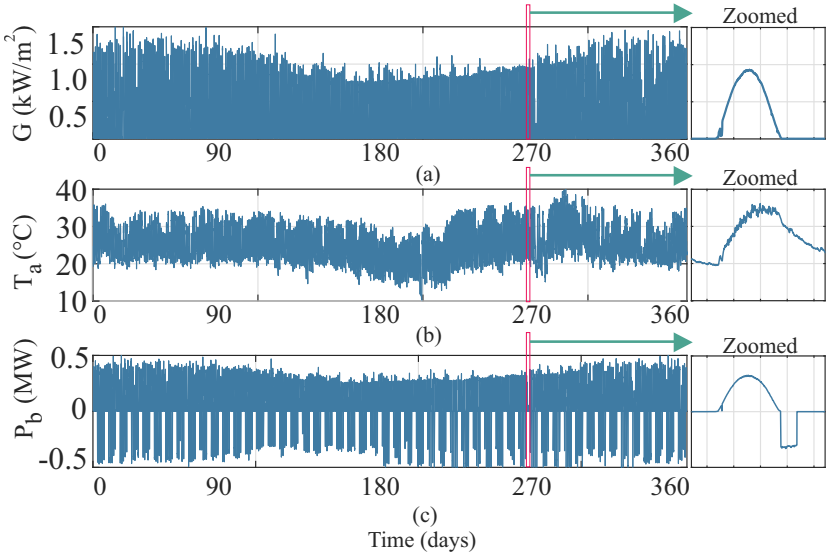

Figure 24 – One year mission profile of the battery bank power (a) solar irradiance, (b) ambient temperature and (c) battery bank power mission profile.

Source: Own authorship.

during the peak hours. In addition, the discharging process is not considered during the weekend, since the price of electrical energy is generally the same over the day.

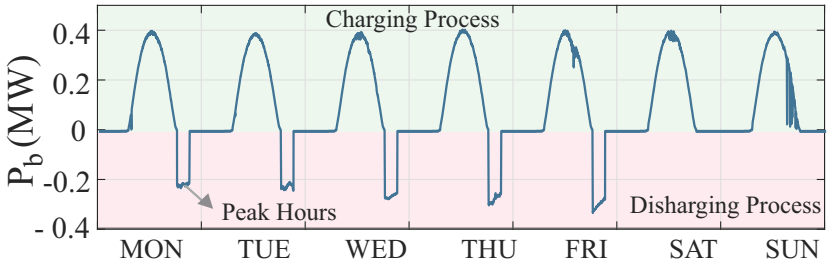

Figure 25 – Representation of the BESS peak shaving operation over one week.

Source: Own authorship.

Regarding to the batteries that can be used in the project, 27 batteries (called M =1, 2 ...27) are selected. In this context, 13 lead acid batteries manufactured by MOURA are considered. The batteries are from the clean nano technology (MOURA, 1987). These batteries present nominal capacity from 30 Ah to 220 Ah. In addition, 14 Li-ion batteries manufactured by Power Brick (Power Tech, 2021) and Chargex (Chargex, 2021) are considered. The batteries were numbered from 1 to 27, and their main parameters are summarized in Table 3. The lead-acid batteries correspond to the model 1 to 13, the Li-ion batteries from Power Brick correspond to the models 14 to 20 and the batteries manufactured by Chargex correspond to the models 21 to 27. The SOC interval for all the batteries models was considered from 20% to 100%, and the battery temperature was considered constant and equal to 30°C.

Table 3 – Batteries and its main parameters.

M	C_N (Ah)	E_{bat} (Wh)	Vl_{bat} (m^3)	r_{bat} ($m\Omega$)	c_{bat} (pu)	V_{batmin} (V)
	Lead acid batteries - MOURA					
1	30	215	0.005	8.7	1.00	10.0
2	36	218	0.006	7.1	1.16	10.0
3	45	308	0.006	6.9	1.25	10.0
4	45	308	0.007	6.9	1.25	10.0
5	55	341	0.007	6.2	1.55	10.0
6	63	465	0.009	5.0	1.71	10.0
7	80	484	0.012	4.9	2.52	10.0
8	100	605	0.012	5.2	5.14	10.0
9	105	624	0.014	4.9	2.75	10.0
10	150	880	0.026	3.1	3.77	10.0
11	170	1029	0.022	3.3	8.85	10.0
12	175	1059	0.035	2.5	3.88	10.0
13	220	1207	0.035	2.5	4.52	10.0
	Li-on batteries - Power Brick					
14	20	260	0.002	5.0	5.74	10.5
15	30	380	0.002	3.3	8.07	10.5
16	40	510	0.005	2.5	10.27	10.5
17	45	580	0.005	2.2	12.00	10.5
18	70	900	0.007	1.4	14.82	10.5
19	100	1280	0.009	1.0	22.89	10.5
20	250	3200	0.027	0.4	48.60	10.5
	Li-on batteries - Chargex					
21	20	240	0.002	5.0	4.02	10.5
22	35	420	0.003	2.9	7.26	10.5
23	40	480	0.005	2.5	8.07	10.5
24	50	600	0.005	2.0	9.69	10.5
25	75	900	0.011	1.3	15.35	10.5
26	80	960	0.012	1.2	16.16	10.5
27	100	1280	0.014	1.0	20.21	10.5

The first step is to determine the total number of batteries necessary, considering the energy and power requirements. Fig. 26(a) shows the number of batteries in series and parallel, and Fig. 26(b) shows the total number of batteries for each battery type. As observed, for all the three manufactures, the N_T decreases with the C_N increasing, since a higher level of energy stored is expected for batteries with higher nominal capacity (in Ah).

Including N_T, the six criteria considered in this work are estimated and shown in Table. 4. As observed, V_{dc} can present different values for each battery type. The lowest and highest V_{dc} values are 1126.0 V and 1170.8 V, respectively. This fact is explained based on the N_T estimation process, since the chosen dc-link voltage is related to the lowest number of batteries. In addition, the PL_b and vol_b values are higher for the lead

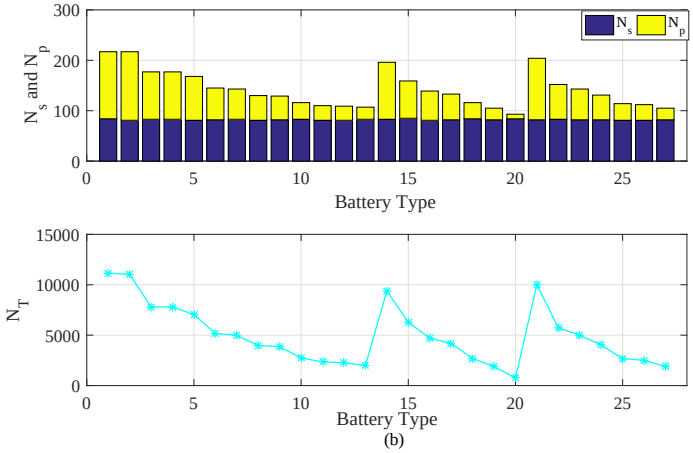

Figure 26 – Battery design estimations: (a) number of batteries in series and in parallel and (b) total number of batteries.

Source: Own authorship.

acid batteries, when compared to the Li-on batteries. On the other hand, the LF is higher for the Li-on batteries. These results are explained based on the characteristics of the battery technologies.

As observed, the In_{Cap} can present different values for each battery type. The highest In_{Cap} value is obtained for the M19. This results can be explained based on the storage energy capacity of the battery bank, which is related to the total number of battery and the energy storage capacity of each the battery type. In addition, the price for the Li-ion batteries are higher than the lead-acid batteries. The price of the battery bank was normalized based on the lowest price value, which is from battery number 6.

Initially, the proposed methodology is applied only to the lead-acid battery. Thus, the optimum matrix solution is presented in Fig. 27. As observed, if the relative importance is given to OPEX, the M7 is the optimal solution. On the other hand, if the relative importance is given to the CAPEX, the M6 is presented as the best solution. In addition, when the relative importance between the OPEX and CAPEX are closely, the M5 is considered the best solution. In terms of percentage as the best solution in the optimal matrix, the M7 appears 62.96 %, M6 appears 17.75 % and M7 appears 17.28 %.

Similar analysis is performed for the Li-on batteries, and the optimal matrix solution is shown in Fig 28. If the relative importance is given to OPEX, the M19 is considered the best option. On the other hand, when more relative importance is given to the CAPEX, M20 is considered the best battery choice. In terms of percentage as the best solution in the optimal matrix, the M19 appears and M20 appear 62.96 % and 37.04 %, respectively.

Finally, the methodology proposed was applied to the 27 batteries and the

Table 4 – Battery Models and the main parameters.

M	V_{dc} (V)	Vl_b (m^3)	PL_b (kW)	LF (Years)	c_b (pu)	In_{Cap} (%)
	Lead acid batteries - MOURA					
1	1156,8	52.6	32.9	7.06	1.26	44.72
2	1126,0	71.5	33.8	7.47	1.45	44.71
3	1143,8	50.7	41.6	7,05	1.11	44.74
4	1143,8	55.0	41.6	7.05	1.11	44.74
5	1126,0	52.2	49.6	7.20	1.24	44.74
6	1129,8	44.6	41.7	6.73	1.00	44.72
7	1143,8	59.5	50.7	7.06	1.42	44.87
8	1126,0	46.3	71.2	7.00	2.33	44.70
9	1129,8	53.4	71.2	7.00	1.20	44.77
10	1143,0	72.4	53.1	6.88	1.14	44.87
11	1126,8	51.9	76.4	6.83	2.36	45.00
12	1126.8	78.4	61.5	6.84	1.02	44.72
13	1143,8	68.9	85.4	6.95	1.12	44.76
	Li-on batteries - Power Brick					
14	1143,8	21.5	18.8	13.41	4.59	44.66
15	1170,8	14.5	18.9	13.50	4.82	44.82
16	1126.8	21.3	18.8	13.50	4.35	44.74
17	1129.0	19.3	18.9	13.50	4.82	44.81
18	1156.8	17.7	18.6	13.50	4.35	44.80
19	1129.0	17.5	18.8	13.58	4.76	44.90
20	1156.8	20.4	18.9	13.58	3.41	45.00
	Li-on batteries - Chargex					
21	1129.0	21.8	20.0	13.50	4.24	44.66
22	1143.8	16.4	20.2	13.50	4.60	44.74
23	1129.0	26.9	20.0	13.50	4.59	44.66
24	1129.8	21.7	20.1	13.58	4.73	44.84
25	1126.3	29.3	19.9	13.58	4.66	44.74
26	1126.3	30.6	20.0	13.58	4.61	44.83
27	1129.3	26.2	18.9	13.58	4.33	44.90

matrix solution is presented in Fig. 29. As observed, when the CAPEX relative index increases, the M6 is considered the best solution. On the other hand, when OPEX relative index increases, the M19 is considered the best solution. In addition, when the relative importance between the OPEX and CAPEX are closely, the M20 is considered the best solution. In addition, for all the combinations of $x_{ij_{CAPEX}}$ and $x_{ij_{OPEX}}$, the M6, M19 and M20 appears 18.75%, 30.86% and 43.20% of times the best solution, respectively.

3.5 Chapter Conclusions

This paper proposes a methodology for the selection of the best battery solution based on the CAPEX and OPEX matrix. This proposed methodology was applied to

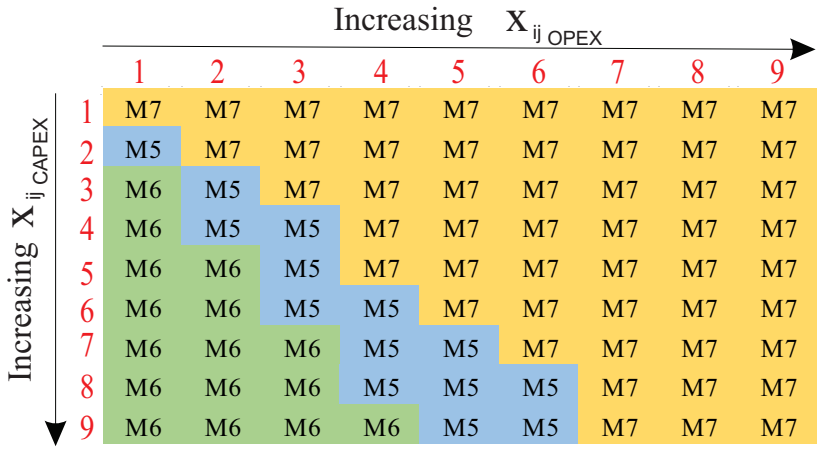

Figure 27 – Optimum matrix solution for the lead-acid battery models (form M1 to M13).

Source: Own authorship.

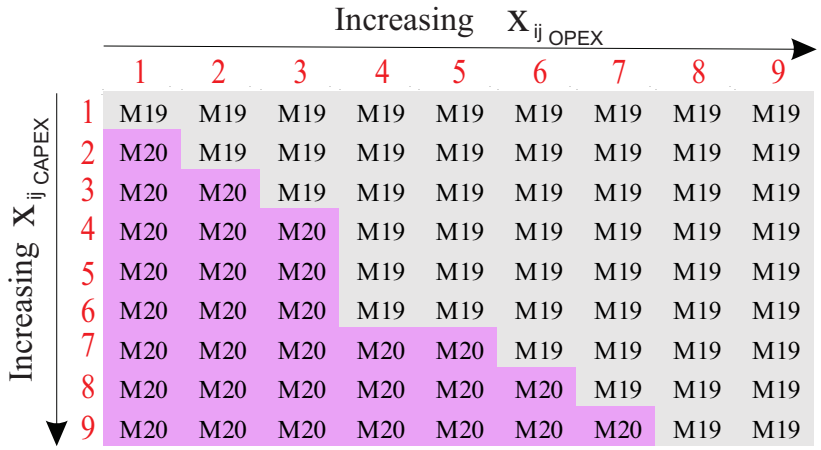

Figure 28 – Optimum matrix solution for the Li-ion battery models (form 14 to 27).

Source: Own authorship.

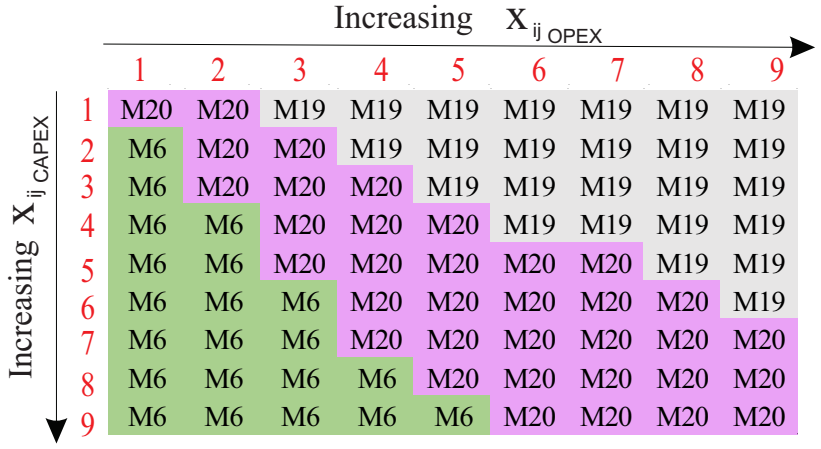

Figure 29 – Optimum matrix solution for lead-acid and Li-ion batteries(form 1 to 27).

Source: Own authorship.

27 batteries. The parameters of the dc-link voltage, battery bank voltage, power losses, price, lifetime and energy storage capacity were taken into account. These parameters were separated in OPEX and CAPEX groups, and the best solution based on the relative importance of those two groups were analyzed.

In addition, the lead-acid battery model manufactured by MOURA was selected when the CAPEX presented high importance level compared to the OPEX. On the other hand, the Li-ion battery manufactured by Power Brick was selected as the best solution. In addition, the Li-on battery model was selected as the optimum solution in 74.04% of the possible combinations between $x_{ij_{CAPEX}}$ and $x_{ij_{OPEX}}$. Finally, the proposed battery selection method is a generic methodology which can compare batteries using different technology and from different manufactures. In addition, the user can add or remove criterion in the battery selection process. In the next chapter, the lifetime evaluation o the dc/ac of the BESS is performed.

4 Lifetime Evaluation of the BESS dc-ac Stage During HCC Operation

The BESS is generally used in renewable energy applications to support the intermittent behavior of wind and PV systems during the energy generation process. In this context, the peak shaving operation is considered an important BESS application. In addition, the BESS can also be used to perform ancillary services to improve the grid power quality. However, the extra functionality can affect the reliability of the entire system. Depending on the grid distortion level and environmental conditions, the BESS is submitted to different stresses, which directly affect its lifetime consumption. In this chapter, the lifetime evaluation considering the semiconductor devices and the dc-link capacitors of the BESS dc/ac stage during HCC operation is performed.

4.1 BESS Parameters

A representation of the BESS used for such applications and ancillary services are presented in Fig. 30.

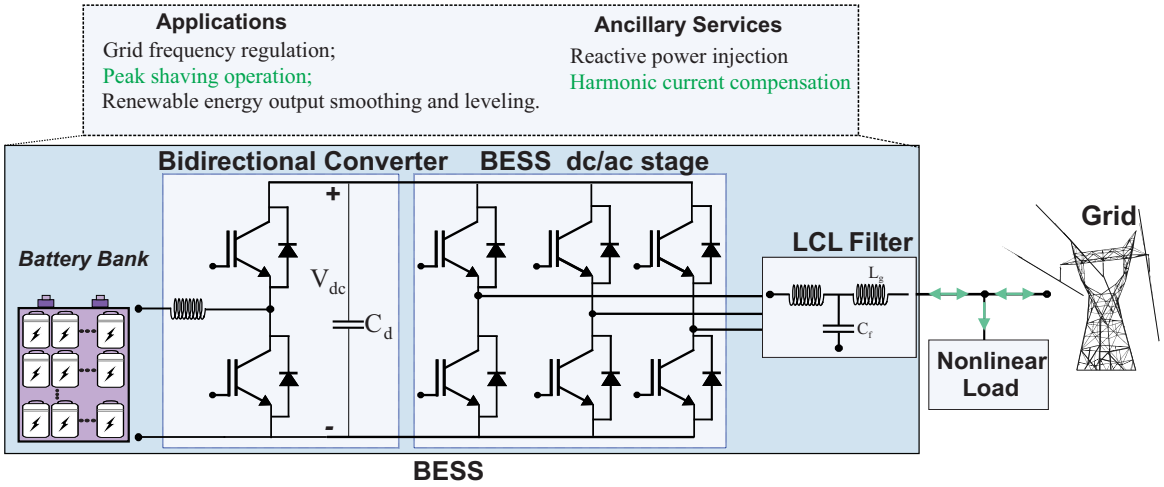

Figure 30 – Structure of a BESS used to perform the common applications and also ancillary services.

Source: Own authorship.

This combination is an interesting solution since it is observed a better usage of the BESS to improve the grid power quality. However, the extra functionality due to the ancillary services can reduce the reliability of the entire system, since additional stresses can be added to the BESS components. Therefore, it is necessary to study how much the

extra functionality can affect the reliability of the BESS components. In this work, the BESS working as peak shaving operation and HCC as ancillary service is analyzed.

The BESS used in this work is a 500 kW three-phase dc/ac stage. The main electrical parameters of the BESS are described in Table 5. As observed, the used power semiconductor devices is an IGBT module 1700V/600A (with antiparallel diode) manufactured by Infineon, with part number FF600R17KE3. The dc-link capacitor used is the 1200μF/500V, part number B43512A6128M0, manufactured by TDK. The capacitor bank is composed of twenty strings (composed of two capacitors in series) connected in parallel.

Regarding the battery selected to the project, the M19 was selected (based on the Chapter 3) as the battery used in this work. In this case, the OPEX relative importance was considered the with the most relative importance. The M19 is Li-ion battery manufactured by Chargex. The main parameters of the battery bank are presented in Table 5. The battery bank are composed of 23 strings connected in parallel (each string is composed of 82 battery in series).

Table 5 – Main parameter of the BESS

Parameter	Value
Nominal Power	500 kW
Grid Voltage	680 V
Dc link Voltage (V_{dc})	1200 V
Full-bridge switching frequency	12 kHz
Sampling Frequency	12 kHz
Filter Inductor - L_f	5.8 mH
Filter Inductor - L_g	5.8 mH
Filter Capacitor - C_f	25 μF
Grid nominal Frequency - f_n	60 Hz
Dc-link capacitance - C_d	15 mF
Nominal battery capacity - C_n	100 Ah
Battery Energy - E_{bat}	1280 Wh
Battery volume - Vl_{bat}	0.009 m^3
Internal battery resistance - r_{bat}	1 $m\ \Omega$
Maximum battery voltage - V_{batmax}	10.5 V
Minimum battery voltage - V_{batmin}	13.5 V

The lifetime evaluation for the battery bank and BESS inverter components (such as semiconductors devices and dc-link capacitors) are presented in this Chapter. Special attention is considered to the semiconductor devices of the BESS dc/ac stage, since the lifetime evaluation for those components considering the HCC operation is not yet consolidated in the literature. Thus, two cases studies are considered in this chapter:

- Case Study 1: BESS with peak shaving considering constant harmonic current compensation;

- Case Study 2: BESS with peak shaving and harmonic current compensation based on mission profile operation.

The Case Study 1 presents the effect of the HCC operation in the semiconductors devices (IGBT and Diodes). Thus, constant operation points for the system are considered. For the Case Study 2, the lifetime evaluation of the semiconductor devices and the dc-link capacitors based on real mission profile are considered. Thus, the annual lifetime consumption and Monte Carlo analysis are discussed.

4.2 Case Study 1: Constant Harmonic Current Compensation

Before understand the effect of the HCC process in the inverter lifetime, it is important to understand how the BESS output current is synthesized. Considering the compensation of the harmonic component (h) with the highest amplitude (I_h), the BESS output current for phase a ($i_{sa}(t)$) can be presented as:

$$i_{sa}(t) = I_f \cos(\omega_f t) + I_h \cos(h\omega_f t + \theta_h), \tag{4.1}$$

where I_f is the amplitude of the fundamental component, ω_f is the angular grid frequency and θ_h is the harmonic current phase angle. As observed, the current signal generated by the BESS dc/ac stage depends on the harmonic current parameters (h, I_h, and θ_h). As an example, the current signals of BESS dc/ac stage compensating 5^{th} and 7^{th} harmonic orders with phases angle 0° and 180° are shown in Fig. 31(a) and (b), respectively. As noticed, the output current waveform is dependent on θ_h. Since power losses depend on the current shape, they are affected by h, I_h, and θ_h values. Notably, the current shape becomes more uniform when high-order harmonic components are considered. Consequently, the power losses are less affected by the harmonic phase angle in comparison with low-order harmonic component.

Since the shape of the BESS output current is affected by the HCC operation, the power losses and consequently the junction temperature of the semiconductor devices are also affected. In Fig. 32, the power losses of an IGBT (P_{IGBT}), and the junction temperature of this component (T_{jIGBT}) are presented when the 5^{th} harmonic with phases angle 0° and 180° are compensated. As observed, with the HCC operation mode, the junction temperatures of the semiconductor devices present additional power cycling when compared to the traditional inverter operation.

In this work two thermal cycling stresses are considered: the long cycles due to mission profile variations and the short cycles caused by the fundamental and harmonic

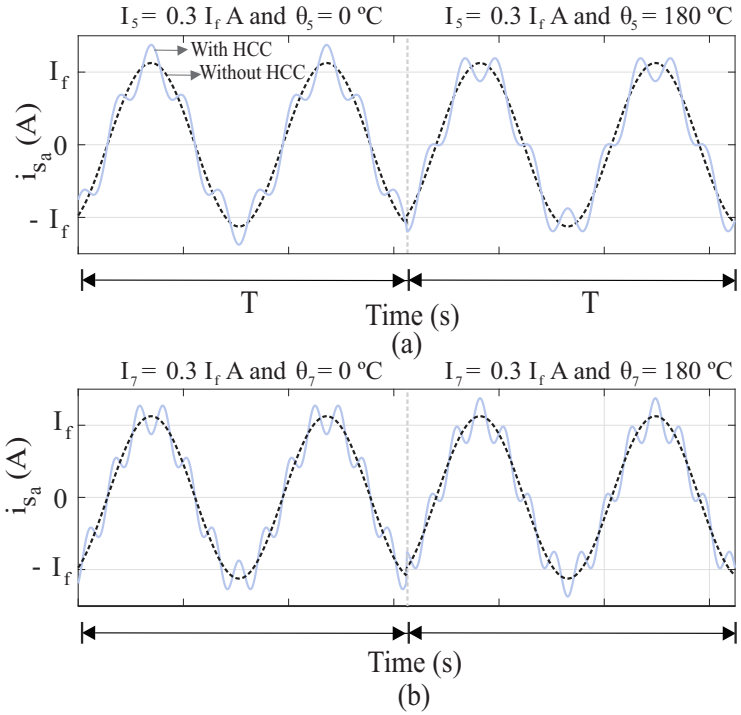

Figure 31 – BESS injecting 200 kW of active power: Output current (phase a) comparison of traditional operation with HCC. In this case, the BESS dc/ac stage is compensating 5^{th} (a) and 7^{th} (b) harmonic current components with phases angle of 0^o and 180^o, respectively.

Source: Own authorship.

frequencies. The lifetime consumption for each of thermal cycling is described in the following subsections.

4.2.1 Lifetime Estimation Considering Long cycle Thermal Loading

Previous works have concluded that the mean junction temperature, the junction temperature fluctuation and the heating time affect the semiconductor lifetime consumption (Ma et al., 2015). With regarding to the HCC operation mode, the semiconductor devices lifetime evaluation considering the long cycles was performed by reference (de Barros et al., 2018). Fig. 33 presents the flowchart to estimate the damage for this time scale.

As observed, the lifetime consumption for long cycles is based on power losses look-up tables. For HCC operation mode, the power losses (P_L) in the semiconductor device depend on the active power injected by the BESS (P_{bb}) and the injected harmonic current. Therefore, in a PLECS simulation environment, the parameters of P_{bb}, I_h, θ_h and T_{jm} are varied to generate the power losses look-up table, as illustrated in Fig. 34. The power losses look-up table can be obtained for an unique harmonic component or for combination of different harmonic orders. The conduction and switching losses of the power devices are stored in the look-up tables.

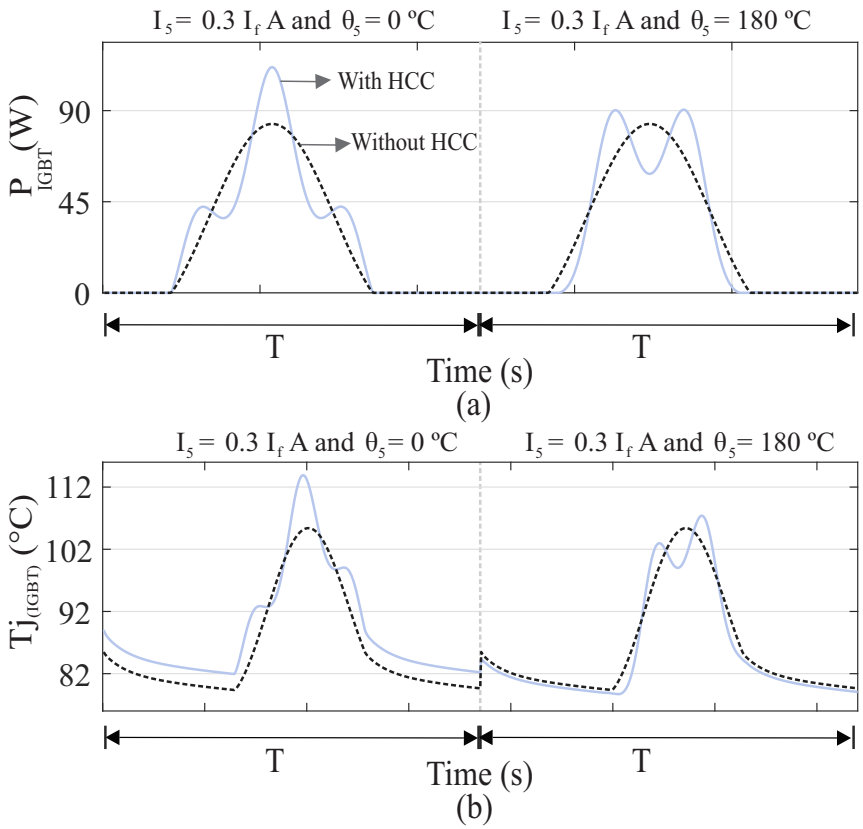

Figure 32 – BESS injecting 200 kW of active power: Power losses (a) and junction temperature of the IGBT (Phase a). In this case, the BESS dc/ac stage is compensating 5^{th} with phases angle equal to 0^o in (a) and 7^{th} harmonic current components with phase angle equal to 180^o in (b).

Source: Own authorship.

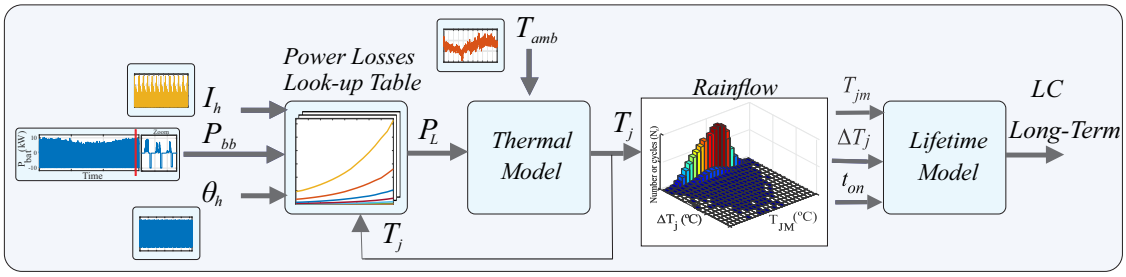

Figure 33 – Flowchart of the long cycle lifetime evaluation considering the HCC operation mode.

Source: Own authorship.

The power losses are estimated based on information provided by the manufacturer's datasheets. For the conduction losses, the on-state characteristics of the diodes and IGBTs are considered. For the switching losses, the energy loss during the turn-on and turn-off switching are used. Temperature dependence of the losses are included in the model as well.

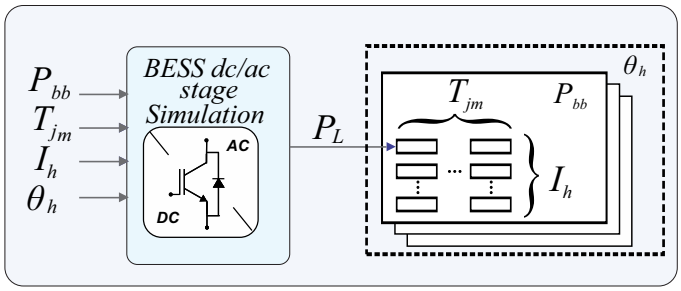

Figure 34 – Power losses look-up table generation process.

Source: Own authorship.

The power losses are applied to an electro-thermal model, which extracts the T_j using the thermal circuit, proposed by (Ma et al., 2015). This approach is composed of the combination of Foster and Cauer thermal impedance models. In this work, the dc/ac stage is composed of three power module of dual IGBTs 1700V/600A manufactured by Infineon, part number FF600R17KE3. The thermal resistances from the semiconductor datasheet are presented in Table 6.

Table 6 – IGBT thermal resistences.

Thermal Resistance	Value (K/W)
Junction to case - IGBT	29.0
Junction to case - Diode	55.0
Junction to Heatsink - IGBT	24.0
Junction to Heatsink - Diode,	56.0

The estimated junction temperature is applied to the rainflow counting algorithm to estimate the parameters of T_{jm}, ΔT_j and t_{on} (Gopi et al., 2015). Thus, these values are used as inputs of statistical lifetime models (Ma et al., 2015). In this work, the lifetime method proposed by Scheuermann, Schmidt and Newman (2014) is used (the method is presented in Chapter 2). This model investigates bondwire fatigue and estimates the number of cycles to failure N_f of the power devices based on the T_{jm}, ΔT_j and t_{on} values. Once the N_f is calculated, the lifetime consumption LC over one year of mission profile is estimated, using the Palmgren-Miner's rule (Huang; Mawby, 2013)

The HCC operation affects the power losses of the semiconductor devices depending on the variation of the harmonic amplitude and phase angle. To illustrate this fact, the behavior of the IGBT and diode power losses due the harmonic phase angle variation are presented in Fig.35 (a) and (b), respectively. For this specific case, the active power inject to the system was set to 500 kW and the harmonic amplitude for the 5^{th} and 7^{th} harmonic component are set to 30 % of the fundamental current. As observed, the harmonic phase angle affects the power losses of the semiconductor devices.

The same analysis was performed considering the harmonic phase angle set at 0^o and variation of the harmonic amplitude was varied from 0 to 30 % of the fundamental

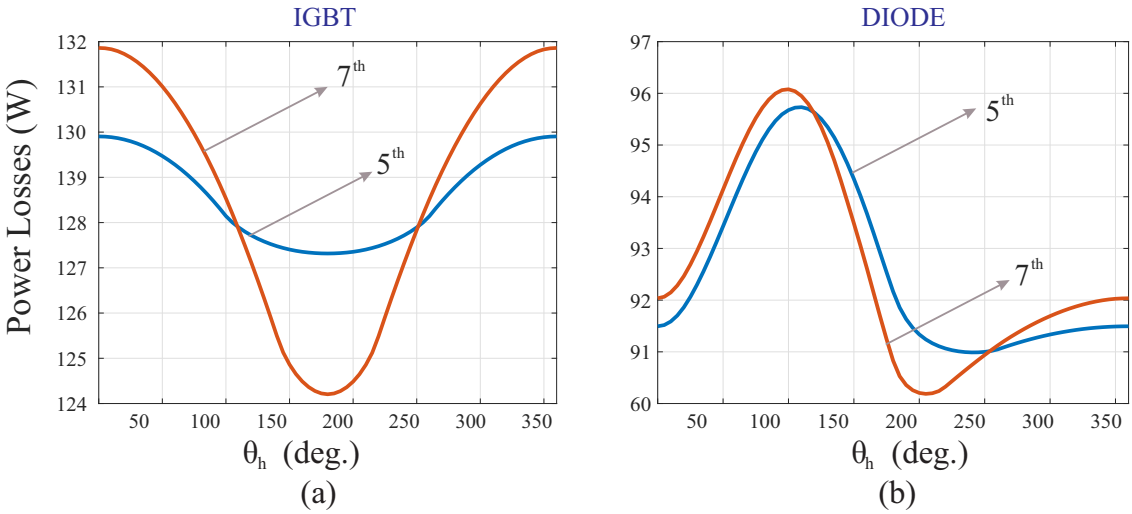

Figure 35 – Variation of the semiconductor power losses due the harmonic phase angle variation: (a) IGBT and (b) diode.

Source: Own authorship.

current, as presented in Fig. 36. The inverter is also injecting 500 kW of active power for this condition. As observed, the power losses increases with the increasing of the harmonic current amplitude. More information about the effect of the harmonic amplitude and phase angle in the semiconductor device can be observed in (de Barros et al., 2018).

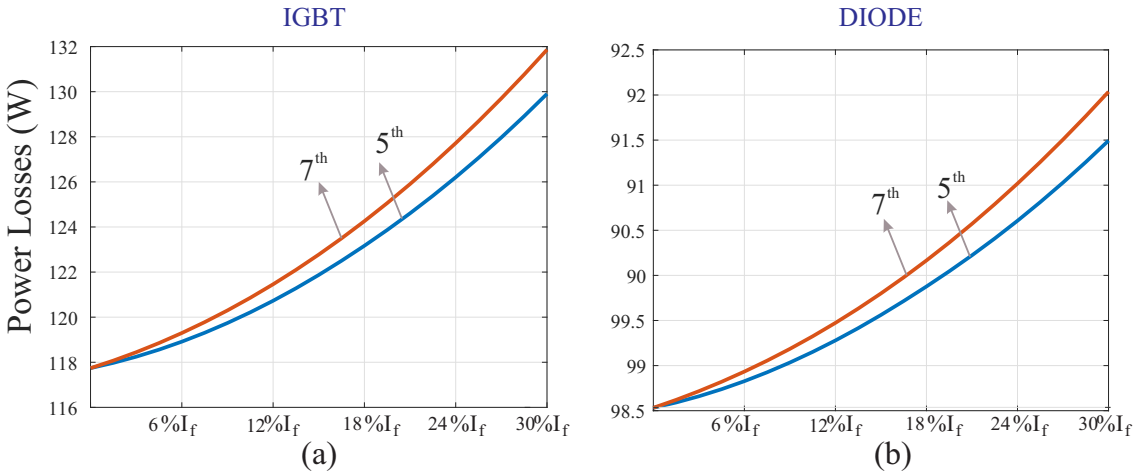

Figure 36 – Variation of the semiconductor power losses due the harmonic amplitude variation: (a) IGBT and (b) diode.

Source: Own authorship.

In Fig. 37, the effect of the compensation of 5^{th} and 7^{th} harmonic components simusltanealy is presented. Thus, the compensation of the 5^{th} and 7^{th} harmonic current components with different phase angles combinations are considered. The active power injected by the BESS is set at 500 kW and the ambient temperature was considered equal to 25 °C.

In Fig. 37(a), the BESS injects 60 % of I_f as the amplitude of the 5^{th} harmonic and

30 % of 7^{th} harmonic. As observed, the IGBT power losses present critical values when the phase angle of the 5^{th} and 7^{th} harmonic components are near to 110^{o} . Similar behavior is observed in Fig. 37(b), where the amplitude of the 5^{th} and 7^{th} harmonic components were considered 30 % and 60 %, respectively. In Fig. 37 (c), the harmonic amplitude for the 5^{th} and 7^{th} harmonic components were both equal to 60 %. These percentage of the harmonic injected are used in order to have a considerable thermal stress in the semiconductor device. In this work, there is any current dynamic saturation used. As observed in this case, the power losses for the IGBT were reduced compared to the previous cases. Thus, it is observed an increasing in the IGBT power losses with the increasing of the harmonic current amplitude. In addition, power losses present critical values for harmonic phase angles near to 110 ^{o} (combination of the 5^{th} and 7^{th} harmonic components).

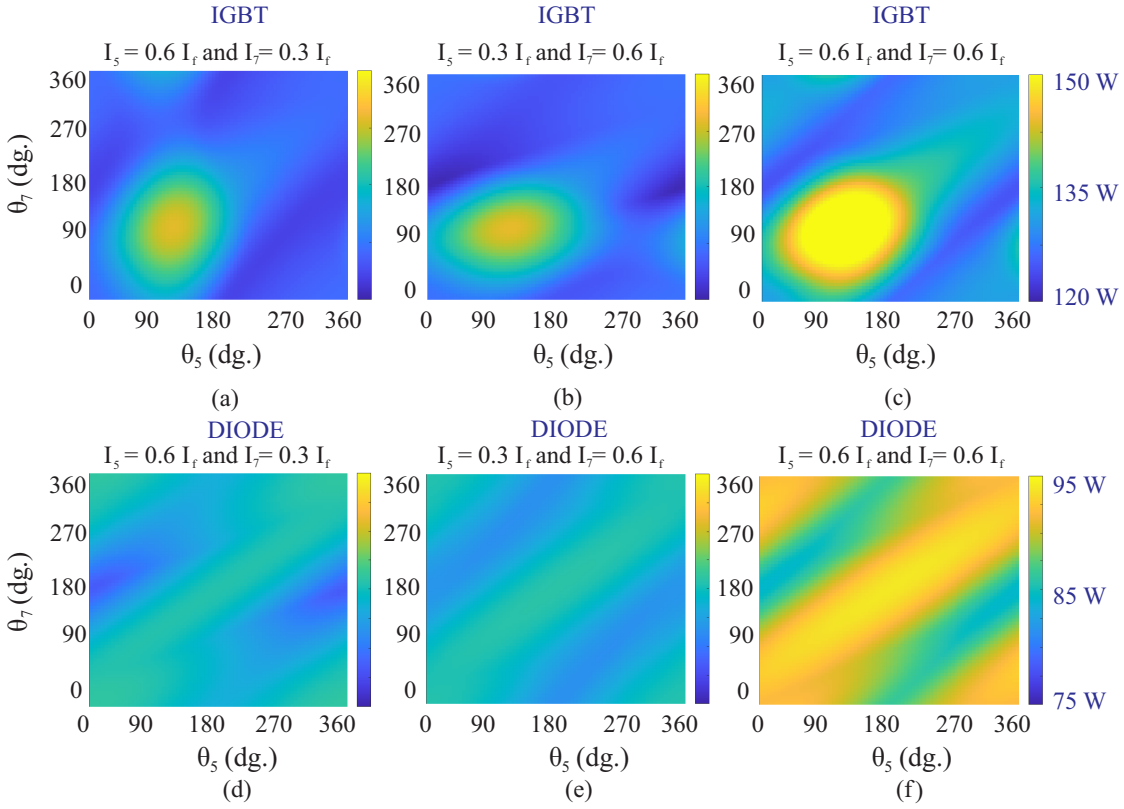

Figure 37 – Power losses of the semiconductor devices when the active power was equal to 500 kW and the ambient temperature equal to 25 ^{o}C. For the IGBT, the 5^{th} and 7^{th} harmonic components were compensated considering: (a) $I_5 = 0.6\ I_f$ and $I_7 = 0.3\ I_f$, (b) $I_5 = 0.3\ I_f$ and $I_7 = 0.6\ I_f$ and (c) $I_5 = 0.6\ I_f$and I_7= 0.6 I_f . For the diodes, the same study were provided: (d) $I_5 = 0.6\ I_f$ and $I_7 = 0.3\ I_f$, (e) $I_5 = 0.3\ I_f$ and $I_7 = 0.6\ I_f$ and (f) $I_5 = 0.6\ I_f$ and I_7 = 0.6 I_f.

Source: Own authorship.

The same study was performed to the diodes and it is presented in Fig. 37(d) - (f). As observed, the power losses also increase with the harmonic amplitude increasing. However, critical values of power losses are presented when the 5^{th} and 7^{th} harmonic

phase angles are near to 0° or 360°. This behavior can be explained based on the thermal impedance of the diodes and the thermal cycles presents in this component. In te next section, the short cycle thermal loading is explained.

4.2.2 Lifetime Estimation Considering Short cycle Thermal Loading

The power cycling due to the line frequency has significant effects on lifetime consumption, when the bondwire failure mechanism is considered (Ma et al., 2015). The short cycle of a single-phase PV inverter during HCC operation was firstly addressed in the literature by de Barros et al. (2021). This work proposes a methodology to estimate the lifetime consumption of the semiconductor devices when different harmonics are synthesized by the dc/ac stage.

The proposed methodology extracts the lifetime parameters (T_j, T_{jm} and t_{on}) directly from one cycle of the junction temperature to ensure that all the power cycling are considered. Therefore, the present study aims to obtain one cycle of junction temperature directly from the system simulation. The flowchart for the proposed methodology is shown in Fig. 38.

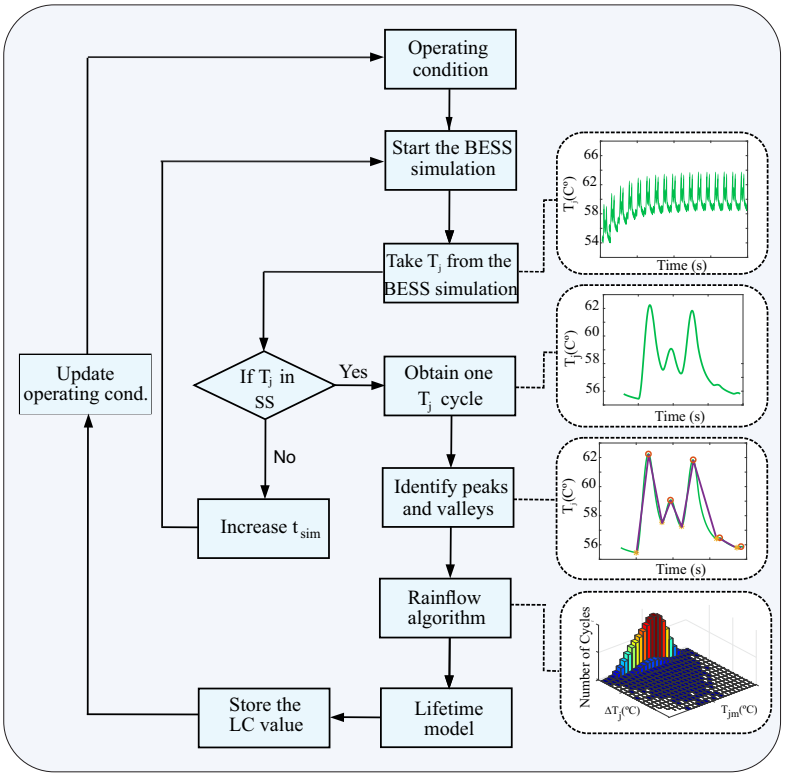

Figure 38 – Flowchat of the proposed short-cycles methodology: the *LC* look-up table generation.

Source: Own authorship.

First of all, in a simulation environment, the system is performed with different combinations of input parameters. For a specific harmonic component, the power required

for the battery bank, the harmonic current amplitude and phase angle are varied. Finally, the junction temperature obtained from the BESS simulation is analyzed for each simulation.

This methodology demands a steady-state (SS) junction temperature value for a better estimation of lifetime consumption. Therefore, T_j is constantly monitored in order to obtain a SS cycle. If the SS is not obtained, the simulation time (t_{sim}) needs to be increased until the steady state condition is achieved. Otherwise, one cycle of the T_j is stored.

The PLECS thermal simulation is used in this work to obtain the junction temperature of the semiconductor device. This software enables the use of the semiconductor devices data provided by the manufacturer datasheets. The conduction losses, switching losses and thermal impedances parameters are used in the software simulation. The effectiveness of the junction temperature estimated by PLECS environment is validated in different works (Ma et al., 2015; Madhusoodhanan et al., 2016; Andresen et al., 2017). In addition, Zhang et al. (2019) shows the effectiveness of T_j estimation by PLECS simulation when the converter sensitizes different frequency values of the output voltage.

The power cycling due to switching frequency is not considered. Previous studies have demonstrated that these cycles have a negligible effect on lifetime consumption, since the values of the fluctuation temperature are very small, compared to the power cycling due to grid frequency (Reigosa et al., 2016a). Therefore, to count only the effects caused by the HCC process, the peaks and valleys of the junction temperature are identified. Then, these information are used to build the SS T_j cycle. This new signal is applied to the rainflow algorithm and the lifetime parameters are obtained.

Thus, all the parameters of ΔT_j, T_{jm} and t_{on} are estimated and applied to the lifetime. The lifetime model is the same used in the long cycle lifetime evaluation. It is important to observe that the resolution of the mission profile for the short cycle lifetime evaluation is hard to obtain, since it is necessary a very low sampling time value (T_s). Therefore, for each interval of T_s, short cycles can be considered constant with the total number of cycles equal to T_sx f_n , as shown in Fig.39.

Then, LC is calculated and stored in a look-up table. As observed, the look-up table is created for a specific harmonic component. The same procedure can be applied for any harmonic characteristics and their combination. The flowchart for the LC, considering the short cycles, is shown in Fig. 40.

Considering a three-phase systems, the common harmonic components are the 5^{th}, 7^{th} and 11^{th} with their combination. Therefore, in this section, the short cycle analysis of the 5^{th}, 7^{th} and the combination of them are analyzed. Only this two harmonic

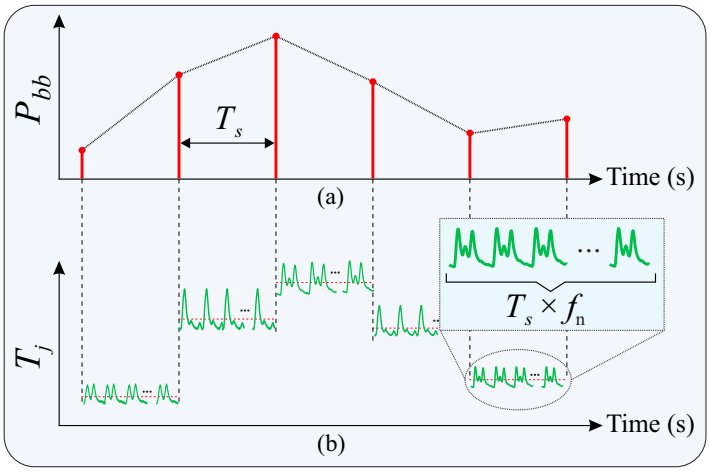

Figure 39 – Exemplification of the total number of short cycles based on the mission profile resolution.

Source: Own authorship.

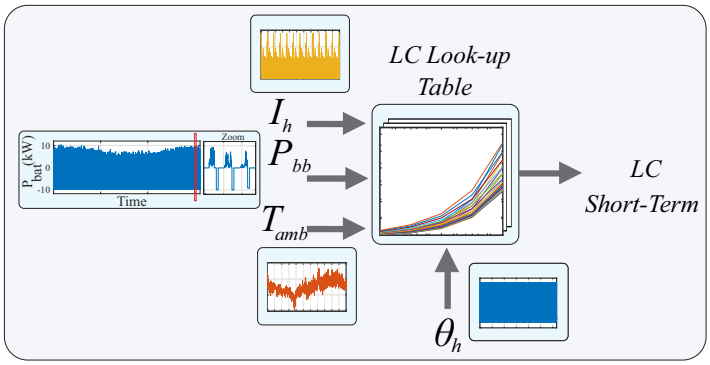

Figure 40 – Flowchart of the LC calculation for the short cycles thermal load.

Source: Own authorship.

components are used since they are more present the electrical power system and because the reduction of the simulation time consumed in the lifetime evaluation process. In this context, the BESS with HCC operation is compared to the BESS without HCC operation to understand how the harmonic compensation can affect the semiconductors devices (IGBT and diodes) lifetime consumption. Since the stress in the power device depends on the I_h/I_{Bat}, two different values of active power injected by the BESS are considered.

The LC values considering the injection of 5^{th} and 7^{th} harmonic current components are presented in Fig. 41, with phase angle ranging from 0° to 360°. In this analysis, the BESS injects 500 of active power, the amplitude of each harmonic current component is fixed in 5 A and the ambient temperature is considered 25°C. As noticed, the phase angle effects on lifetime consumption is more significant for low harmonic orders. In this context, the LC variation due to the phase angle is higher when the BESS is compensating the 5^{th} harmonic current component. This fact is explained by the inverter current waveform, since it presents more shape variations due to the harmonic phase angle. In addition, a phase shift is observed in the minimum and maximum LC values, which

can be explained by the different thermal impedances for each harmonic component.

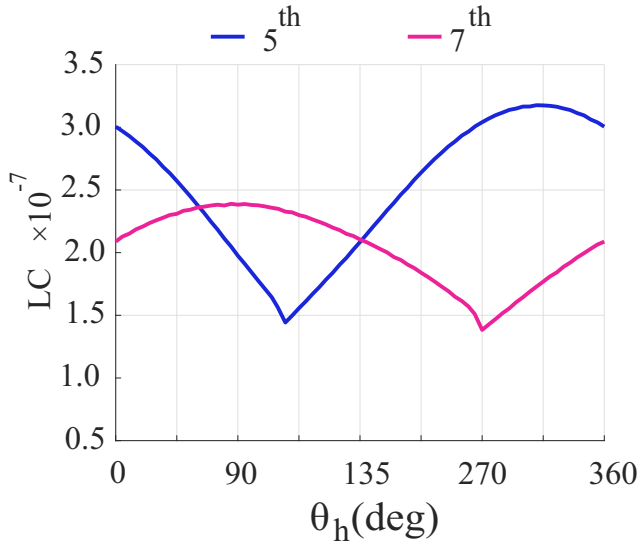

Figure 41 – The effect on the semiconductor LC due to harmonic phase angle variation. The active power is considered 500 kW, the ambient temperature 25^{o}C and the harmonic current amplitude is equal to 0.6 I_f.

Source: Own authorship.

The combination of multiple harmonics in the power system is usually observed under real operation conditions. In this context, the multiple harmonic compensation process should be considered. Thus, the LC is computed considering a nonlinear load composed of a sum of 5^{th} and 7^{th} harmonic current components. The phase angle variation for both harmonic components are considered. In Fig. 42, the BESS injects 500 kW, the ambient temperature is considered 25°C.

In Fig. 42(a), I_5 is considered equal to 0.6 I_f and I_7 is equal to 0.3 I_f . As observed, there are two critical LC areas for the IGBT. In Fig. 42(b) the I_5 was reduced to 0.3 I_f and I_7 was equal to 0.6 I_f. As noticed, the critical areas are also present. However, the LC values are lightly lower than previous case. In addition, in Fig. 42(c), the I_5 and I_7 are both equal to 0.6 I_f . In this case, there is a reduction in the LC critical areas. Thus, it is observed an increasing in the LC values with the harmonic current amplitude increasing. In addition, the compensation of the 5^{th} harmonic component is lightly higher than the 7^{th} harmonic. In the next section, the lifetime evaluation considering the mission profile operation is presented.

4.3 Case Study 2: HCC Based on Mission Profile Operation

The lifetime evaluation of the semiconductor devices and the dc-link capacitor are obtained based on a mission profile operation of the system during one year of operation.

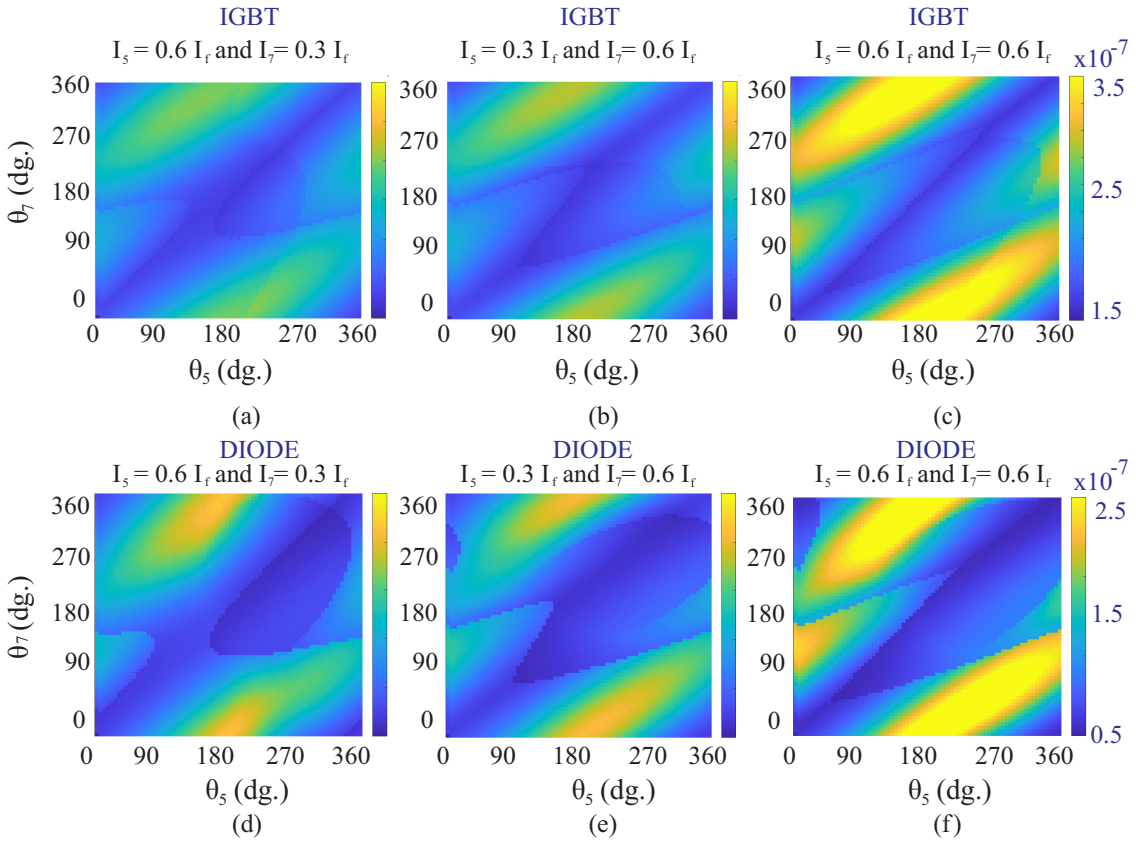

Figure 42 – LC of the semiconductor devices when the active power was equal to 500 kW and the ambient temperature equal to 25 ^{o}C. For the IGBT, the 5^{th} and 7^{th} harmonic components were compensated considering: (a) $I_5 = 0.6\ I_f$ and $I_7 = 0.3\ I_f$, (b) $I_5 = 0.3\ I_f$ and $I_7 = 0.6\ I_f$ and (c) $I_5 = 0.6\ I_f$and I_7= $0.6\ I_f$. For the diodes, the same study were provided: (d) $I_5 = 0.6\ I_f$ and $I_7 = 0.3\ I_f$, (e) $I_5 = 0.3\ I_f$ and $I_7 = 0.6\ I_f$ and (f) $I_5 = 0.6\ I_f$ and $I_7 = 0.6\ I_f$.

Source: Own authorship.

The mission profile of solar irradiance, ambient temperature and the power consumed by the load were used to generate the power profile of the battery bank, as presented in Chapter 3. These mission profiles were sampled with 1 minute per data in the city of Goiânia, Goiás (Brazil). The mission profiles are presented in Fig. 43.

Since the BESS operates with peak shaving function, the energy produced by the PV system is stored in the battery bank and it is injected to the grid during the peak hours. If the battery bank is fully charged, the energy produced by the PV is injected to the grid. The battery bank is charged until 17h and it injects the power to the grid during the time interval from 17h to 19h. In addition, the active power is observed by the load during the working days. Regarding the HCC operation, the BESS compensates the harmonic components from the nonlinear load during full time

Aiming to improve knowledge about the harmonic profiles, Fig. 44 shows the amplitude and phase angles used in this work. The harmonic profiles were measured from an industry park and also sampled at 1 minute per data. The harmonic amplitudes were

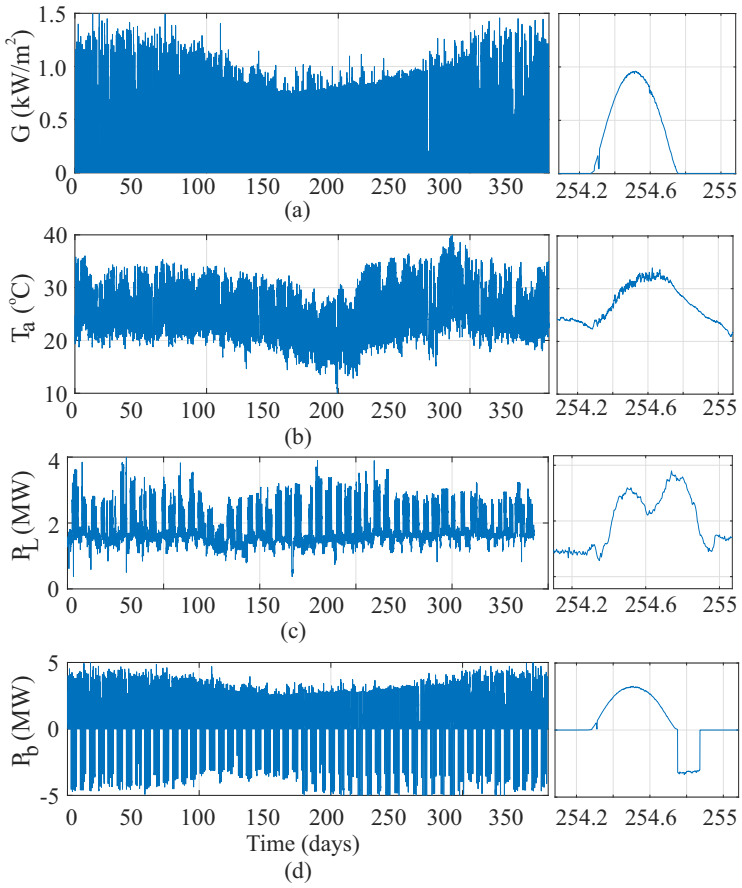

Figure 43 – Mission profiles of: (a) solar irradiance, (b) ambient temperature, (c) power consumed by the load and (d) battery bank power.

Source: Own authorship.

normalized to obtain the highest value equal to 100 A. This normalization is performed in order to have a considerable affect in the LC of the semiconductor devices. In addition, the histogram of the mission profiles, presenting the number of time (N_h) that each value appear in the profile, are also presented in Fig. 45.

The 5^{th} and 7^{th} harmonic current components are considered the current distortion in the nonlinear load. Those harmonic orders are selected for being very common in three-phase systems, based on studies on electrical systems in different types of commercial facilities (Yang; Zhou; Blaabjerg, 2016), (Sedo; Kascák, 2018). The active power reference for the inverter is provided based on the peak shaving operation, as presented in Fig. 24 in Chapter 4. Therefore, four cases are analyzed:

- Case 1: lifetime evaluation of the BESS dc/ac stage with peak shaving operation without HCC (base case);
- Case 2: lifetime evaluation of the BESS dc/ac stage with peak shaving operation and injecting only 5^{th} harmonic current component;

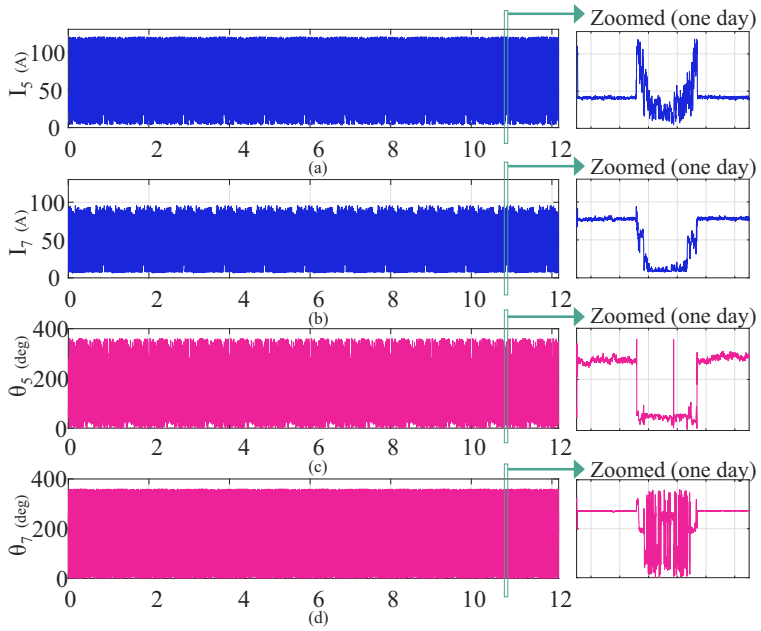

Figure 44 – Mission profile of: (a) 5^{th} harmonic amplitude, (b) 7^{th} harmonic amplitude, (c) 5^{th} harmonic phase angle and (d) 7^{th} harmonic phase angle.

Source: Own authorship.

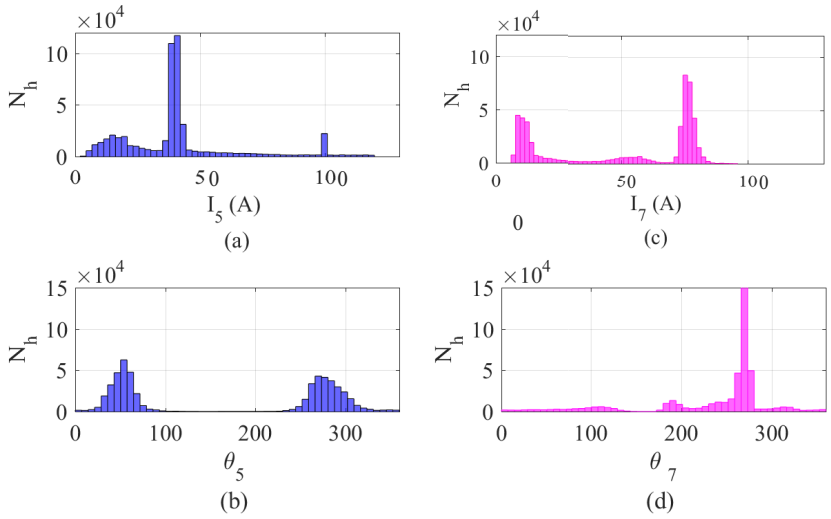

Figure 45 – Mission profile histogram of: (a) 5^{th} harmonic amplitude, (b) 7^{th} harmonic amplitude, (c) 5^{th} harmonic phase angle and (d) 7^{th} harmonic phase angle.

Source: Own authorship.

- Case 3: lifetime evaluation of the BESS dc/ac stage with peak shaving operation and injecting only 7^{th} harmonic current component;
- Case 4: lifetime evaluation of the BESS dc/ac stage with peak shaving operation and injecting 5^{th} and 7^{th} harmonic current components simultaneously.

The lifetime evaluation for the semiconductors devices and the dc-link capacitor are performed. For the semiconductors devices, the short and long cycles analysis are

carried out. In addition, the lifetime evaluation for the dc-link capacitor is performed based on the methodology presented in Chapter 4. Since the lifetime evaluation for the components were estimated, the Monte Carlo simulation considering 10.000 samples was applied to obtain the B_{10} of the system level.

4.3.1 Lifetime Evaluation of Semiconductor Devices

The four case studies are performed to evaluate the lifetime of the semiconductor devices. The damage in the IGBT and diode due to the short and long cycles are performed. Regarding the long cycles, the mean junction temperature of semiconductor devices in one year operation are presented in Fig. 46.

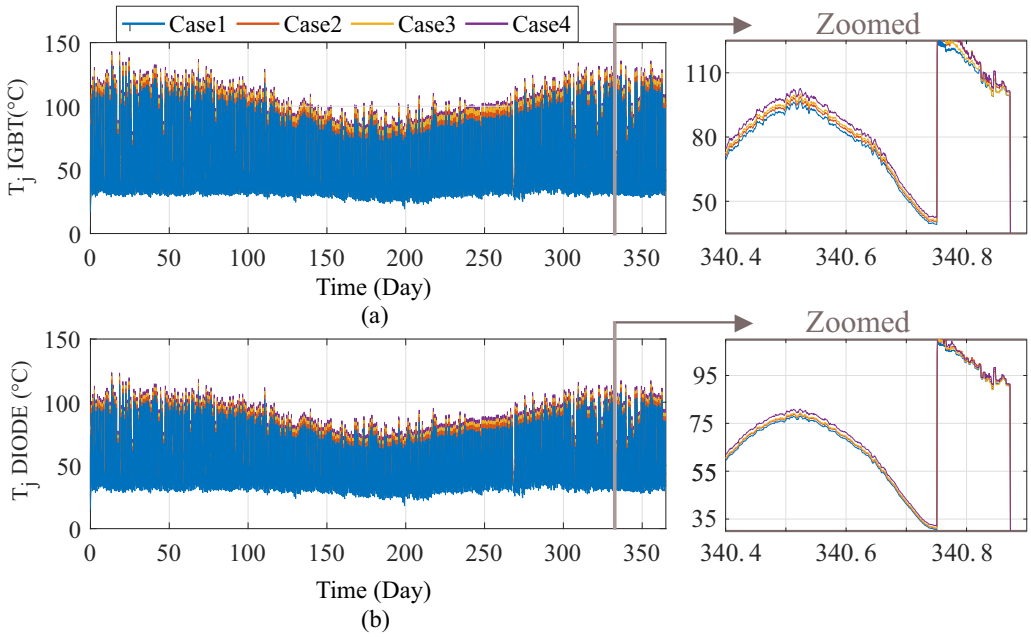

Figure 46 – Mean junction temperature for one year operation considering the long cycles analyzes for (a) IGBT and (b) diode.

Source: Own authorship.

As observed in Case 1, which is the base case, it presents the lowest junction temperature between all the cases. Thus, the HCC increases the mean junction temperature for the IGBT and diodes. In addition, the junction temperature for Case 3 is higher than that for Case 2, which means higher junction temperature when the 7^{th} harmonic component is compensated compared to the 5^{th} harmonic component. In addition, Case 4, which is the compensation of 5^{th} and 7^{th} harmonic components, presents the highest junction temperature. The same behavior is observed for the diode.

The annual lifetime consumption for IGBT and diodes considering the long and short cycles are presented in Table 7. The *LC* values are normalized based on the values of the base case *LC* (Case 1). As observed, the HCC operation increases the *LC* for the semiconductor devices considering the short and long cycles. Compared to the base case

(Case 1), it is observed an increasing of 21.3 %, 34.5 %, 52.0 % in the LC short cycle for Case 2, Case 3 and Case 4, respectively. With regarding to the diode LC, it is observed an increasing of 59.2 %, 62.1 %, 71.2 % in the short cycle LC for Case 2, Case 3 and Case 4, respectively. For the long cycle analysis, it is observed an increasing of 25.8 %, 43.7 %,74.0 % in the LC long cycle for Case 2, Case 3 and Case 4, respectively. With regarding to the diode LC, it is observed an increasing of 75.0%, 85.6 %, 91.1 % in the long cycle LC for Case 2, Case 3 and Case 4, respectively.

Table 7 – LC for the IGBT and diode considering the short and long cycles. LC for Case 1 considering: short IGBT = 0.0032; LC long IGBT = 0.012; LC short diode = 0.0010 and LC long diode = 0.010.

Cases	LC Short IGBT	LC Long IGBT	LC Short Diode	LC Long Diode
Case 1	1.000	1.000	1.000	1.000
Case 2	1.213	1.258	1.592	1.750
Case 3	1.345	1.437	1.621	1.856
Case 4	1.520	1.740	1.712	1.911

4.3.2 Lifetime Evaluation of Dc-link Capacitor

The lifetime evaluation of the dc-link capacitor is also evaluated. The same mission profiles used in the semiconductor devices lifetime analysis were considered. Therefore, the hot-spot temperature over one year is presented in Fig. 47.

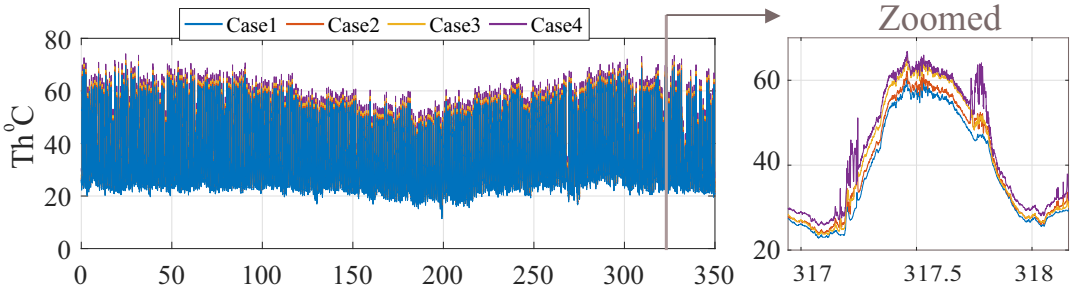

Figure 47 – Hot-spot temperature of one year operation for the dc-link capacitor.

Source: Own authorship.

As observed, the HCC increases the hot-spot temperature of the dc-link capacitor compered to the base case (Case 1). It is observed that the T_h is higher for Case 4, which is the harmonic compensation of the 5^{th} and 7^{th} harmonic components. In addition, the T_h for Case 3 is higher than that for Case 2, which means that the compensation of the 7^{th} harmonic component increases more the hot-spot temperature than the compensation of 5^{th} harmonic component.

In this context, the LC values for the cases considering one year mission profile is presented in Table 8. As observed, the lifetime consumption increases with the HCC

process. Compared to the base case, there is an increasing of 7,0 %, 12,8 % and 24,8 % for Case 2, Case 3 and Case 4, respectively.

Table 8 – LC for the dc-link capacitor considering one year mission profile. The LC base case is 0.0182.

Cases	LC
Case 1	1.000
Case 2	1.070
Case 3	1.128
Case 4	1.248

4.3.3 Monte Carlo Simulation Analyzes

Since the LC of each element over one year was performed, a Monte Carlo simulation analysis is applied to have a better understanding of the BESS dc/ac stage lifetime evaluation. Firstly, the unreliability function $F(x)$ for the system level considering the failure of the dc/ac stage caused only by a specific component is performed. Therefore, the unreliability considering each component can be analyzed. The $F(x)$ curve for each component is presented in Fig. 48.

As shown in Fig. 48 (a), considering the $F(x)$ for the BESS dc/ac stage based on the IGBT, it is observed reduction in the B_{10} due to the HCC operation. Compared to the base case, there are a reduction in B_{10} of 4.2, 8.4 and 18 years for Case 2, Case 3 and Case 4, respectively. The same behavior is observed for the diodes. However, the B_{10} are higher than these for the IGBT. Compared to the base case, there are a reduction of 0.8, 1.6 and 2.1 years for Case 2, Case 3 and Case 4, retrospectively. Finally, the $F(x)$ for the dc-link capacitor is presented in Fig. 48 (c). As observed, the B_{10} reduces due to the HCC process. Compared to the base case, there are a reduction in B_{10} of 2.2 , 4.9 and 7.4 and for Case 2, Case 3 and Case 4, respectively.

Finally, the unreliability function for the system level considering all the components are presented in Fig. 49. The B_{10} considering all the components in the Mont Carlo simulation is equal to 23.8, 28.0, 32.0 and 41.0 years for Case 1, Case 2, Case 3 and Case 4, respectively. Thus,it is observed a reduction in the reliability of the BESS dc/ac stage during the HCC. Compared to the base case there are a reduction of 4.2, 8.2, and 17.2 years for Case 2, Case 3 and Case 4, respectively.

4.4 Chapter Conclusions

The lifetime evaluation of semiconductor devices and the dc-link capacitor of the dc-ac stage were performed. The lifetime evaluation was performed based on the mission profile of battery bank power, harmonic current amplitude and phase angle, irradiance and

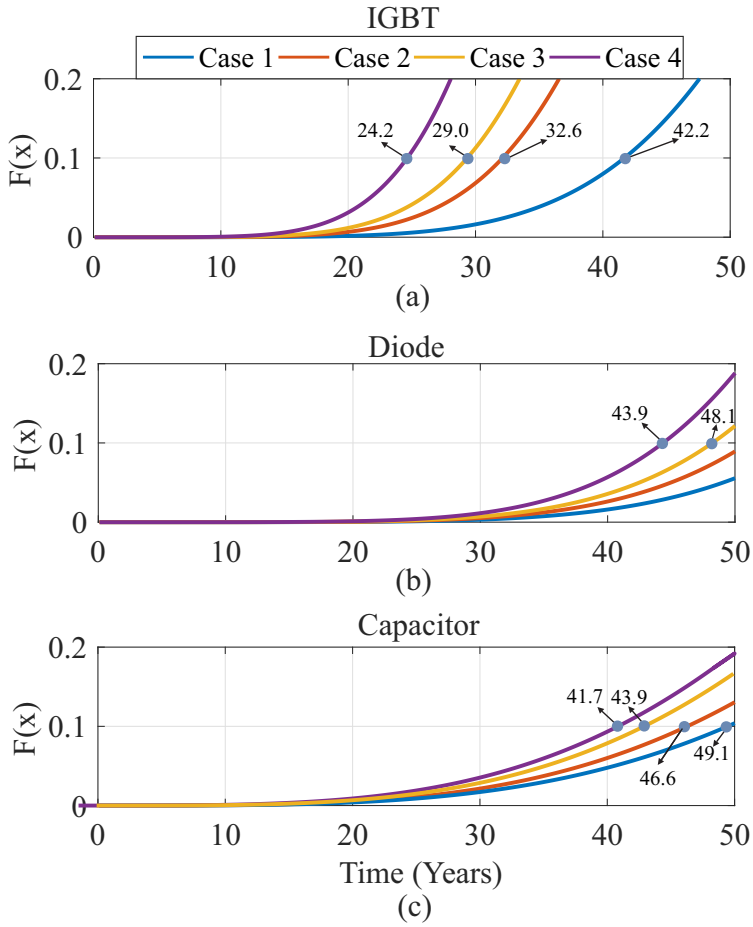

Figure 48 – Unreliability function considering the system level composed only of: (a) IGBT, (b) diode and (c) dc-link capacitor.

Source: Own authorship.

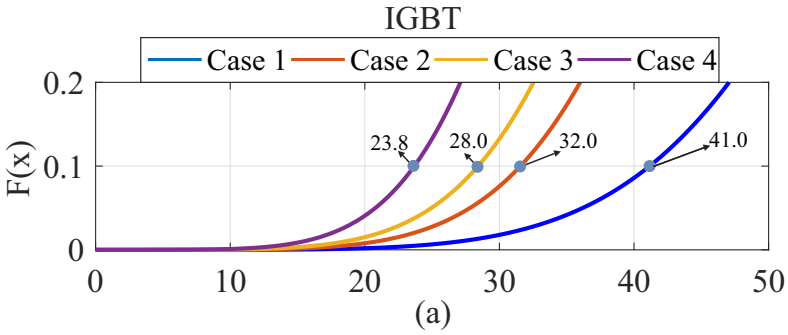

Figure 49 – Unreliability function considering the system level composed of all the components (IGBT, diode and dc-link capacitor)

Source: Own authorship.

ambient temperature. It was observed the increasing of the lifetime consumption of the semiconductor devices and dc-link capacitors due to the harmonic current compensation. In addition, it is observed a reduction the system level reliability, compared to the base case there are a reduction of 4.2, 8,2, and 17.2 years for Case 2, Case 3 and Case 4, respectively. In the next chapter, some experimental results are presented. The control

strategy used in this work and some thermal results are obtained and explained in this work.

5 Experimental Results

This chapter presents a laboratory test bench used to validate the BESS operating with peak shaving and HCC operation. The schematic of the test bench is explained and experimental results of the control strategy are presented. Experimental results with focus on the control strategy of the charge and discharge battery bank are preformed. In addition, thermal results of the dc-link capacitors and battery terminals are also performed. The experimental results of the lifetime evaluation of the semiconductor devises and dc-link capacitors are out of scope of this work.

5.1 Electrical Schematic of the Test Bench

The schematic of the test bench is shown in Fig. 50. As observed, there are two inverters (INV1 and INV2). In order to have a dc-link voltage at INV1 around 530 V, a 10 KVA transformer (220/380V) is connected to a three-phase diode rectifier bridge. In addition, the contactors K_0 and K_1 are used to perform the pre-load process.

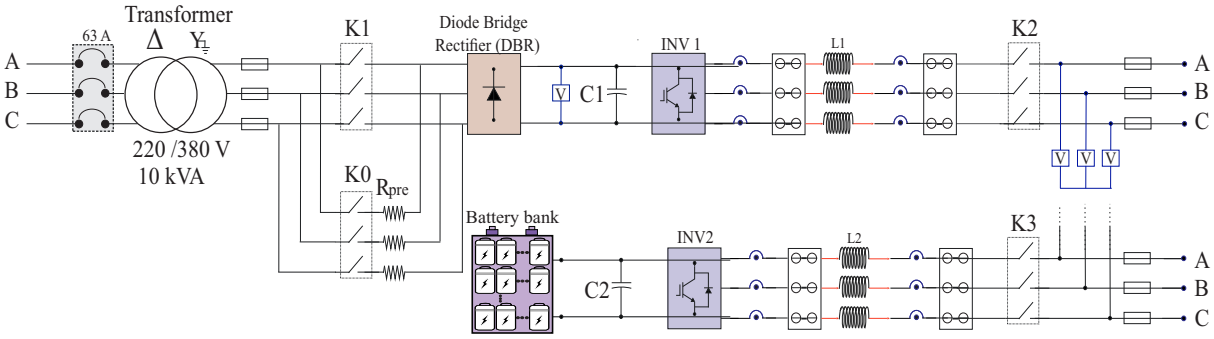

Figure 50 – Schematic of the laboratory test bench used in this work.

Source: Own authorship.

The dc-link of INV 2 is connected to a battery bank. In addition, INV1 and INV2 are interfaced to the grid by using L filter, which are responsible to filter the high harmonic frequencies from the inverters switching process. The contactors K_2 and K_3 are used to connect the INV1 and INV2 to the grid, respectively. The inverters used in this work are based on power module manufacture by Semikron. This module is composed by two three-phase inverters with separated dc-link. It is possible to connect the dc-link voltages of INV1 and INV2 to work as a back-to-back topology. However, in this work, the inverters are operating separately. Three dimensional model illustration for the power model is presented in Fig. 51. In addition, the main specification of the power modules are presented in the in Table 9.

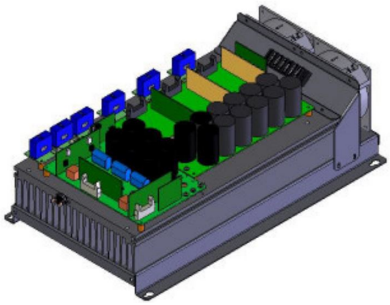

Figure 51 – Three-dimensional model of the power model used in the test bench (SEMIKRON, 2006).

Source: Own authorship.

Table 9 – Main parameter and specification of the power module.

Symbol	Parameter	Description
INV 1	IGBT bridge	25 A (125°C)/1200 V
INV 2	IGBT bridge	40 A (125°C)/1200 V
DBR	Three-phase diode bridge	70 A (80°C)/1600 V
BC	Braking chopper	25 A (125°C)/1200 V
C1	dc-link capacitor bank for B3	1.02 mF/750V
C2	dc-link capacitor bank for B4	2.04 mF/750 V
L1	Inductor Filter	1.8 mH
L2	Inductor Filter	1.8 mH
R_{pre}	Pre load resistor	20Ω

The inverter current output before and after the L filter of each inverter are measured. Thus, six LA-55-P(LEM) current sensors are used in the test bench. In addition, the grid voltage is also measured to perform the synchronism of the inverters to the electrical grid. In this context, the dc-link voltage for INV1 and INV2 are also measured by two LV-25-P(LEM) sensors. The measured signal for the voltage and current sensors are conditioned and connected to a Digital Signal Processing (DSP). In this work, a C2000 TMS320F28379D model is adopted. In addition, the Simulink - MATLAB environment is used to generate the code which is sent to the DSP. Thus, the control strategy is performed in block diagram and the system works in real time operation.

The battery bank is composed of twenty lead-acid batteries (12 V) connected in series. Thus, the nominal voltage of the INV2 dc-link is 240 V. The batteries are manufactured by WEG, with part number BAT0070122, and the main specification are presented in the Table 10. In addition, Fig. 52 is presented the test bench images, which is located at *Gerência de Especialista em Sistemas Elétricos de Potência* (GESEP).

For the experimental results of this work, only the INV 2 is used and the battery bank is considered the dc-link voltage. Thus, the battery bank and the INV 2 are the focus of study for this work. The control used in this work for INV2 is presented in Fig. 53. As observed, there is only one loop, which is the current loop, since the dc-link is not

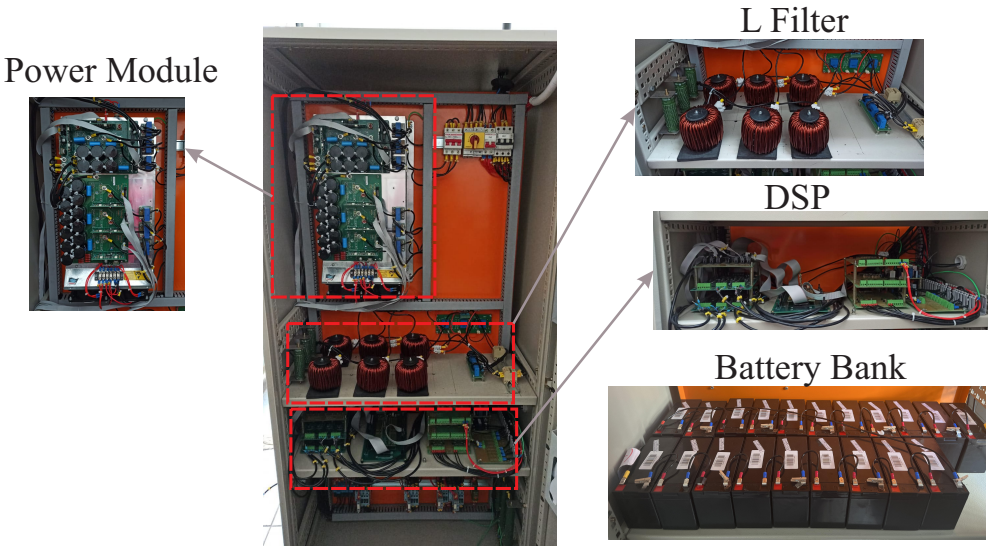

Figure 52 – Images of the laboratory test bench used in this work.

Source: Own authorship.

Table 10 – Electrical specification of the battery used in this work.

Parameters	Value
Nominal voltage	12 V
Float voltage	13.8 V
Capacity (Ah)	7Ah (20h until 10.5 V)
Internal resistance	32 mΩ
Maximum Charge Current	2.1 A

controlled and it is equal to battery bank voltage. As observed, the INV2 output current is measured and used in the control loop. In addition, the control is based stationary reference frame coordinates (α and β). The reference for the inverter current ($I_{inv}{}^{*}$) can be updated in real time operation. The PMR controller is adopted in the this work.

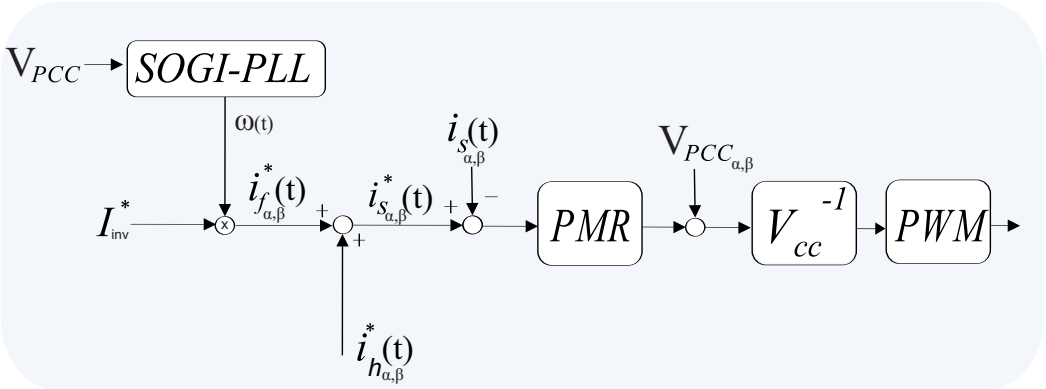

Figure 53 – Control block diagram for INV1 and INV2.

Source: Own authorship.

5.2 Validation of the Control Adopted Strategy

The results of synchronization of INV2 to the grid is presented in Fig. 54. The grid voltage measurement for phase a and the estimated angle Θ (t) by the SOGI-PLL are presented. As observed, the synchronization achieved by the SOGI-PLL is satisfactory. In addition, the this synchronization with is used to generate the harmonic current references.

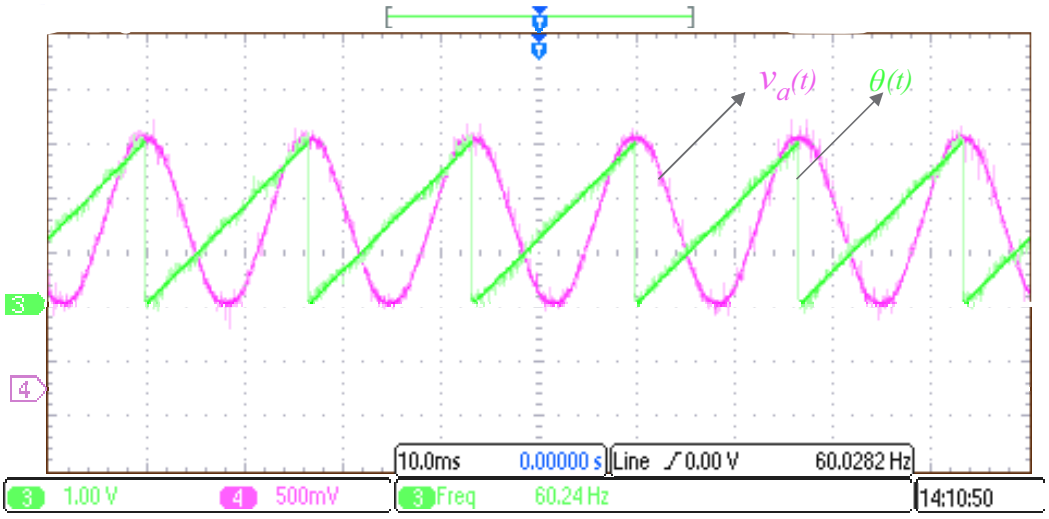

Figure 54 – SOGI-PLL performance: synchronization of the line voltage and $w(t)$ waveforms.

Source: Own authorship.

The output current of the inverter are presented in Figure 55. In this case, the reference of the inverter currents were performed to obtain an injection of 6 A of fundamental current and: 2 A of 5^{th} harmonic component with phase-angle 180^o in Figure 55(b), 2 A of 7^{th} harmonic component with phase-angle 180^o in Figure 55(c) and 2 A of 5^{th} and 7^{th} harmonic components with phase-angle 180^o in Figure 55(d). In addition, in Figure 55(a) only the injection of the 6 A of fundamental current is performed. The harmonic spectrum of the inverter current output is presented in Figure 56 to validate the waveforms presented in Fig.55.

The battery bank charging and discharging process are analyzed in Fig. 57 and the output of the invert and battery bank currents are presented. As observed in Fig. 57 (a), during the charging process, 3.5 A of fundamental current are drained from the grid to charge the battery bank. For the discharging process, 3.5 A are also considered as the inverter current reference. As observed, the Root Mean Square (RMS) current of the battery bank during the charge process was equal to 1.3 A and for the discharge process the battery bank current was equal 2.2 A. This fact is explained based on the voltage drop at the internal resistance of the battery bank. As observed, with the control strategy adopted in this work, it is possible to charge and discharge the battery bank based on the INV2 connected to the electrical grid.

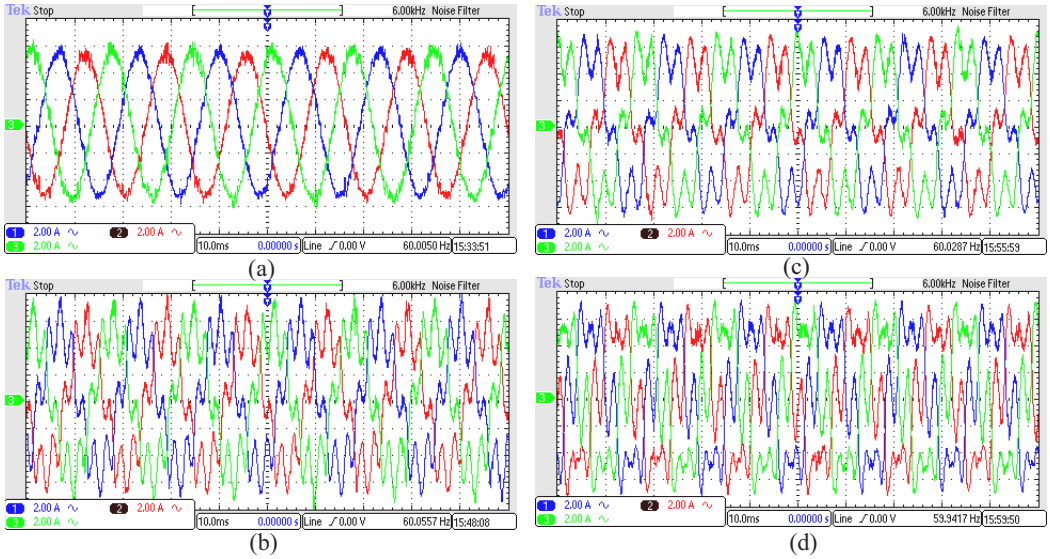

Figure 55 – Output current of a three-phase PV inverter injecting: (a) 6 A of I_f and: (b) 2 A of I_5 with $\theta_h = 180^o$, (c) 2 A of I_7 with $\theta_h = 180^o$ and (d) 2 A of I_5 and I_7 with $\theta_h = 180^o$.

Source: Own authorship.

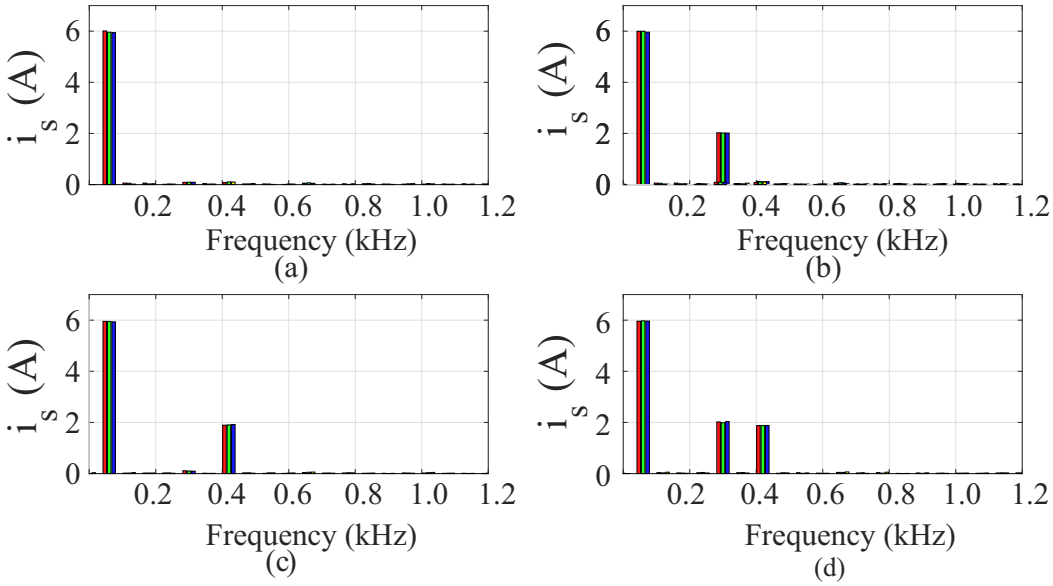

Figure 56 – Spectrum current of a three-phase PV inverter injecting: (a) 6 A of I_f and: (b) 2 A of I_5 with $\theta_h = 180^o$, (c) 2 A of I_7 with $\theta_h = 180^o$ and (d) 2 A of I_5 and I_7 with $\theta_h = 180^o$.

Source: Own authorship.

The same analysis is performed when the battery bank is charged and discharged with the injection of the harmonic current component. This fact is observed in Fig. 57 (b). The reference of the inverter fundamental current is also equal to 3.5 A and the 1 A of 5^{th} harmonic is considered constant during the charge and discharge process. In addition, the RMS current for the battery bank current was equal to 1.5 A during the charge process and 2.6 A during the discharge process. As can be observed, with the HCC operation,

the battery bank current presents more oscillation and a higher battery bank current compared to the traditional operation (presented in Fig. 57 (a)).

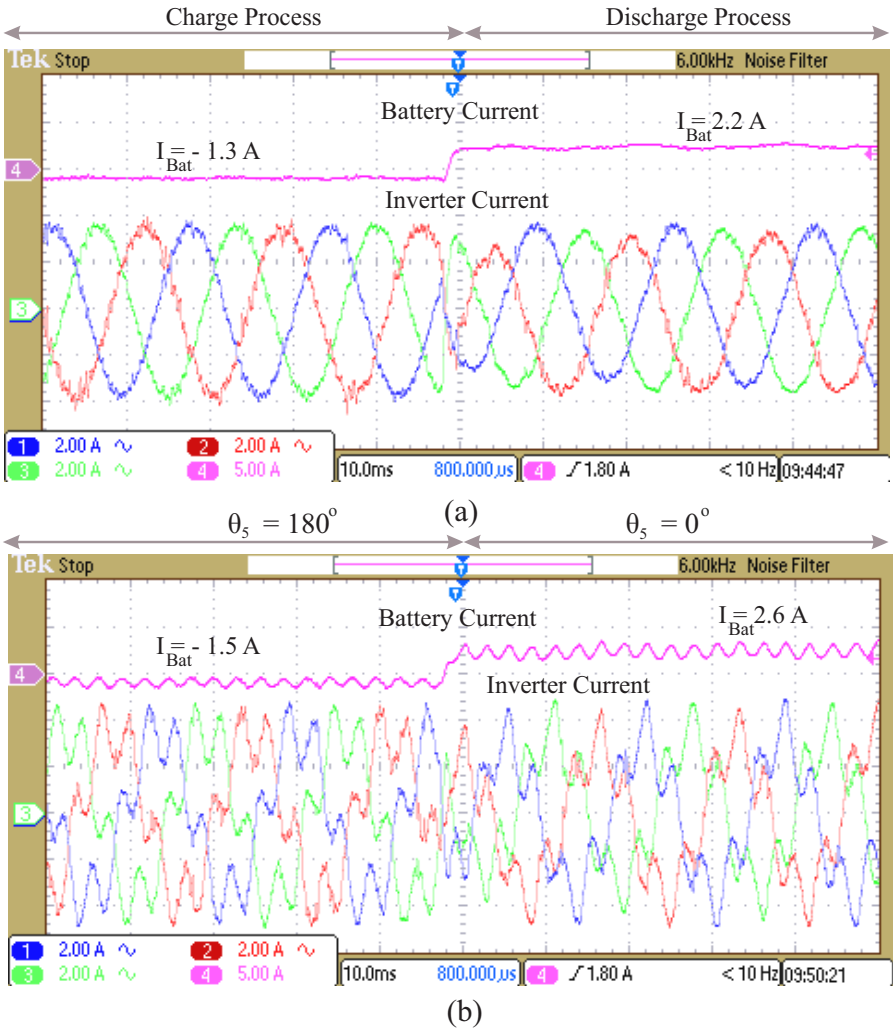

Figure 57 – Waveforms of the inverter and battery bank currents with I_f equal to 3.5 A: (a) without harmonic current compensation and (b) With harmonic current compensation (I_5 equal to 1 A).

Source: Own authorship.

The control strategy is also validated considering the real time operation of the proposed system. Thus, the charge and discharge process of the battery bank are performed based on the typical behavior of a peak shaving operation. The battery bank was charged during 11 hours, simulating a theoretical energy generation by a PV inverter in a sunny day. Thus, the amplitude of the fundamental inverter current to charge the battery bank is presented in Fig. 58. As observed, after 11 hours, the energy stored to the battery bank is injected to the grid during three hours, simulating the peak time. An algorithm was implemented in the DSP to calculate the stored energy during the charge process and perform the inverter current reference for the discharge process.

Respecting the limits of energy, voltage and current supported by the battery used

in this work, the maximum inverter current reference used to charge the battery bank was 1 A. The battery bank voltage (V_{bb}) is presented in Fig. 58 (b). The V_{bb} was obtained with a sampling time equal to 5 minutes. As observed, the battery bank presents the same voltage value at the beginning and in the end of the experiment. The initial battery bank value was 245 V, achieving 266 V during the charging process. The lowest voltage achieved during the discharging process is 240 V.

As observed in Fig. 58, the battery bank voltage decreases during the time from 8.0 to 11.0 hours, even during the charge process. This fact is explained based on the voltage drop over the internal resistance of the batteries. In addition, there is a voltage drop of 4.4 V in the battery bank at the transition of the charge and discharge process (11h), which is also explained based on the voltage drop over the internal resistance of the batteries.

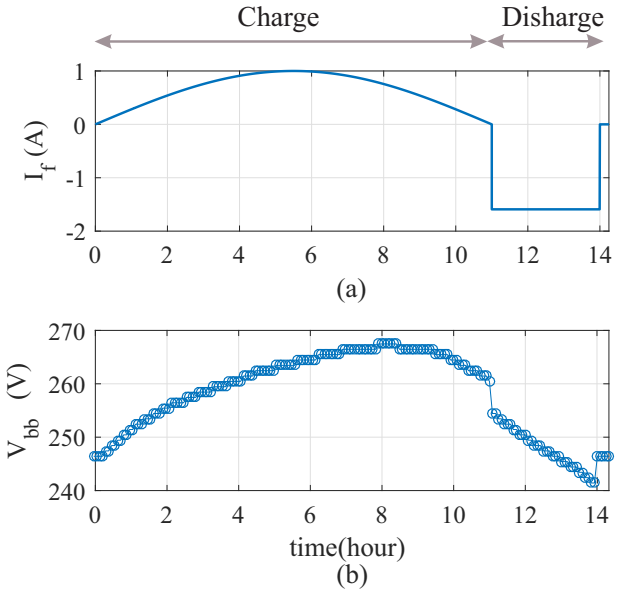

Figure 58 – Charging and discharging performance of the battery bank (a) fundamental current reference of the inverter and (b) battery bank voltage.

Source: Own authorship.

5.3 HCC Effect on the dc-link capacitors

In this section, the effect of the HCC operation on the dc-link is presented. INV1 was used instead of INV2 for this experiment. This choice was performed to obtain a constant dc-link voltage (530 V), since the dc side of INV2 is connected to the battery bank. The capacitor bank of INV1 is composed by six capacitors (2 strings in parallel and each string is composed of 3 capacitor). The capacitors are named as C_1 to C_6, as presented in Fig. 59.

Figure 59 – Capacitor bank of INV1 with the specification of C_1 to C_6.

Source: Own authorship.

The thermal analysis were performed based on the temperature measured of the capacitors. The temperatures were measured using a thermal camera (FLIR E75) and for numerical evaluation, the high-precision Jumper JPD-FR202 thermometer was used. The temperature were measured in the external area (on the top) of the capacitors. For the specific experiment, four cases were considered:

- Case 1: I_f equal to 4 A (only fundamental current is injected to the grid);
- Case 2: I_f equal to 4 A and I_5 equal to 2 A;
- Case 3: I_f equal to 4 A and I_7 equal to 2 A;
- Case 4: I_f equal to 4 A, I_5 and I_7 equal to 2 A.

Each experiment was performed considering the same duration time of 80 minutes, which was sufficient to achieve the steady state temperature of the dc-link capacitor. The thermal images obtained of the capacitors top are presented in Fig. 60 and the temperatures from the the high-precision Jumper sensor are presented in Table 11.

Table 11 – Temperatures (in degree) values of the dc-link capacitors.

Cases	C_1	C_2	C_3	C_4	C_5	C_6
Case 1	29.3 °C	30.4 °C	28.1 °C	30.1 °C	31.7 °C	31.1 °C
Case 2	30.1 °C	31.4 °C	29.4 °C	30.7 °C	32.6 °C	31.9 °C
Case 3	30.1 °C	31.6 °C	29.5 °C	30.9 °C	32.9 °C	31.9 °C
Case 4	30.5 °C	32.5 °C	29.9 °C	31.0 °C	33.3 °C	32.2 °C

As observed in the thermal images, there is an increase in the capacitors temperature due to the HCC operation mode. In addition, some capacitor are more thermal stressed than others. In this context, the C_5 is the most stressed and C_3 is the

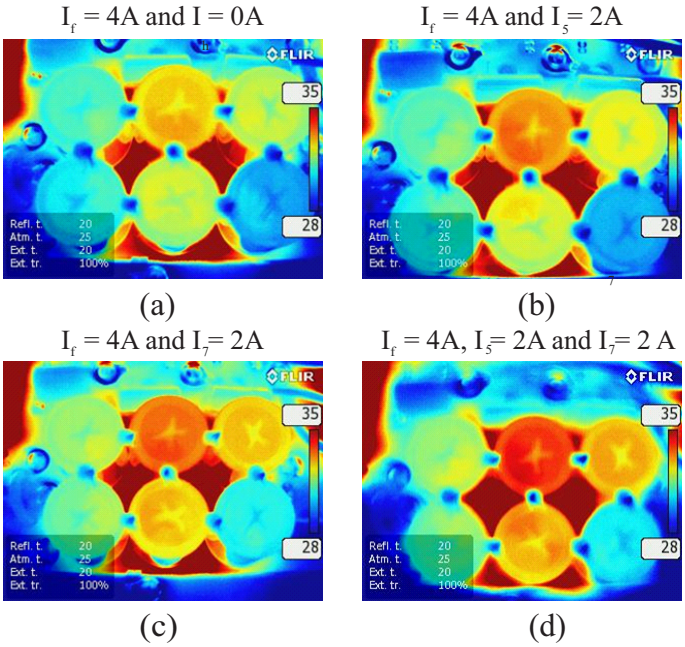

Figure 60 – Thermal images of current capacitor bank for: (a) Case 1, (b) Case 2, (c) Case 3 and (d) Case 4.

Source: Own authorship.

lesser stressed. Considering the capacitor with the higher temperature (C_5), it is observed an increasing of 0.9 C^o, 1.2 C^o, 1.6 C^o when the Case 2, Case 3 and Case 4 are compared to the Case 1 (base case). Thus, it is observed the increasing of the capacitor temperature due to the HCC operation.

5.4 HCC Effect on the Battery Bank

The thermal analysis of the batteries during the HCC operation mode was also performed. For this experiment, the equipment NI9213, manufactured by National Instruments, was used and it is presented in Fig. 61. This equipment measures the voltage signals from thermocouples with a sampling of 60 measurements per second. The thermocouples (type k) were connected to the external positive born of the batteries. The measurement of the ambient temperature was also obtained to estimate the increasing of the temperature compared to the ambient temperature.

The temperature of the batteries were obtained considering the experiment presented in Fig. 58, which the battery bank was charged for 11 hours and discharged for 3 hours. The batteries and the ambient temperature are presented in Fig. 62 (a). As observed, compared to the ambient temperature, there is an increasing in the batteries temperature due to the charging and discharging process. The difference of the batteries temperatures and the ambient temperature are presented in Fig. 62 (b).

In addition, the temperature of the batteries are very similar since the batteries

Figure 61 – Representation of a NI9213 manufactured by National Instruments.

Source: Own authorship.

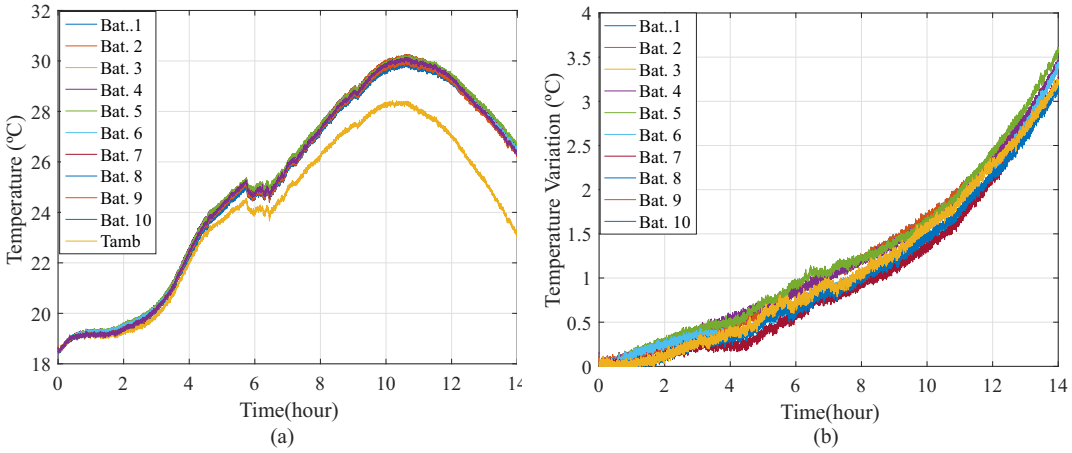

Figure 62 – Measurements of the batteries and ambient Temperatures in (a) and temperature variation of the batteries comparing to the ambient temperature (b).

Source: Own authorship.

were obtained at the same time from the same manufactured. It is important to note the increasing of the batteries temperature due to the charging and discharging process. There is an increasing of almost 3.25 C^o at the end of the experiment. Also, during the discharge process, the battery temperature presents a higher increasing, since there are more current drained from the batteries.

The temperature of the batteries during the HCC operation were also performed. The battery bank were discharged for three hours considering the following cases:

- Case 1: I_f equal to 4 A (only fundamental current is injected to the grid);
- Case 2: I_f equal to 4 A and I_5 equal to 2 A;
- Case 3: I_f equal to 4 A and I_7 equal to 2 A;
- Case 4: I_f equal to 4 A, I_5 equal to 2 A and I_7 equal to 2 A.

The temperature of the batteries were measured in all the fours cases and the increasing of the temperature in relation to the ambient temperature are presented in Fig. fig:tempbat. The average of temperature from the then batteries was considered for reach case. As observed, the HCC operation increases the temperature of the batteries. Comparing to the base case, there is an increasing of 0.2 °C when the 7^{th} is injected, 0.35 °C when the 5^{th} is injected and 0.6 C^o when the 5^{th} & 7^{th} are injected.Thus, the temperature increasing is more significant when the 5^{th} and 7^{th} are injected simultaneously.

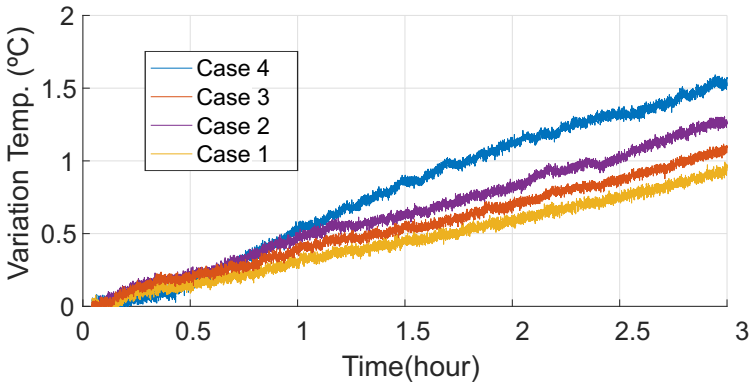

Figure 63 – Temperature variation of the batteries compared to the ambient temperature.

Source: Own authorship.

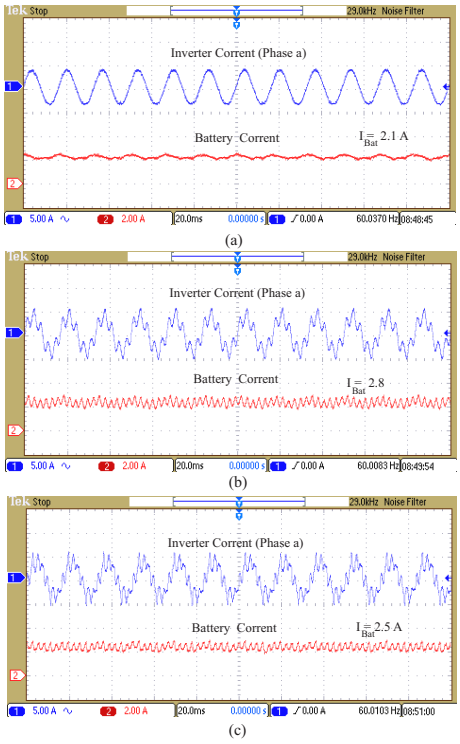

Figure 64 – Inverter and battery bank current considering: (a) Case 1, (b) Case 2 and (c) Case 3.

Source: Own authorship.

In order to have a better understanding of the HCC effect on the battery

temperature, the inverter and battery bank for Case 1, Case 2 and Case 3 are presented in Fig. 64. As observed, due to the harmonic current injection, the battery bank current presents more oscillation. This oscillation is more significant when the 5^{th} harmonic is injected. With regard to the RMS current of the battery bank, it is observed an increasing in the RMS of 0.7 A and 0.4 A when the 5^{th} and 7^{th} harmonic component are injected (compared to the base case), respectively.

The spectrum of the battery bank current are presented in Fig. 65. As observed, there is a considerable 6^{th} harmonic component when the HCC operation is performed, compared to the base case. In addition, this 6^{th} harmonic component is higher for Case 2, which directly increases the RMS current of battery bank for this case. It is also observed a presence of the second harmonic for all the cases, which is explained based on the grid voltage unbalance.

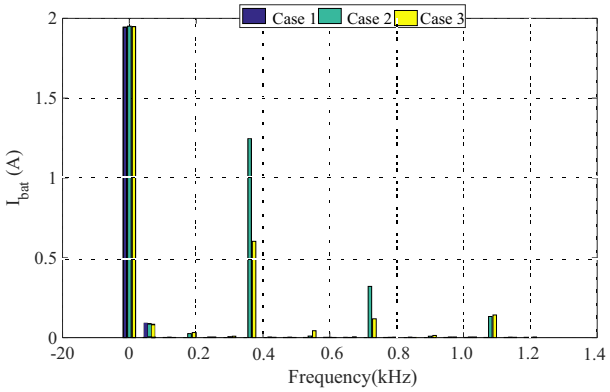

Figure 65 – Spectrum of the battery bank current considering: (a) Case 1, (b) Case 2 and (c) Case 3.

Source: Own authorship.

5.5 Chapter Conclusions

In this chapter some experimental results of inverter with a battery bank are presented. The results of the control strategy used to charge and discharge the battery bank are presented. The peak Thermal results of the capacitor and battery bank are presented. As observed, there is an increasing in the temperature in these components when the HCC operation is performed. In addition, the temperature increasing is even more significant when the 5^{th} and 7^{th} are injected simultaneously.

6 Closure

In this chapter, the conclusions regarding this work are presented. The conclusion achieved in the previous chapters are pointed out. Finally, proposals for continuity of this research are presented.

6.1 Conclusions

This work presented the challenges related to the BESS operating with HCC operation. Firstly, a methodology to size the battery bank is proposed. The methodology was applied to peak shaving operation as an example. In addition, a methodology used to estimate the lifetime consumption of an BESS dc/ac stage during the HCC operation process was also presented. In this context, the lifetime evaluation of dc/ac stage of a BESS based on real time mission profile was performed. Thus, the lifetime evaluation based on the short and long cycles for the semiconductor devices was evaluated. In addition, the lifetime evaluation of the dc-link capacitor was also considered. Finally, experimental results based on a laboratory bench is presented. The conclusion of this work can be divided in three parts:

- Battery bank selection based on OPEX and CAPEX concepts;
- Semiconductor devices lifetime evaluation considering the BESS ac/dc stage during peak shaving and HCC operation mode;
- Experimental results in the laboratory test bench.

6.1.1 Battery Choice Based on OPEX and CAPEX Analysis

- Based on the proposed methodology, the battery choice can be related to the six factors: BESS dc/ac stage dc-link voltage, battery bank volume, battery bank power losses, stored capacity index, battery lifetime and total battery bank price;
- Based on the proposed methodology, the user can select the battery according to the relative importance given to the OPEX and CAPEX concepts;
- The proposed methodology can be modified by the user. More or less criteria can be considered in the analysis.

6.1.2 Lifetime Evaluation of Semiconductor Devices During HCC Operation Mode

- The lifetime evaluation for the BESS inverter during the HCC operation is affected by the harmonic contents (h, I_h, and θ_h) which are compensated;
- The increasing of the compensated harmonic amplitude increases the semiconductor devices lifetime consumption;
- The effect of the harmonic phase angle on the the semiconductor devices lifetime consumption is higher for low harmonic order;
- The lifetime consumption in the semiconductor devices are higher when the 5^{th} and 7^{th} harmonic component are compensated simultaneously;
- The B_{10} considering all the components in the Mont Carlo simulation is equal to 23.8, 28.0, 32.0 and 41.0 years for Case 1, Case 2, Case 3 and Case 4, respectively. Thus,it is observed a reduction in the reliability of the BESS dc/ac stage during the HCC. Compared to the base case, there are a reduction of 4.2, 8.2, and 17.2 years for Case 2, Case 3 and Case 4, respectively.

6.1.3 Experimental Results in the Test Bench

- The synchronism of the two inverters connected to the grid is also satisfactory;
- The control strategy used in the HCC and peak shaving operation was validated.
- The HCC operation increases the external temperature of the dc-link capacitors. For the experiment presented in this work, an increasing of 1.6^oC was observed when the 5^{th} and 7^{th} harmonic are compensated simultaneously.
- The HCC operation increases the external temperature of the batteries. For the experiment presented in this work, an increasing of 0.6 C^o was observed when the 5^{th} and 7^{th} harmonic are compensated simultaneously.

6.2 Next steps - Propose

For future researches of this work, the following topic will be study:

- Apply the methodology the choose of the battery of the BESS considering other cases studies and different batteries technologies;
- Explore the effect of the HCC operation on the battery bank.

- Improve the laboratory test bench performing remote control.

References

Abba, M.; P. Luigi; Saeedallah, M.; G.Mohammad. Coordinated operation of energy storage systems for distributed harmonic compensation in microgrids. *Energies*, v. 13, n. 3, 2020. 27

Ahmed, S. D.; Al-Ismail, F. S. M.; Shafiullah, M.; Al-Sulaiman, F. A.; El-Amin, I. M. Grid integration challenges of wind energy: A review. *IEEE Access*, v. 8, p. 10857–10878, 2020. 24

Andresen, M.; Ma, K.; De Carne, G.; Buticchi, G.; Blaabjerg, F.; Liserre, M. Thermal stress analysis of medium-voltage converters for smart transformers. *IEEE Trans. on Power Electronics*, v. 32, n. 6, p. 4753–4765, 2017. 77

ANEEL. *ANEEL Agência Nacional de Energia Elétrica*. 2022. Available in: <https://www.gov.br/aneel/pt-br>. 60

Ashby, M.; Cebon, D. Materials selection in mechanical design. *Letter Journal Physics*, v. 3, p. 1–9, 1993. 29

Bernal-Agustín, J.; Dufo, R. Simulation and optimization of stand-alone hybrid renewable energy systems. *Renewable and Sustainable Energy Reviews*, v. 13, n. 8, p. 2111–2118, 2009. 40

Byrne, R. H.; Nguyen, T. A.; Copp, D. A.; Chalamala, B. R.; Gyuk, I. Energy management and optimization methods for grid energy storage systems. *IEEE Access*, v. 6, p. 13231–13260, 2018. 27, 28

Chai, J.; Liu, J.; Ngai, E. Application of decision-making techniques in supplier selection: A systematic review of literature. *Expert Systems with Applications*, v. 40, n. 10, p. 3872 – 3885, 2013. 39, 58

Chargex. *Chargex - Lithium Ion Batteries*. [S.l.], 2021. Available in: <www.lithiumion-batteries.com/products/12-volt-lithium-batteries/>. 62

Chen, A.; Sen, P. K. Advancement in battery technology: A state-of-the-art review. In: *2016 IEEE Industry Applications Society Annual Meeting*. [S.l.: s.n.], 2016. p. 1–10. 27

Citro, C.; Luna, A.; Rocabert, J.; Muñoz-Aguilar, R. S.; Candela, I.; Rodriguez, P. Overview of power processing structures for embedding energy storage in pv power converters. In: *IECON 2011 - 37th Annual Conference of the IEEE Industrial Electronics Society*. [S.l.: s.n.], 2011. p. 2492–2498. 35, 36, 37

Cupertino, A. F.; Amorim, W. C. S.; Pereira, H. A.; Seleme Junior, S. I.; Chaudhary, S. K.; Teodorescu, R. High performance simulation models for es-statcom based on modular multilevel converters. *IEEE Transactions on Energy Conversion*, v. 35, n. 1, p. 474–483, 2020. 53

de Barros, R.; S. Brito, E.; G.G. Rodrigues; Mendes, V.; Cupertino, A.; Pereira, H. Lifetime evaluation of a multifunctional pv single-phase inverter during harmonic current

compensation. *Microelectronics Reliability*, v. 88-90, p. 1071–1076, 2018. 29th European Symposium on Reliability of Electron Devices, Failure Physics and Analysis (ESREF 2018). 71, 74

de Barros, R. C.; da Silveira Brito, E. M.; Boaventura, W.; Pereira, H. A.; Cupertino, A. F. Methodology for bondwire lifetime evaluation of multifunctional pv inverter during harmonic current compensation. *International Journal of Electrical Power Energy Systems*, v. 128, p. 106711, 2021. 76

Díaz-González, F.; Sumper, A.; Gomis-Bellmunt, O. *Energy storage in power systems*. [S.l.]: John Wiley & Sons, 2016. 9, 25

Divya, K.; Ostergaard, J. Battery energy storage technology for power systemsan overview. *Electric Power Systems Research*, v. 79, n. 4, p. 511–520, 2009. 33

Downing, S.; Socie, D. Simple rainflow counting algorithms. *International Journal of Fatigue*, v. 4, n. 1, p. 31–40, 1982. 40

Falck, J.; Felgemacher, C.; Rojko, A.; Liserre, M.; Zacharias, P. Reliability of power electronic systems: An industry perspective. *IEEE Industrial Electronics Magazine*, v. 12, n. 2, p. 24–35, 2018. 39, 49

Falcones, S.; Ayyanar, R. Simple control design for a three-port dc-dc converter based pv system with energy storage. In: *2010 Twenty-Fifth Annual IEEE Applied Power Electronics Conference and Exposition (APEC)*. [S.l.: s.n.], 2010. p. 2149–2153. 37

Farahani, R.; SteadieSeifi, M.; Asgari, N. Multiple criteria facility location problems: A survey. *Applied Mathematical Modelling*, v. 34, n. 7, p. 1689 – 1709, 2010. 38, 55

Farihan, M.; .Jiashen, T.; Ching-Ming, L.; Liang-Rui, C. Development of energy storage systems for power network reliability: A review. *Energies*, v. 11, n. 9, 2018. 27

Fathima, H.; Palanisamy, K. Optimized sizing, selection, and economic analysis of battery energy storage for grid-connected wind-pv hybrid system. *Hindawi*, v. 2015, n. 713530, p. 1–16, 2015. 27, 28, 29

Feix, G.; Dieckerhoff, S.; Allmeling, J.; Schonberger, J. Simple methods to calculate igbt and diode conduction and switching losses. In: *2009 13th European Conference on Power Electronics and Applications*. [S.l.: s.n.], 2009. p. 1–8. 54

Gopi, L. R.; TolberT, L. M.; Ozpineci, B.; Pinto, J. O. P. Rainflow algorithm-based lifetime estimation of power semiconductors in utility applications. *IEEE Transa. Ind. Appl.*, v. 51, n. 4, p. 3368–3375, July 2015. 73

Horiba, T. Lithium-ion battery systems. *Proceedings of the IEEE*, v. 102, n. 6, p. 939–950, 2014. 33, 34

Hshiung, G. H.; Dieckerhoff, J.; Huang, J. In: *MultiplAttribute Decision Making - Methods and Applications*. [S.l.: s.n.], 1981. 38, 55

Huang, H.; Mawby, P. A. A lifetime estimation technique for voltage source inverters. *IEEE Trans. Power Electron.*, v. 28, n. 8, p. 4113–4119, Aug 2013. 48, 73

Ibrahim, H.; Ilinca, A.; Perron, J. Energy storage systemscharacteristics and comparisons. *Renewable and Sustainable Energy Reviews*, v. 12, n. 5, p. 1221–1250, 2008. 33

Infineon. *HighspeedDuoPack:IGBTinTrenchandFieldstoptechnologywithsoft,fast recoveryanti-paralleldiode*. [S.l.], 2014. 53

Jha, N.; Kumar, R.; Kumari, A.; Bepari, B. Design, development and implementation of a robust decision support expert system (brandec) in multi criteria decision making. *Procedia Engineering*, v. 97, p. 1853 – 1865, 2014. 12th Global Congress on Manufacturing and Management GCMM - 2014. 38

Jiang, X.; N. Guoliang; L.Hao; G.Zhimin; Z. Qingshan; J.Yang. Optimization of battery energy storage system capacity for wind farm with considering auxiliary services compensation. *Applied Sciences*, v. 8, n. 10, 2018. 26, 27

Jinkui, H.; Yang, Y.; Vinnikov, D. Energy storage for 1500 v photovoltaic systems: A comparative reliability analysis of dc- and ac-coupling. *Energies*, v. 13, n. 13, 2020. 29

Kamali, S.; Tyagi, V.; N.A.Rahim; Panwar, N.; Mokhlis, H. Emergence of energy storage technologies as the solution for reliable operation of smart power systems: A review. *Renewable and Sustainable Energy Reviews*, v. 25, p. 135–165, 2013. 24

Kazmierkowski, M. P. Energy storage: Systems and components [book news]. *IEEE Industrial Electronics Magazine*, v. 12, n. 4, p. 48–48, 2018. 32

Lander, J. Further studies on the anodic corrosion of lead solutions. *Journal of The Electrochemical Society*, The Electrochemical Society, v. 103, n. 1, p. 1, 1956. 42

Lenz, J. M.; Pinheiro, J. R. Mission profile impact on capacitor reliability in pv single-stage inverters. In: *7th ICRERA*. [S.l.: s.n.], 2018. p. 976–981. 49

Linden, D.; Reddy, T. Handbook of batteries. *McGraw-Hill Professional*, v. 3, p. 1–1200, 2001. 27

Lopez, D.; Arcos, C.; Sevil, T.; Sergio, J.; Berna, J. Comparison of lead-acid and li-ion batteries lifetime prediction models in stand-alone photovoltaic systems. *Applied Sciences*, v. 11, n. 3, 2021. 33

Ma, K.; Bahman, A. S.; Beczkowski, S.; Blaabjerg, F. Complete loss and thermal model of power semiconductors including device rating information. *IEEE Trans. on Power Electronics*, v. 30, n. 5, p. 2556–2569, 2015. 77

Ma, K.; F. Blaabjerg. Reliability-cost models for the power switching devices of wind power converters. In: *3rd IEEE International Symposium on Power Electronics for Distributed Generation Systems*. [S.l.: s.n.], 2012. p. 820–827. 47, 48

Ma, K.; Liserre, M.; Blaabjerg, F.; Kerekes, T. Thermal loading and lifetime estimation for power device considering mission profiles in wind power converter. *IEEE Trans. Power Electronics*, v. 30, n. 2, p. 590–602, Feb 2015. 45, 46, 47, 71, 73, 76

Ma, K.; Wang, H.; F. Blaabjerg. New approaches to reliability assessment: Using physics-of-failure for prediction and design in power electronics systems. *IEEE Power Electron. Mag.*, v. 3, n. 4, p. 28–41, Dec 2016. 39, 45

Madhusoodhanan, S.; Mainali, K.; Tripathi, A. K.; Kadavelugu, A.; Patel, D.; Bhattacharya, S. Power loss analysis of medium-voltage three-phase converters using 15-kv/40-a sic n-igbt. *IEEE Journal of Emerging and Selected Topics in Power Electronics*, v. 4, n. 3, p. 902–917, 2016. 77

Manoranjan, S.; Siva, K. Bidirectinal switched boost converter for ac-dc hybrid microgrid. In: *2014 IEEE Applied Power Electronics Conference and Exposition - APEC 2014*. [S.l.: s.n.], 2014. p. 2231–2236. 37, 40

Manz, D.; Piwko, R.; Miller, N. Look before you leap: The role of energy storage in the grid. *IEEE Power and Energy Magazine*, v. 10, n. 4, p. 75–84, 2012. 27

Molina, M. G. Energy storage and power electronics technologies: A strong combination to empower the transformation to the smart grid. *Proceedings of the IEEE*, v. 105, n. 11, p. 2191–2219, 2017. 34

Moseley, P.; Rand, D.; Peters, K. Enhancing the performance of leadacid batteries with carbon in pursuit of an understanding. *Journal of Power Sources*, v. 295, p. 268–274, 2015. 32, 33

MOURA. *7 Stationary leadacid batteries. General requirements and methods of test. Vented types*. [S.l.], 1987. 62

Nguyen, V. T.; Shim, J. W. Virtual capacity of hybrid energy storage systems using adaptive state of charge range control for smoothing renewable intermittency. *IEEE Access*, v. 8, p. 126951–126964, 2020. 24

Panday, A.; Bansal, H. Multi-objective optimization in battery selection for hybrid electric vehicle applications. *J. Electrical Systems*, v. 12, n. 2, p. 325 – 343, 2016. 29, 39

PereiraL, G.; Martínez, M. Comparison and influence of flywheels energy storage system control schemes in the frequency regulation of isolated power systems. *IEEE Access*, v. 10, p. 37892–37911, 2022. 25

Power Tech. *Power Tech - Advanced Energy Storage Systems*. [S.l.], 2021. Available in: <www.powertechsystems.eu/home/products/12v-lithium-battery-pack-powerbrick/>. 62

Reigosa, P. D.; Wang, H.; Y. Yang; F. Blaabjerg. Prediction of bond wire fatigue of igbts in a pv inverter under a long-term operation. *IEEE Trans. Power Electronics*, v. 31, n. 10, p. 7171–7182, Oct 2016. 45, 48, 77

Reigosa, P. D.; Wang, H.; Yang, Y.; Blaabjerg, F. Prediction of bond wire fatigue of igbts in a pv inverter under a long-term operation. *IEEE Transactions on Power Electronics*, v. 31, n. 10, p. 7171–7182, 2016. 50, 54

REN. *Renewables 2022: Global Status Report (GRS). 2022.* 2022. Available in: <http://www.ren22.net8/>. 24

Rodríguez, P.; Luna, A.; Candela, I.; Mujal, R.; Teodorescu, R.; Blaabjerg, F. Multiresonant frequency-locked loop for grid synchronization of power converters under distorted grid conditions. *IEEE Transactions on Industrial Electronics*, v. 58, n. 1, p. 127–138, 2011. 38

Rufer, A. *Energy storage: systems and components*. [S.l.]: CRC Press, 2017. 9, 25, 26

Sandelic , M.; Sangwongwanich, A.; Blaabjerg, F. Reliability evaluation of pv systems with integrated battery energy storage systems: Dc-coupled and ac-coupled configurations. *Electronics*, v. 8, n. 9, 2019. 29

Sandelic, M.; Sangwongwanich, A.; Blaabjerg, F. A systematic approach for lifetime evaluation of pv-battery systems. In: *IECON 2019 - 45th Annual Conference of the IEEE Industrial Electronics Society*. [S.l.: s.n.], 2019. v. 1, p. 2295–2300. 29

Sangwongwanich, A.; Angenendt, G.; Zurmühlen, S.; Yang, Y.; Sera, D.; Sauer, D. U.; Blaabjerg, F. Enhancing pv inverter reliability with battery system control strategy. *CPSS Transactions on Power Electronics and Applications*, v. 3, n. 2, p. 93–101, 2018. 29, 35

Sangwongwanich, A.; Yang, Y.; Sera, D.; Blaabjerg, F. Lifetime evaluation of grid-connected pv inverters considering panel degradation rates and installation sites. *IEEE Transactions on Power Electronics*, v. 33, n. 2, p. 1225–1236, 2018. 54

Scheuermann, U.; Schmidt, R.; Newman, P. Power cycling testing with different load pulse durations. In: *7th IET PEMD*. [S.l.: s.n.], 2014. p. 1–6. 48, 73

Schiffer, J.; Sauer, D.; Bindner, H.; Cronin, T.; Lundsager, P.; Kaiser, R. Model prediction for ranking lead-acid batteries according to expected lifetime in renewable energy systems and autonomous power-supply systems. *Journal of Power Sources*, v. 168, n. 1, p. 66–78, 2007. 9, 40, 41, 42, 43, 55

Sedo, J.; Kascák, S. Current harmonics compensation in single-phase grid-connected inverter. In: *2018 ELEKTRO*. [S.l.: s.n.], 2018. p. 1–6. 81

SEMIKRON. *Power Electronic System - SEMISTACK*. 2006. Available in: <http://www.semikron.com>. 11, 88

Shen, Y.; H.Wang; Yang, Y.; Reigosa, P. D.; Blaabjerg, F. Mission profile based sizing of igbt chip area for pv inverter applications. In: *IEEE 7th International Symposium on Power Electronics for Distributed Generation Systems*. [S.l.: s.n.], 2016. p. 1–8. 47

Stroe, D.; wierczyski, M.; Stan, A.; Teodorescu, R.; Andreasen, S. J. Accelerated lifetime testing methodology for lifetime estimation of lithium-ion batteries used in augmented wind power plants. *IEEE Transactions on Industry Applications*, v. 50, n. 6, p. 4006–4017, 2014. 39, 55

Stroel Ioan, D. *Lifetime Models for Lithium-ion Batteries used in Virtual Power Plant Applications*. Ph.D. Thesis (Doutorado), nov. 2014. 9, 43, 44, 55

Sundararajan, P.; Sathik, M. H. M.; Sasongko, F.; Tan, C. S.; Pou, J.; Blaabjerg, F.; Gupta, A. K. Condition monitoring of dc-link capacitors using goertzel algorithm for failure precursor parameter and temperature estimation. *IEEE Trans. Power Electron.*, v. 35, n. 6, p. 6386–6396, 2020. 49

Thakker, A.; Jarvis, J.; Buggy, M.; SahedFF, A. A novel approach to materials selection strategy case study: Wave energy extraction impulse turbine blade. *Materials and Design*, v. 29, n. 10, p. 1973–1980, 2008. 39

Vazquez, S.; Lukic, S. M.; Galvan, E.; Franquelo, L. G.; Carrasco, J. M. Energy storage systems for transport and grid applications. *IEEE Transactions on Industrial Electronics*, v. 57, n. 12, p. 3881–3895, 2010. 27

Vucijak, B.; Kupusovi, T.; Midi-Kurtagi, S.; eri, A. Applicability of multicriteria decision aid to sustainable hydropower. *Applied Energy*, v. 101, p. 261 – 267, 2013. Sustainable Development of Energy, Water and Environment Systems. 38

Wang, G.; Konstantinou, G.; Townsend, C. D.; Pou, J.; Vazquez, S.; Demetriades, G. D.; Agelidis, V. G. A review of power electronics for grid connection of utility-scale battery energy storage systems. *IEEE Transactions on Sustainable Energy*, v. 7, n. 4, p. 1778–1790, 2016. 27

Wang, H.; Blaabjerg, F. Reliability of capacitors for dc-link applications in power electronic convertersan overview. *IEEE Trans. Ind. Appl.*, v. 50, n. 5, p. 3569–3578, 2014. 49

Wang, J.; Hashemi, S.; You, S.; Trholt, C. Active and reactive power support of mv distribution systems using battery energy storage. In: *2017 IEEE International Conference on Industrial Technology (ICIT)*. [S.l.: s.n.], 2017. p. 382–387. 27

WEG. *ESSW - Sistema de Armazenamento de Energia em Baterias*. [S.l.], 2021. Available in: <www.weg.net>. 61

WeiQing, X.; Seamus, G. Dynamics of dissolution for underwater compressed air energy storage. In: *2019 Offshore Energy and Storage Summit (OSES)*. [S.l.: s.n.], 2019. p. 1–5. 25

Xavier, L. S.; Amorim, W. C. S.; Cupertino, A. F.; Pereira, H. A.; Seleme, S. I.; Teodorescu, R. Power converters for battery energy storage systems connected to medium voltage systems: a comprehensive review. *BMC Energy*, v. 1, n. 7, 2019. 27

Xu, L.; Miao, Z.; Fan, L.; Gurlaskie, G. Unbalance and harmonic mitigation using battery inverters. In: *2015 North American Power Symposium (NAPS)*. [S.l.: s.n.], 2015. p. 1–6. 27

Xu, X.; Bishop, M.; Oikarinen, D. G.; Hao, C. Application and modeling of battery energy storage in power systems. *CSEE Journal of Power and Energy Systems*, v. 2, n. 3, p. 82–90, 2016. 9, 24, 25, 27, 35

Yang, Y.; Sularea, V. S.; Ma, K.; Blaabjerg, F. Advanced design tools for the reliability of power electronics ; case studies on a photovoltaic (pv) system. In: *Conf. of the IEEE Industrial Electronics Society*. [S.l.: s.n.], 2015. p. 002828–002833. 47

Yang, Y.; Zhou, K.; Blaabjerg, F. Current harmonics from single-phase grid-connected invertersexamination and suppression. *IEEE Journal of Emerging and Selected Topics in Power Electronics*, v. 4, n. 1, p. 221–233, March 2016. 81

Yoon, K. System selection by multiple attribute decision making. *Ph.D thesis, Kansas State University*, 1980. 29

Zhang, Y.; Wang, H.; Wang, Z.; Yang, Y.; Blaabjerg, F. Simplified thermal modeling for igbt modules with periodic power loss profiles in modular multilevel converters. *IEEE Trans. on Industrial Electronics*, v. 66, n. 3, p. 2323–2332, 2019. 77

Zimann, F. J.; Batschauer, A. L.; Mezaroba, M.; Neves, F. A. Energy storage system control algorithm for voltage regulation with active and reactive power injection in low-voltage distribution network. *Electric Power Systems Research*, v. 174, p. 105825, 2019. 27